Simulation of relativistic jets in high-mass microquasars

Arthur Charlet

▶ **To cite this version:**

Arthur Charlet. Simulation of relativistic jets in high-mass microquasars. Solar and Stellar Astrophysics [astro-ph.SR]. Université Montpellier, 2021. English. NNT : 2021MONTS106 . tel-03619941

HAL Id: tel-03619941

https://theses.hal.science/tel-03619941v1

Submitted on 25 Mar 2022

HAL is a multi-disciplinary open access archive for the deposit and dissemination of scientific research documents, whether they are published or not. The documents may come from teaching and research institutions in France or abroad, or from public or private research centers.

L'archive ouverte pluridisciplinaire **HAL**, est destinée au dépôt et à la diffusion de documents scientifiques de niveau recherche, publiés ou non, émanant des établissements d'enseignement et de recherche français ou étrangers, des laboratoires publics ou privés.

THÈSE POUR OBTENIR LE GRADE DE DOCTEUR DE L'UNIVERSITÉ DE MONTPELLIER

En Astrophysique

École doctorale I2S

Unités de recherche LUPM, UMR 5299 ; CRAL, UMR 5574

Simulation de jets relativistes dans les microquasars à haute masse

Présentée par Arthur CHARLET
Le 10 décembre 2021

Sous la direction d'Alexandre MARCOWITH et Rolf WALDER

Devant le jury composé de

Yves GALLANT, Professeur des universités, Université de Montpellier	Président du jury
Julien MALZAC, Chargé de Recherche, Université de Toulouse III	Examinateur
Valenti BOSCH-RAMON, Associate Professor, Universitat de Barcelona	Rapporteur
Luca DEL ZANNA, Associate Professor, Universtià degli studi di Firenze	Rapporteur
Alexandre MARCOWITH, Directeur de recherche, Université de Montpellier	Directeur de thèse
Rolf WALDER, Professeur émérite, ENS de Lyon	Co-directeur de thèse
Zakaria MELIANI, Astronome Adjoint, Université de Paris	Invité
Doris FOLINI, Senior Scientist, ETH Zurich	Invitée

UNIVERSITÉ DE MONTPELLIER

Abstract

Microquasars, high-energy sources made of an accreting black hole and a stellar companion, are complex astrophysical objects where various physical phenomenon are at play. The name *microquasar* originates in the similarities found with *quasars*, an outdated term for a subcase of active galactic nuclei, especially the presence of a relativistic jet visible in radio. The energy loss related to these radiations, as well as other plasma processes, is not taken into account while simulating relativistic jets. Moreover, studies of microquasar jets are either performed with relativistic flow over small scales ($\sim$ one orbital separation) or Newtonian flow over large scales (tens of orbital separations), but not relativistic over large scales. This PhD thesis thus aim at filling the gap from both of these considerations.

Firstly, I developed analytical formulas for the cooling of an astrophysical plasma, as well as numerical tools aiming to precisely analyse and quantify simulated relativistic hydrodynamical jets. These tools were then used to study the impact of including the aforementioned cooling in state-of-the-art numerical simulations of hydrodynamical, relativistic jets over a large spatial and temporal scale. This study was performed with numerical setups based on the microquasars Cygnus X-1 and Cygnus X-3, which were (tentatively) reproduced for this PhD.

This PhD found that adding radiative losses induced a differential cooling between the jet beam and the surrounding cocoon. This differential cooling strengthens the overpressure of the latter over the former, which in turn modifies the jet internal structure, accelerating the growth of the Kelvin-Helmholtz instability, destabilising the jet and thus impacting its global structure and dynamics.

A parametric study around the chosen parameters for Cygnus X-1 and Cygnus X-3 was also performed. Results from previous studies such as jet bending and jet disruption by the stellar wind are confirmed, and the impact of the jet temperature on its stability and dynamics was investigated. A threshold effect is found: when the injected temperature is greater than the temperature to which the first recollimation shock would heat injected material of this density and velocity, the instability growth results in sensibly different dynamical properties of the jet.

Résumé

Les microquasars, sources de rayonnement à haute énergie composées d'un trou noir accrétant de la matière et d'une étoile compagnon, sont des objets astrophysiques complexes où divers phénomènes physiques sont en jeu. Le nom *microquasar* trouve son origine dans les similitudes trouvées entre ces objets et les *quasars*, terme désuet désignant un sous-ensemble de noyaux actifs de galaxie, en particulier par la présence dans les deux cas d'un jet relativiste visible en radio.

La perte d'énergie liée à ces radiations, ainsi que d'autres processus plasma, n'est pas prise en compte lors de la simulation des jets relativistes. De plus, les études des jets de microquasars sont réalisées soit avec un écoulement relativiste sur de petites échelles ($\sim$ une séparation orbitale), soit avec un écoulement newtonien sur de grandes échelles (dizaines de séparations orbitales), mais pas relativiste sur de grandes échelles. Cette thèse vise à comprendre l'impact de ces pertes sur les jets de microquasars, tout en proposant la première étude à la fois relativiste et à grande échelle de ces systèmes.

Notre étude se porte alors sur Cygnus X-1 et Cygnus X-3, deux microquasars à haute-masse (i.e. l'étoile compagnon est une étoile massive). Le premier est un des microquasars plus observés, découvert dès les années 60. Le deuxième est unique dans le fait que son étoile compagnon est une étoile de Wolf-Rayet, et est notable pour sa compacité et la très faible période orbitale du système binaire qui en découle : plusieurs heures contre plusieurs jours pour Cygnus X-1

Les jets relativistes hydrodynamiques

Les jets relativistes sont modélisés par les équations de l'hydrodynamique relativiste, dont la dérivation peut être trouvée dans les livres dédiés au sujet tels que Landau & Lifschitz (1959) ou Mihalas & Mihalas (1984). Les quantités thermodynamiques d'intérêt sont la densité dans le référentiel comobile ρ, la pression thermique p, l'enthalpie spécifique relativiste $h \equiv c^2+\epsilon+p/\rho$ (où ϵ est l'énergie interne spécifique) et la 4-vitesse $u^\alpha = (\gamma c, \gamma\vec{v})$, où $\gamma \equiv (1 - v^2/c^2)^{-1/2}$ est le facteur de Lorentz. Le système d'équations à résoudre est alors:

$$\partial_t(\gamma\rho) + \partial_i(\gamma\rho v^i) = 0, \tag{1}$$

$$\partial_t(\gamma^2\rho h v^j) + \partial_i(\gamma^2\rho h v^i v^j + pc^2\delta^{ij}) = 0, \tag{2}$$

$$\partial_t(\gamma^2\rho h - p) + \partial_i(\gamma^2\rho h v^i) = 0. \tag{3}$$

On introduit les densités relativistes conservatives de masse $D = \gamma\rho$, de quantité de mouvement $S^i = \gamma^2\rho h v^i$, et d'énergie $\tau = \gamma^2\rho h - p$. Ces variables sont aussi nommées *variables conservatives*, par comparaison avec les *variables primitives* que sont la densité, la vitesse et la température du fluide.

Le système d'équations est fermé avec l'équation d'état adiabatique d'index Γ :

$$\epsilon(\rho, p) = p/(\Gamma - 1)\rho. \tag{4}$$

On peut alors réécrire l'enthalpie spécifique $h = c^2 + \Gamma_1 p/\rho$, avec $\Gamma_1 \equiv \Gamma/(\Gamma - 1)$. Le système d'équations de la mécanique des fluides relativistes (SRHD) peut s'écrire sous une forme vectorielle :

$$\partial_t\mathcal{U} + \partial_i\mathcal{F}^i = 0, \tag{5}$$

où les variables conservatives ainsi que les flux correspondants dans la direction i sont donnés par :

$$\mathcal{U} = \begin{bmatrix} D \\ S^j \\ \tau \end{bmatrix}, \quad \mathcal{F}^i = \begin{bmatrix} Dv^i \\ S^j v^i + p\delta^{ij} \\ S^i \end{bmatrix}. \tag{6}$$

Les jets relativistes sont alors modélisés par un écoulement supersonique à haute vitesse lancé dans un environnement, dominé par les vents stellaire de l'étoile compagnon dans le cadre d'un microquasar. Leur étude se base sur celle de leurs équivalents à plus grande échelle, les jets relativistes des noyaux actifs de galaxie, dont je fais ici un résumé.

Une classification des jets relativistes est proposée par Martì et al. (1997), qui distingue 5 paramètres principaux pour décrire intégralement un jet : le ratio de la densité du jet avec celle du milieu ambiant $\eta \equiv \rho_j/\rho_w$, le ratio des pressions $K \equiv p_j/p_w$, la vitesse du jet à l'injection v_j (ou le facteur de Lorentz associé γ_j), le nombre de Mach du jet M_j, et l'indice adiabatique Γ. On ajoutera à cette liste la vitesse du vent stellaire v_w dans le cadre d'un jet de microquasar. La morphologie d'un jet et son évolution sont alors intégralement décrite par ce jeu de paramètres.

L'interaction entre le jet et son environnement génère une structure riche, dont il convient de donenr les éléments principaux, trois zones d'écoulement : 1) le faisceau central, cœur du jet, écoulement haute vitesse de matière du jet non perturbée ; 2) le cocon interne (parfois simplement « cocon »), entourant le faisceau, composé majoritaire de matière du jet choquée ; 3) le cocon externe (aussi appelé « cavité »), composé de matière du milieu ambiant choquée. Le faisceau est séparé du cocon interne par une combinaison de discontinuités, dont notamment un choc terminal. Il est marqué par une série régulière de chocs internes liés à l'équilibrage de la pression du faisceau avec celle du cocon qui l'entoure. La séparation entre les cocons interne et externe est marquée par une discontinuité de contact, et le cocon externe est séparé du milieu ambiant par un arc de choc.

Des instabilités hydrodynamiques peuvent croître durant la propagation du jet, agissant alors sur sa structure et sa propagation. L'instabilité dominante dans ces systèmes est l'instabilité de Kelvin-Helmholtz, dont l'étude dans le cadre d'un jet hydrodynamique commence dès le milieu des années 70. On peut tout de même citer d'autres instabilités à même de se développer lors de la propagation d'un jet : l'instabilité de Rayleigh-Taylor lorsqu'un fluide léger supporte un fluide plus lourd contre la gravité, ou de façon équivalente ici lorsqu'un fluide léger (le jet) accélère un fluide plus lourd (le milieu ambiant) par entraînement ; l'instabilité de Richtmyer-Meshkov qui se développe lorsqu'une onde de choc traverse une interface ondulée séparant deux fluides de propriétés thermodynamiques différentes ; et l'instabilité centrifuge induite par l'éventuelle rotation du jet sur lui-même.

Dans le cadre de cette thèse, je m'appuie sur les travaux d'Hanasz & Sol (1996) qui ont fait la dérivation complète de équation de dispersion de l'instabilité de Kelvin-Helmholtz dans la situation suivante : un écoulement plan formé d'un cœur relativiste, d'un cocon non-relativiste, et d'un milieu ambiant au repos. Les quantités du cœur relativiste sont indiquées par l'indice b, celles du cocon par l'indice c, et celles du milieu ambiant par l'indice w. Des perturbations à l'interface entre le cœur relativiste et le cocon provoquent la propagation d'ondes sonores dans le cocon, rebondissant entre les interfaces internes et externes du jet, amplifiant les perturbations à ces interfaces. Lorsque la distance effectuée par cette onde lors d'un aller-retour entre les deux interfaces coïncide avec un multiple

entier de sa longueur d'onde, la perturbation croit le plus vite. De cette condition de résonance, nous tirons une équation de dispersion simplifiée qui est alors résolue par la méthode de Newton-Raphson afin de trouver la valeur du nombre d'onde longitudinal k_x maximisant la la valeur de la pulsation ω, où les autres paramètres sont fixés par la situation choisie. Une estimation du temps de croissance *linéaire* de l'instabilité est alors obtenue par $t_{KHI} = \omega^{-1}$. il est à noter que ce temps linéaire ne correspond pas au temps réél de la croissance de ces instabilités, du fait de nombreux effets non-linéaires non considérés ici.

L'interaction entre un jet relativiste et un vent stellaire a été étudiée à petites échelles notamment par Perucho et al. (2010) et à grandes échelles parYoon & Heinz (2015). Le premier note notamment que des jets trop peu puissants peuvent être détruits par l'impact du vent et ne jamais propager au-delà de l'échelle du système binaire. Dans le cas contraire, un choc de recollimation se produit là où s'équilibrent la pression cinétique du vent et celle due à l'expansion latérale du jet. Lorsque le jet peut se propager au-delà de l'échelle du système binaire, l'impact du vent stellaire peut dévier la trajectoire du jet de façon significative.

Pertes radiatives dans les plasmas relativistes

On introduit les pertes d'énergie dans les plasmas par un terme source dans l'équation vectorielle de la SRHD:

$$\partial_t \mathcal{U} + \partial_i \mathcal{F}^i = \Psi. \tag{7}$$

Quatre phénomènes principaux sont à l'origine de ces pertes : le rayonnement continu de freinage (ou Bremsstrahlung) provoqué lors de la déviation d'un électron par le champ électromagnétique d'un proton ou ion, les émissions synchrotron dûs à l'interaction des électrons avec le champ magnétique local, la diffusion Compton inverse où des électrons énergétiques accélèrent des photons du rayonnement stellaire, et les pertes par recombinaison et lignes d'absorptions des électrons par les ions. De part l'isotropie des distributions de vitesses des électrons et ions dans le plasma, toutes ces pertes peuvent être considérées comme isotropes à leur tour, à l'exception de la diffusion Compton inverse. Cependant, dans un plasma ion - électrons, ce sont les premiers, bien plus massifs, qui portent la quasi-totalité de la quantité de mouvement, on considère alors que le ralentissement des électrons est négligeable sur le fluide. On modélise alors l'effets de ces radiations par un terme de perte d'énergie uniquement.

La dérivation de ces pertes, à l'exception des pertes par recombinaisons pour lesquelles nous avons utilisé la paramétrisation de Walder & Folini (1996), s'est faite en considérant la puissance rayonnée par un électron au cours de chaque processus puis en intégrant cette puissance sur la distribution de Maxwell-Jüttner décrivant une population d'électrons dans un plasma au repos:

$$n_e(\gamma) = \frac{n_e}{\Theta} \frac{\gamma_e(\gamma_e^2 - 1)^{1/2}}{K_2(\Theta^{-1})} \exp(-\gamma_e/\Theta), \tag{8}$$

où K_2 est la fonction de Bessel modifiée du second type d'ordre 2 et $\Theta = k_B T/m_e c^2$ la température normalisée. Cette formulation a été choisie car les températures atteintes dans les jets (plus de 10^{10} K) justifient un traitement relativiste des électrons. Les ions sont eux considérés comme non-relativistes à ces températures.

Ces pertes sont calculées dans l'approximation d'un plasma thermique et opticalement fin. Afin d'obtenir des spectres d'émission, les coefficients d'émissions associés à ces différents processus radiatifs ont également été dérivés.

Méthodes numériques

Les simulations réalisées pour cette thèse l'ont été avec le code A-MaZe, un code hydrodynamique sur grille eulérienne. L'intégration des équations de la SRHD se fait avec la méthode Runge-Kutta d'ordre 1 (ou méthode d'Euler), les flux étant évalués par un simple schéma central . Il est à noter que dans un schéma relativiste, l'évolution des variables conservatives nécessite la connaissance des variables primitives. Ces dernières sont obtenues à partir des premières en résolvant numériquement par la méthode de Brent une équation sur le facteur de Lorentz γ obtenue à partir des définitions des différentes variables et l'équation d'état. Les fonctions modifiées de Bessel du second ordre apparaissant dans les termes de pertes, une approximation numérique de ces fonctions a été implémentée dans A-MaZe.

Un code d'analyse a également été développé au cours de cette thèse afin de traduire les données de simulations, plusieurs To, en données scientifiques exploitables. Ce code utilise les définitions des différentes zones du jet afin de marquer les cellules de la grille de simulation selon leur appartenance à une de ces zones. Cela permet de procéder à des diagnostics plus précis, obtenir des valeurs moyennes plus représentatives, dériver le temps de croissance des instabilités, tracer des fonctions de densités de probabilités, etc. Je présente également une méthode afin d'obtenir un spectre d'émission depuis des données de simulations hydrodynamiques.

Résultats

Nous avons identifié trois phases dynamiques principales lors de l'évolution d'un jet : 1) une propagation initiale autosimilaire, en accord avec des considérations unidimensionnelles d'équilibre de quantité de mouvement, suivie par 2) une modification de la structure interne du jet et une phase de croissance de l'instabilité de Kelvin-Helmholtz, et enfin 3) un cocon turbulent et un faisceau déstabilisé.

Dans Cygnus X-3, où les pertes radiatives entrent en jeu aux échelles de temps couvertes par nos simulations, nous constatons que ces pertes affectent le rapport de volume entre le cocon extérieur et le cocon intérieur, ce qui met en garde contre un simple post-traitement des simulations ne tenant pas compte du refroidissement radiatif pour étudier les émissions des jets de microquasars. De même, on constate que le volume du faisceau obéit à une loi de puissance différente dans le temps selon que le refroidissement est actif ou non.

Du fait des caractéristiques différentes des zones du jet, le refroidissement n'est pas le même partout. En particulier, il est plus fort dans le faisceau que dans le cocon, ce qui contribue à augmenter le gradient de pression entre ces deux zones : la surpression du cocon par rapport au faisceau, responsable également de la collimation de ce dernier sur ces telles distances, est plus intense. Cela intensifie les chocs internes présents dans le faisceau. Or la croissance de l'instabilité de Kelvin-Helmholtz dépend de la structure de l'interface entre le faisceau et le cocon : plus les chocs sont resserrés, plus cette croissance

sera forte. Refroidir le jet le déstabilise.

Nous trouvons également que les sensibilités à la puissance du jet et aux paramètres du vent sont en accord avec la littérature. Nous complétons ce tableau en démontrant que l'augmentation de la température du faisceau entraîne une croissance plus rapide de l'instabilité et un ralentissement de la vitesse de la tête du jet. Compte tenu de la grande variété de microquasars à haute masse connus, mais aussi de la difficulté d'estimer les paramètres de leur système, des études de paramètres plus poussées et plus étendues sont clairement souhaitables à l'avenir. Sur la base des résultats présentés ici, nous préconisons que de telles études ne soient pas limitées aux simulations adiabatiques.

Contents

Introduction **1**
0.1 Quasars and microquasars . . . 1
0.1.1 Quasars . . . 1
0.1.2 Micro-quasars . . . 2
0.2 Two high-mass microquasars: Cygnus X-1 and Cygnus X-3 . . . 7
0.2.1 Cygnus X-1 . . . 7
0.2.2 Cygnus X-3 . . . 8
0.3 Physics of a microquasar . . . 10
0.3.1 Underlying mechanisms . . . 12
0.3.2 Non-thermal plasma processes in microquasars . . . 13
0.3.3 Understanding the jets . . . 16
Bibliography . . . 18

1 Relativistic hydrodynamical jets **27**
1.1 Special relativistics hydrodynamics . . . 27
1.1.1 Covariant hydrodynamics . . . 27
1.1.2 Model for jet propagation . . . 28
1.2 Instabilities in relativistic jets . . . 29
1.2.1 General picture . . . 29
1.2.2 Kelvin-Helmholtz instability . . . 30
1.2.3 Rayleigh-Taylor instability . . . 32
1.3 Description and classification of relativistic hydrodynamical jets . . . 33
1.3.1 Jet classification . . . 33
1.3.2 Jet propagation . . . 35
1.3.3 Steady state structure . . . 36
1.4 Effects of magnetic field on relativistic jets . . . 38
1.4.1 Effects on instabilities growth . . . 38
1.4.2 Effects on the steady-state structure . . . 39
1.5 Wind effects . . . 39
1.5.1 Jet bending . . . 40
1.5.2 Recollimation shock . . . 41
1.5.3 Wind clumpiness . . . 41
Bibliography . . . 41

2 Radiative processes in thermal, optically thin, relativistic plasmas **45**
2.1 Energy losses . . . 45
2.1.1 Free-free . . . 46

2.1.2 Synchrotron . . . 46
2.1.3 Inverse Compton scattering . . . 48
2.1.4 Line and recombination cooling . . . 49
2.1.5 Scalings and cooling time . . . 49
2.2 Volume emission . . . 50
2.2.1 Free-free . . . 51
2.2.2 Synchrotron . . . 52
2.2.3 Inverse Compton . . . 53
Bibliography . . . 54

3 Numerical methods and setups **57**
3.1 The A-MaZe Toolkit . . . 57
3.1.1 Integration scheme . . . 57
3.1.2 Inversion scheme . . . 58
3.1.3 Numerical approximation of Bessel K functions . . . 59
3.2 Benchmark for the scheme . . . 59
3.2.1 Basic tests of the adiabatic scheme . . . 60
3.2.2 Uncertainty for simulations of turbulent and cooling flows . . . 62
3.3 Numerical setups . . . 65
3.3.1 Physical parameters . . . 65
3.3.2 The need for a relativistic solver . . . 67
3.4 Post-processing methods . . . 67
3.4.1 Data tree . . . 68
3.4.2 Jet structure and cell identification . . . 69
3.4.3 Data extraction . . . 69
3.4.4 Data analysis . . . 69
3.4.5 Data access and visualisation . . . 70
3.5 Numerical calculation of the radiation emitted by a relativistic source . . . 70
Bibliography . . . 72

4 Structure and dynamics of cooled high-mass microquasar jets **75**
4.1 Cygnus X-1 and Cygnus X-3 fiducial cases . . . 75
4.2 Effects of losses on jet structure and dynamics . . . 81
4.2.1 Beam destabilising effect through cocoon pressure . . . 81
4.2.2 Effects on outer cocoon expansion . . . 82
4.3 Parameter sensitivities . . . 84
4.3.1 Effects of jet temperature on instabilities growth . . . 84
4.3.2 Effects of injected power . . . 86
4.3.3 Wind effects on jet propagation . . . 87
Bibliography . . . 87

5 Conclusion **95**
5.1 Summary . . . 95
5.2 Perspectives . . . 96
5.2.1 Jet zones diagnostics and equation of state . . . 96
5.2.2 Instabilities, shocks, and mesh resolution . . . 97
5.2.3 Jet bending and wind structure . . . 98

5.2.4 SED 99
5.2.5 Electron temperature and cooling 99
5.2.6 The hydrodynamical framework assumption 101
5.2.7 Wind driving and dynamics 102
Bibliography 103

Introduction

0.1 Quasars and microquasars

0.1.1 Quasars

The first observation of an active galactic nucleus (AGN) was produced by Fath (1909), but the presence of a gravitational well was not suggested until Seyfert (1943) from broad emission lines he linked to gas moving at high speed. After the beginning of radio astronomy in the 1930s (Jansky, 1933; Reber, 1940), a key discovery was the resolution of the bright radio source Cygnus A as two lobes (Jennison & Gupta, 1953) surrounding a galaxy. Shklovskii (1955) and Burbidge (1956) then identified synchrotron as the process responsible for the radio emission, and shown this emission to require very high energies.

1963 marked the discovery of 3C273, the first quasar (from "*quas*i-stell*ar*" object) (Hazard et al., 1963; Schmidt, 1963). This object is characterised by an even greater radio power than Cygnus A, a flat and compact radio spectrum, and a linear jet 20 arcsec long similar to M87. The spectrum from 3C273 differed from the one of Cygnus A by the presence of broad emission lines, which is a main difference between radio galaxies and quasars. Another distinguishing feature between those two objects is the size of the sources: the sources associated with radio loud quasars (RLQs) are compact, while they are extended in the case of radio galaxies. Optical surveys such as Sandage (1965) then found radio quiet quasars to be ten times more numerous than their radio-loud counterparts, but just as powerful in optical bands. It became clear that most galaxies have a nuclei that can be identified from spectral lines, stellar activity or non-thermal emission (Keel, 1983).

More surveys were then conducted throughout the electromagnetic spectrum. Smith & Hoffleit (1963); Dent (1965) found 3C273 to be highly variable in radio bands on timescale of days to years. Blazars, another high energy source, were found highly variable on timescales as short as minutes throughout the spectrum: in radio (Hughes, 1965), optical (Smith & Hoffleit, 1963), X-ray (Schreier et al., 1982) and γ-ray (Bignami et al., 1981; Punch et al., 1992) bands. At first mistakenly thought to be irregular stars in our galaxy, the similarities between the "variable star" BL Lacertae and the powerful radio source VRO 42.22.01 (Schmitt, 1968) have shown blazars to display many of quasar characteristics, and then identifying them as extragalactic objects (Oke & Gunn, 1974).

Early models of quasars suggested supermassive black holes (SMBHs) to explain the high radiative efficiency (Salpeter, 1964; Zel'dovich & Novikov, 1964). Accretion disks

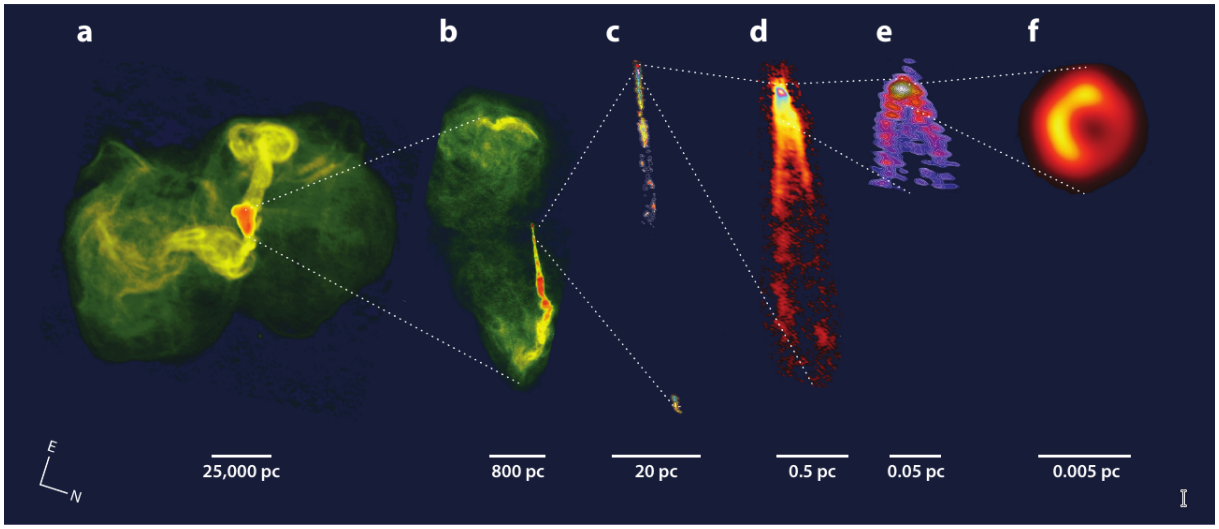

Figure 1: From Blandford et al. (2019). Montage of radio galaxy M87 from the outer lobes to the black hole vicinity. (*a*) Lobe jet and outer lobes. The present outburst and an older one almost perpendicular to the first can be seen; (*b*) galaxy jet and inner lobes; (*c*) full view of the BH jet; (*d*) innermost jet; (*e*) jet launching region near the SMBH; (*f*) inner accretion disc and black hole. Effects of relativistic beaming are visible in images *b*-*d*: even with the jet pointing with an angle $\sim 17°$ from our line of sight (Walker et al., 2018), the counter-jet is largely invisible. Images from: (*a*) NRAO, 90-cm VLA; (*b*) NRAO, 20-cm VLA; (*c*) NRAO, 20-cm VLBA (Cheung et al., 2007); (*d*) NRAO, 7-mm VLBA (Walker et al., 2018); (*e*) 3-mm global VLBI network (Kim et al., 2018); (*f*) 1.3-mm Event Horizon Telescope Safarzadeh et al. (2019) image of accretion disc and supermassive black hole. Abbreviations: VLA, Very Large Array; VLBA, Very Long Baseline Array; VLBI, very long baseline interferometry.

were investigated (Lynden-Bell, 1969; Bardeen, 1970), and jets from the galactic nuclei were identified as the mechanism behind double radio sources (Rees, 1971). Relativistic motion and its angular beaming effects (see figure 1) was suggested by Rees (1966) to explain the rapid radio variability of RLQs. This suggestion was the first step towards the unification of flat-spectrum radio quasars. Multiple generic models (fluid, particle and electromagnetic jets) were then explored to explain their origin, collimation, and emission (Blandford & Rees, 1974; Scheuer, 1974). Following this argument, blazars were also identified as an AGN where the relativistic jet is aligned close to our line of sight (Blandford & Rees, 1978; Ajello et al., 2013).

0.1.2 Micro-quasars

History

The first black hole binary (BHB) discovered was Cygnus X-1 in 1964 (Bowyer et al., 1965; Giacconi et al., 1967) in the beginning of X-ray astronomy. At this point, X-ray astronomy was done by sounding rockets boarded with X-ray sensitive instruments. Later optical observations revealed the binary nature of this source and allowed first estimations of the compact object mass to be done (Bolton, 1972; Webster & Murdin, 1972), making

Cygnus X-1 the first candidate for systems hosting a BH.

Relativistic jets were discovered in the 1990s from the BHBs GRS 1915+10 (Mirabel & Rodriguez, 1994) and 1E1740.7-2942 (Mirabel et al., 1992), to be followed by jets from both BHBs (e.g. Hannikainen et al., 2000, 2001; Corbel et al., 2005) and neutron star binaries (NSBs) (Fomalont et al., 2001; Migliari & Fender, 2006). In analogy to *quasars*, BHBs became to be known as *microquasars*. This increase in data allowed to study the connection between accretion and jet generation.

Contrary to Cygnus X-1 which is a *persistent* microquasar, most of them are *transients* and therefore only visible during *outbursts*. The first transient system classified as a BHB was A0620-00 (McClintock & Remillard, 1986), with a lower limit on the mass of the compact object at $3.2M_{\odot}$ (Elvis et al., 1975). Other notable transient microquasars include LMC X-1 and LMC X-3 in the Large Magellanic Cloud, and GX339-4 as one of the most extensively studied BHB (Markert et al., 1973).

The launch in 1987 of the Ginga satellite equipped with an all-sky monitor allowed for an increase in microquasars discoveries. Notable discoveries include: GS023+338 in 1989 (Makino, 1989), quickly linked with the optical source V404 Cygni as well as an optical transient observed more than 50 years earlier (Hurst, 1989). The first determination of the system mass function ($f(M) = 6.26 \pm 0.31M_{\odot}$) by Casares et al. (1992) dynamically confirmed this system as a BHB.

Studies in the hard X-ray/soft γ-ray bands were conducted in the 1980s by the *CGRO* and *Granat* observatories in a large energy domain range: from few keV to few MeV and even more for *CGRO*/EGRET. A big jump forward happened after the launch of the Rossi X-ray Timing Explorer (*RXTE*) satellite in 1995, carrying an All Sky Monitor which allowed the detection of a lot more outbursts and transients than before. The satellite was also equipped with two very flexible high time-resolutions instruments, allowing for high signal-to-noise data for timing and spectral studies in the 2-200 keV band. The INTErnational Gamma-ray Astrophysics Laboratory (*INTEGRAL*), another mission dedicated to high-energy emissions, was launched in 2002 just a few years after the *XMM-Newton* and Chandra X-ray satellites (both in 1999). *INTEGRAL*'s sensitive high-energy instruments contributed significantly to the research on microquasars. The cumulative contribution of these four observatories resulted in an explosion of information, leading to better data on the microquasars emission properties and a clearer understanding of the accretion process onto compact objects (Van Der Klis, 1996; Van der Klis, 1997; McClintock & Remillard, 2006; Done et al., 2007; Belloni & Motta, 2016).

Accretion states

The basic properties of microquasars were defined from the early era of observations: short timescale of variations and significant flux changes, leading to the definition of two accretion states (Tananbaum et al., 1972), historically called the *Hard Soft State (HSS)* and *Low Hard State (LHS)*. The "hard" or "soft" qualification is based on the cut-off frequency of the X-ray spectrum, a higher one meaning a "harder" spectral state. Those definitions were initially based on limited X-ray observations of Cygnus X-1 (which, as was understood later on, is an exception in the microquasar population from his persistent characteristics), but observations of other systems such as GX1124-683 (a.k.a. Nova Muscae 1991) or GX339-4 coupled to larger-band observations of Cygnus X-1 precised the picture of microquasar spectral states, defining additional states depending on their

complex spectral and timing properties (e.g. Miyamoto et al., 1993; Homan et al., 2006; Done et al., 2007; McClintock et al., 2009). Restricting ourselves to the original two accretion states from Tananbaum et al. (1972) still leads to a number of state classifications (Zdziarski & Gierliński, 2004; Homan et al., 2005; McClintock & Remillard, 2006) due to the complex details of the emission (e.g. Gilfanov, 2010). Following Motta et al. (2021), we will describe the classification originally suggested by Homan et al. (2005) (see also Belloni et al., 2011; Belloni & Motta, 2016).

The interactions between the different components of a BHB system and their spectral and time-variability properties may change over a small timescale of $\sim$ hours or even faster, in ways that may depend on the current state and/or state transitions of the microquasar. Drawing the X-ray intensity (in units of instrumental count rate, luminosity or flux) as a function of a hardness ratio (calculated as a ratio of count rates/luminosity/fluxes in two energy bands, typically hard over soft) gives the so-called X-ray *hardness intensity diagram (HID)* which highlights the cyclical aspect of those variations (see figure 2 for a sketch of a typical HID). A HID can be seen as the X-ray equivalent of the stellar Hertzsprung-Russel diagrams, but drawn for a single source over its observed evolution instead of being populated by several sources at different evolutionary phases.

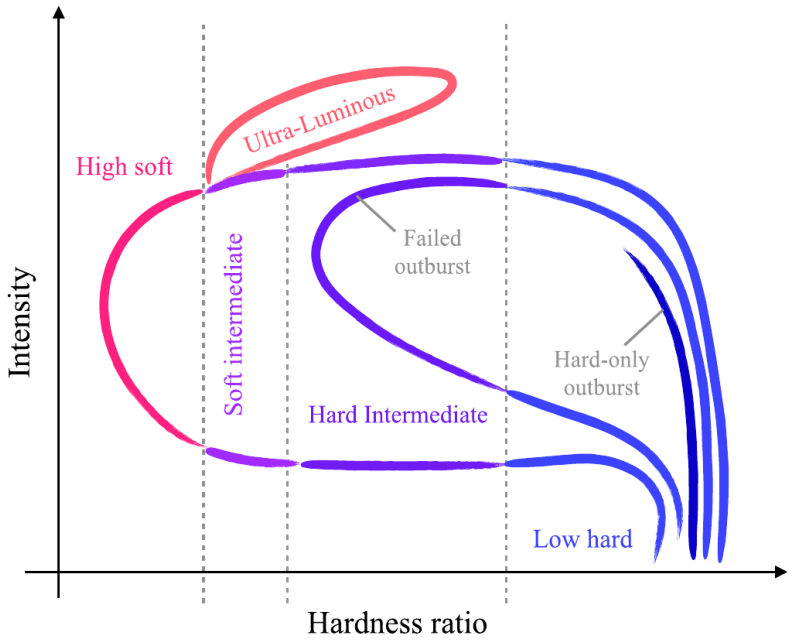

Figure 2: From Motta et al. (2021). Sketch of a typical Hardness Intensity Diagram (HID). The accretion states sampled during an outburst (except the ultra-luminous state) each occupy a vertical band in the HID, with their name displayed. A BHB will travel counter-clockwise during an outburst.

HID are commonly used to describe the evolution of accreting stellar mass BH (Belloni & Motta, 2016), but have also been used for NS binaries (Muñoz-Darias et al., 2014) and AGN (Körding et al., 2006; Svoboda et al., 2017). In most cases, a microquasar will follow the same evolution in the HID during an outburst, visualized by the "q-shaped" curve traversing all the states: in the beginning the system will be in the LHS at the bottom right of the HID, with the intensity increasing. Then, the hardness ratio will start to diminish at constant intensity, traversing the *Intermediate State* to the HSS which generally includes

or follows closely the peak of the outburst. Then, after a decrease in intensity, the hardness ratio will rise again, traversing the intermediate state again and ending up back in the LHS. This hysteresis circle (Miyamoto et al., 1995) can be seen as going through the q-shaped curve in figure 2 counter-clockwise. Belloni & Motta (2016) split the Intermediate State in the *Hard Intermediate State (HIMS)* and *Soft Intermediate State (SIMS)*, which can be distinguished by their different timing properties. A fifth *Ultra-Luminous State (ULS)*, or anomalous state (Motta et al., 2021), has been observed in a few sources, sharing some properties with the two intermediate states and characterised by a high luminosity reaching or even exceeding the Eddington limit (Uttley & Klein-Wolt, 2015).

This canonical pattern is followed by many transients microquasars during their outburst, with some outbursts showing occasional back-and-forth between the two intermediary states or even all the way back to a main accretion state in rare cases (see e.g. Fender et al., 2004; Motta et al., 2009, 2012; Brocksopp et al., 2002, for examples such as GX 339-4, GRS 1655-40 or XTE J1859+226). Other types of outbursts which do not show all the main accretion states, also drawn figure 2, have also been observed in a relatively small number over the past decades: some show hard-only outbursts, never leaving the LHS (Brocksopp et al., 2002), while others only managed to attain HIMS before returning to LHS and quiescence (Capitanio et al., 2009; Ferrigno et al., 2012; Soleri et al., 2013) and are usually called *failed* outbursts, even though some literature use this term to describe hard-only outbursts. Some sources have been observed undergoing both canonical and failed outbursts (Sturner & Shrader, 2005). Capitanio et al. (2008) argued that the lack of a transition to the HSS could be explained by a premature decrease of the accretion rate.

A weaker outburst called re-flares or re-brightening (e.g. Kajava et al., 2019) may follow the initial outburst by a few weeks to a few months, during which the source luminosity rises out of quiescence with no transition to a softer state. This is so similar to hard-only outbursts that it is unclear whether these events are physically different. Similar secondary outbursts were also observed in white dwarf binaries (see e.g. Kuulkers et al., 1996) or NSBs (e.g. Lewis et al., 2010; Patruno et al., 2016). This suggests these outbursts could take origin in a disc instability or an increase in the companion mass-shedding, the latter of which possibly caused by X-ray heating of the star outer layers during the primary outburst (Tanaka, 1995; Lasota, 2001).

Spectral properties

Unlike the complex spectra of accreting NSs, the typical X-ray spectrum of a microquasar presents two main components. Firstly, a multi-colour disc black-body (Shakura & Sunyaev, 1973) contributes to the spectrum below $\sim$ 6 keV, peaking at a few keV. This component have long variation timescales and does not contribute significantly to the spectrum variability on outbursts timescales; it is explained by a geometrically thin, optically thick, inner disc truncated at a radius usually larger than the innermost stable circular orbit (ISCO, Bardeen et al., 1972).

The second main contribution to the spectrum was identified as non-thermal emission from Comptonisation of disc photons, typically appearing over 5-10 keV (Sunyaev & Titarchuk, 1980; Haardt et al., 1994), characterised by a power law with an high-energy cut-off linked to the temperature of the Comptonising electrons (Eardley et al., 1975; Sunyaev & Titarchuk, 1980; Zdziarski et al., 2004; Joinet et al., 2005; Done et al., 2007).

This component is believed to primarily originate from a cloud of electrons located close to the BH, historically refered as the *corona* by analogy with stellar coronæ, and is most likely a part of the accretion flow onto the BH, coinciding at least partly with its central part called the *hot flow*. This hot flow is believed to replace or surround a razor-thin Shakura-Sunyaev existing outside of the aforementioned disc (Shapiro et al., 1989; Narayan & Yi, 1994; Esin et al., 1997; Done et al., 2007; Marcel et al., 2018a,b, 2019). The accretion flow inwards of the inner disc truncation radius is then best described by a geometrically thick disc. The high variability of this non-thermal component is responsible for the high variability in microquasar spectra.

This hard X-ray component does not show any cut-off under MeV energies in the soft state where the corona electrons have been cooled down by the photons' upscattering, leading studies to suggest the existence of a small electron population with a non-thermal/power-law distribution responsible for this emission through inverse Compton scattering (Coppi, 1999; Poutanen & Svensson, 1996; Gierliński et al., 1999; McConnell et al., 2002; Zdziarski et al., 2002). In the hard state, this component comprises emission from thermal electrons in a hot plasma cloud and its variability is driven by the variations in seed photon flux. An additional high-energy, power-law tail extending in the MeV may also be present, showing no cut-off (Bouchet et al., 2003). Tentative explanations of this high-energy tail involve the contribution of jets, or Comptonisation of seed photons by nonthermal electrons (see e.g. Zdziarski et al., 2012).

A third component may appear in the spectra and is believed to be reflection of the hot flow emission off the geometrically thin disc, taking the form of several lines around 6.4 keV attributed to the Fe Hα line as well as several Fe ionisation states and a high-energy bump around 30 keV (Garcia et al., 2013). The presence of a local absorber in some sources such as V404 Cyg (see e.g. Motta et al., 2017) significantly affects the emission. In those cases, the so-called *reflection* also includes the radiation reprocessed in this local absorber by up- and down-scattering in a cool and possibly inhomogeneous, nearly optically thick medium.

The contributions of these different spectral components vary with the accretion states, determining the spectrum in the X-ray band as well as the fast time-variability properties during outburst. Non-thermal emission from the hot flow dominates in the LHS with little to no contribution of the disc black-body component, showing hard spectra extending sometimes up to hundreds of keV and up to 30% fast time-variability. In the HSS, the X-ray emission is dominated by the accretion disc, presenting a soft X-ray spectrum, very little to no thermal component and less than 5% fast-time variability. In this state, the radio(-millimetre) spectra is flat or even inverted (Fender, 2001).

Both thermal and non-thermal components are present in the other states, with relative contributions depending on the outburst phase. The evolution of the source from the LHS to the HSS is linked to a decrease in the inner disc truncation radius, causing a decrease in hot flow emission and a rise in thermal emission. The opposite trend is observed when the source moves from HSS to LHS (Done et al., 2007). The fast time-variability is driven by with those trends, decreasing along the LHS to HSS transition due to the decrease in non-thermal, variable seed photons which become diluted in the thermal photons, and the other way round for the HSS to LHS transition.

A word on neutron stars binaries

Some effects specific to neutron stars permits to discriminate between NS and BH binaries. Firstly, a BH has no material surface, and therefore cannot present some effects such as type I bursts. Those events, similar to recurrent novæ with a NS as the accretor instead of a white dwarf, result from the nuclear burning of accreted material on the NS surface at a timescale ranging from a few seconds to a few minutes (see e.g. Schatz & Rehm, 2006, for more details on X-ray bursts and the underlying nuclear physics). Another distinguishing feature stems from the fact that a BH cannot sustain a magnetic field anchored within it, and thus cannot give birth to the periodic X-ray pulsations observed for many NSs. These effects are considered as firm signatures of a NS (Tanaka, 1995) and allow to distinguish between NS and BH binary in cases where the mass measurements cannot permit to determine the nature of the compact object (e.g. Zdziarski et al., 2013, for Cygnus X-3 case).

0.2 Two high-mass microquasars: Cygnus X-1 and Cygnus X-3

0.2.1 Cygnus X-1

As explained section 0.1.2, Cygnus X-1 was discovered during the flight of a sounding rocket in 1964 (Bowyer et al., 1965) and was later identified as a massive source in orbit with O-type star HDE226868 (Bolton, 1972; Webster & Murdin, 1972), becoming the first BH candidate. The latest VLBI parallax measurement by Miller-Jones et al. (2021) find the source at a distance $2.22^{+0.18}_{-0.17}$ kpc, almost 20% greater than the previous estimate from Reid et al. (2011) obtained by measuring Cygnus X-1 trigonometric parallax.

With a circular orbit 40 $R_\odot$ wide travelled in a 5.6 d period by the binary components (Brocksopp, 1998), the distance is small enough for the stellar wind to be gravitationally focused towards the BH (Gies & Bolton, 1986) of mass 21 $M_\odot$ (Miller-Jones et al., 2021). A schematic diagram of the binary system is given figure 3, taken from Orosz et al. (2011). The presence of a small accretion disc dampens the typical short-term fluctuations of pure wind accretors, which results in Cygnus X-1 staying in the LHS 73% of the time (Orosz et al., 2011, based on hardness count). Cygnus X-1 has thus been considered as the prototype of microquasars in the LHS for a long time, although excursions into the HSS have been observed, especially in the last decade (Grinberg et al., 2013; Cangemi et al., 2021b). This timely evolution of Cygnus X-1 spectral state is shown figure 4, taken from Cangemi et al. (2018), presenting the *INTEGRAL/IBIS* lightcurve of Cygnus X-1 from years 2004 to 2018.

In its (low) hard state, the X-ray spectrum of Cygnus X-1 is represented by a power-law continuum with an exponential cut-off above a few hundreds keV. This may be well described by the sum of a Comptonisation continuum (Pottschmidt et al., 2003; Del Santo et al., 2013) and a Compton reflection hump (Duro et al., 2016) with seed photons from a blackbody disc peaking at a fraction of keV (Ebisawa et al., 1996; Salvo et al., 2001), while the deviations from this continuum indicate a soft γ-ray tail whose origin is still unclear. The two main investigated origins are a non-thermal particle population in the accretion flow (Romero et al., 2014; Chauvin et al., 2018), or synchrotron emission from

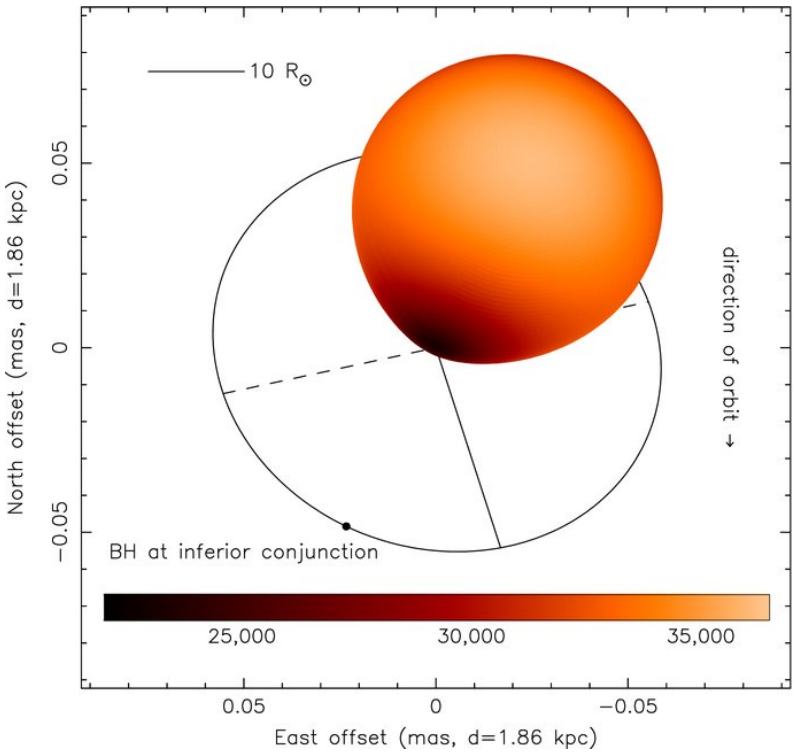

Figure 3: From Orosz et al. (2011). Schematic diagram of Cygnus X-1 as it would appear on the sky plane. The ellipse indicates BH orbit, with major ax in solid line and minor ax in dashed line. The orbital motion goes in the clockwise direction (Reid et al., 2011), the colormap shows the local effective temperature. The star is cooler near the inner Lagrangian point due to gravity darkening (Orosz & Hauschildt, 2000).

the jet (Malzac et al., 2006; Zdziarski et al., 2012; Del Santo et al., 2013; Pepe et al., 2015; Kantzas et al., 2021) .

The broadband spectrum from Cygnus X-1 in the HSS is well modelled by the summed contributions of a blackbody disc, Compton scattering by thermal and non-thermal electron components, and Compton reflection with the accompanying Fe Kα fluorescence line (Gierliński et al., 1999; Frontera et al., 2001; McConnell et al., 2002) as in the LHS. A comparison of the spectrum in the LHS and HSS is shown figure 5.

0.2.2 Cygnus X-3

Cygnus X-3 was discovered not long after Cygnus X-1 (Giacconi et al., 1967). The peculiarity of this system lies in the nature of the companion star as it is the only known X-ray binary including a Wolf-Rayet (WR) star (Van Kerkwijk et al., 1992; Van Kerkwijk, 1993; Van Kerkwijk et al., 1996; Fender et al., 1999; Koljonen & Maccarone, 2017), as well as in the very small orbital separation between the compact object with an orbital period of 4.8 h (Parsignault et al., 1972; Singh et al., 2002) that could indicate a past spiral-in episode during common-envelope evolutionary stage. Given the estimates of the binary masses and stellar mass loss rate, the compact object is thought to orbit in the WR star photosphere.

The nature of the accretor is still a mystery and could be a NS or a BH as the system

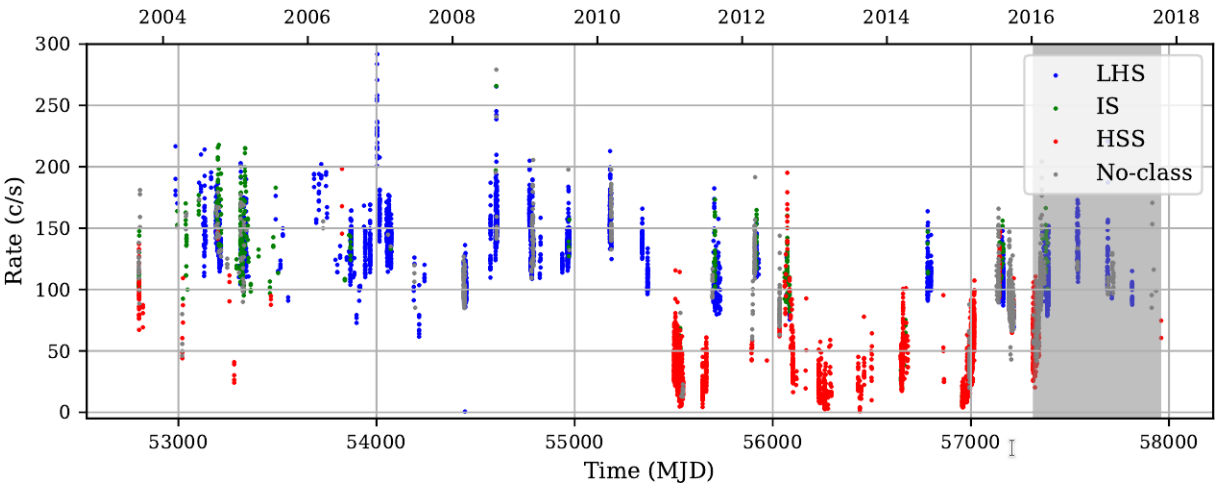

Figure 4: From Cangemi et al. (2018). Cygnus X-1 20-40 keV *INTEGRAL/IBIS* lightcurve extracted on a Scientific Window (ScWs, individual uninterrupted *INTEGRAL* pointing). Each point was classified as LHS (blue), IS (green) or HSS (red) according to Grinberg et al. (2013). ScWs that couldn't be classified are in grey. The grey area correspond to the period after 2016, which described as with dubious calibration.

mass function could not be estimated yet (e.g. Hanson et al., 2000; Vilhu et al., 2009), but the spectral properties of the source seem to point towards a BH (Szostek & Zdziarski, 2008; Hjalmarsdotter et al., 2008; Zdziarski et al., 2013; Cangemi et al., 2021a), notably a radio flux in the HSS that is strongly correlated to soft X-ray flux with a very similar correlation to what is observed in BHBs. Cygnus X-3 is also one of the brightest X-ray binary in radio (McCollough et al., 1999), presenting very strong radio outbursts and resolved jets (Martí et al., 2000; Mioduszewski et al., 2001). High-energy γ emission has also been unambiguously confirmed for this accretion-powered microquasar (Fermi LAT Collaboration, 2009; Tavani et al., 2009).

The global shape of Cygnus X-3 spectrum is similar to other microquasars, but the value of the spectral parameters can be significantly different: the exponential cut-off in the hardest states is at a lower energy of $\sim$ 20 keV and the disc is very strong in the softest states (Szostek & Zdziarski, 2008; Hjalmarsdotter et al., 2008; Cangemi et al., 2021a). This specifities in the spectrum, which Zdziarski et al. (2010) explains by a scattering of the emission in the strong stellar wind, and their correlation with the radio emission led Szostek & Zdziarski (2008) to separate Cygnus X-3 spectral behaviour into six spectral states. Five of them are defined according to both X-ray spectral shape and radio flux, while the last one, deemed as "hypersoft", is based on the source's HID (Koljonen et al., 2010).

This hypersoft state precedes the emission of powerful radio ejections (Beckmann et al., 2007; Koljonen et al., 2010) and is defined by three main characteristics: the absence of iron lines (which was shown by Koljonen et al. 2018 to be an orbital effect); either a pure blackbody emission or an accretion disc spectrum Comptonised by electrons of the same temperature as the disk; and a faint power-law tail over 20 keV with spectral index $\sim$ 2. Koljonen et al. (2018) explain these properties by a turned-off (or highly diminished) jet production, the low pressure allowing the wind to refill the region close to the black hole. γ-ray emission from Cygnus X-3 is most often detected when the source transits to/from

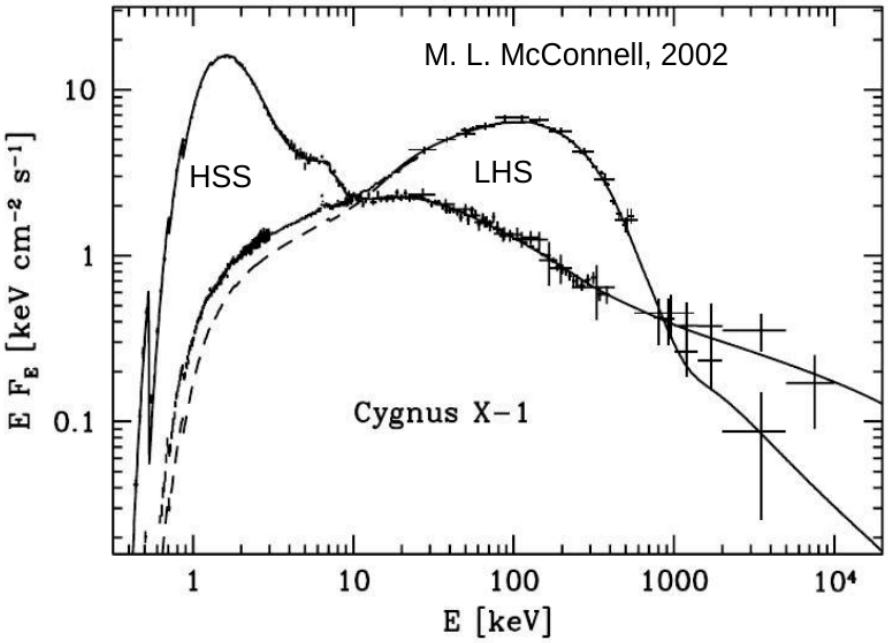

Figure 5: From McConnell et al. (2002). Comparison of Cygnus X-1 spectrum in the HSS and LHS, fitted with EQPAIR model in solid lines (Gierliński et al., 1999). Dashed curve shows the model fitting the *CGRO* data only.

the hypersoft state, and occasionally during this state when connected to radio flares (Tavani et al., 2009; Fermi LAT Collaboration, 2009; Corbel et al., 2012; Bulgarelli et al., 2012).

The presence of a Thomson-thick, low-temperature, plasma cloud surrounding Cygnus X-3 has been postulated by e.g. Davidsen & Ostriker (1974) and Hertz et al. (1978) from the energy-independant orbital modulations of the X-ray flux, and by Berger & van der Klis (1994) from the lack of high frequencies in the power spectra. The presence of such an absorber is indicated by a deep ~ 9 keV Fe K edge in the X-ray spectra (see e.g. Szostek & Zdziarski, 2008). The effects of its possible presence have been studied by Zdziarski et al. (2010), who reproduced both the X-ray spectrum and power spectrum of Cygnus X-3 in the hard state with their model.

0.3 Physics of a microquasar

Accretion-ejection connection

A general picture for accretion-ejection connection was suggested by Fender et al. (2004), with equivalent conclusions drawn by Corbel et al. (2004) and approaching the scenarios described by Meier (1999, 2001, 2003) from a more theoretical approach. This simplified model is displayed figure 6 and links the presence of a jet with disc inner radius. The four sketches indicates the state of the source in the phases of the microquasar cycle: in a first phase (i), the source is in the LHS with low X-ray luminosity and a jet whose power correlates to the X-ray luminosity as $L_j \propto L_X^{0.5}$, the emission is dominated by the

corona in X-ray while the radio emission is dominated by the steady, compact (meaning not resolved in high-resolution radio images) jet. The luminosity then rises to a peak (state (ii)) before the spectrum starts softening and the source moves horizontally to the left of the HID, crossing the HIMS. The accretion disc inner radius diminishes during this evolution, as the higher densities in the disc allows it to cool effectively, thus becoming thin even in its innermost region. This causes the jet velocity to rise subsequently after a delay. This rise becomes sharp as the disc inner radius approaches a few ISCO radii in state (iii), launching a final powerful jet that catches up to the slower-moving steady jet, provoking an strong, optically thin internal shock which can produce some microquasar spectral properties such as the flat SED as suggested by Malzac (2013, 2014). The jet is then suppressed as the inner disc radius attains the ISCO and the source enter the disc-dominated HSS, the stage (iv). The disc radius then recedes from reheating following the reverse process from phase (ii), probably coupled to highly ionized disc winds flowing in an almost equatorial direction. These winds transport the excess energy that is not radiated away, and are thought to emit a great amount of matter possibly comparable to the accreting matter flow. Muñoz-Darias et al. (2016) suggest this mechanism could trigger a return to the LHS. This simplified scenario fits nicely the pattern described section 0.1.2 and remain overall true to explain the various microquasar spectral properties.

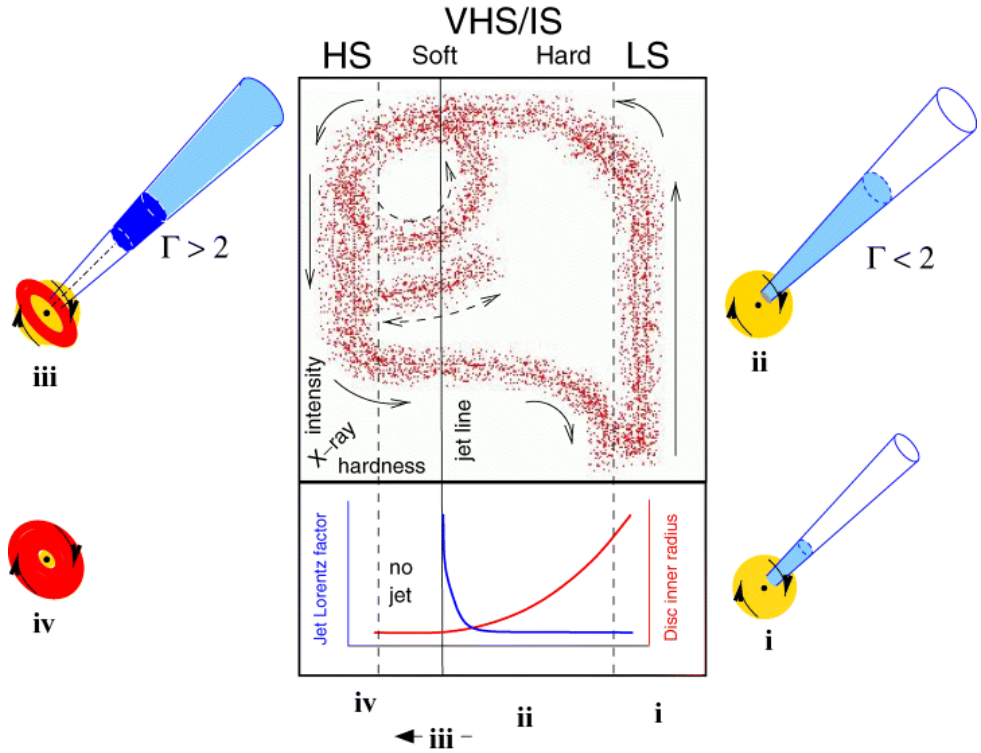

Figure 6: From Fender et al. (2004). The upper central panel represents an HID comparable to Fig. 2, in our terminology introduced section 0.1.2, 'HS' corresponds to HSS, 'LS' to LHS and VHS/IS to the intermediary states HIMS and SIMS. Lower panel displays jet bulk Lorentz factor and inner disc truncation radius versus X-ray hardness. Schematics of the system are given around those central panels, with the jet represented in blue, corona in yellow and accretion disc in red. The dashed loop and dotted track indicate the path taken by some sources producing several radio outbursts such as GRS 1915+105.

0.3.1 Underlying mechanisms

Accretion

The matter inflow in microquasars comes either from Roche lobe overflow (RLOF), capturing part of the stellar wind, or a combination of both. The Roche lobe is defined as the region around a star in a binary system within which matter is gravitationnaly bound to that star. In the case where the star radius is greater than this region, stellar matter flows through the Lagrangian point L1 unto the accretion disc. This may happen in the case where the star evolves and its radius grows past its Roche lobe, or as the orbital separation decreases. This may happen from the wind escaping the system, carrying away part of its angular momentum, slowing the binary rotation down and thus the orbital separation diminishes (see e.g. Davidsen & Ostriker, 1974).

Main sequence low mass companion present very weak winds which cannot contribute to the BH accretion and are therefore pure RLOF systems, while evolved low-mass or high-mass companions present stellar winds strong enough to be a significant matter source for the BH accretion disc. RLOF and wind accreting both operate in low-mass BHB GRS 1915+105 hosting a red giant companion, while the stellar companion in high-mass systems often does not fill the entirety of their Roche lobe, and the accretion disc is then fed through wind only (see e.g. Walder et al., 2014, for numerical study of this latter situation).

Disc structure and jet launching

The same basic ingredients seems to be the recipe for the production of an astrophysical jet: a gravitational potential well, matter accretion, angular momentum and magnetic fields. The potential well is a supermassive black hole in case of jets from AGN, and stellar mass BH or NS for microquasars. The accreted matter comes from the central region of a galaxy for AGN jets and from the wind of a stellar companion for microquasars, and form an accretion disc as it falls onto the compact object.

The structure of an accretion disc depends on the accretion rate $\dot{M}$, with three main regimes which can be identified by the relation of the accretion rate to a critical rate defined as:

$$\dot{M}_{crit} = \frac{L_{Edd}}{c^2}, \tag{9}$$

where $L_{Edd} \equiv 4\pi G M m_p c/\sigma_T$ is the Eddington luminosity, defined as the luminosity of accreting gas necessary to stop spherical accretion by radiation pressure.

At subcritical rates $\dot{M} < \dot{M}_{crit}$, the disc can be described by the standard model from Shakura & Sunyaev (1973) as geometrically thin and optically thick. At very low accretion rates $\dot{M} \ll \dot{M}_{crit}$, hot and optically-thin advection-dominated accretion flow are possible according to e.g. Narayan & Yi (1994); Yuan & Narayan (2014). In the last, super-critical case $\dot{M} \gg \dot{M}_{crit}$, the disc is optically thick, advection dominated, and may be geometrically slim or thick (Abramowicz et al., 1989; Begelman & Meier, 1982; Wiita, 1982). The magnetic field generated in the disc is expected to be intially only toroidal, then a poloidal magnetic flux can be generated *in situ* through turbulent dynamo induced by magnetorotational instabilities (Tout & Pringle, 1996; Liska et al., 2020).

Wald (1974) showed that a spinning (Kerr) black hole with zero net electric charge and its spin aligned with an external uniform magnetic field will induce an electric field

with $\vec{E} \cdot \vec{B} \neq 0$. An uniform field at infinity was assumed, but King et al. (1975) extended this result to any realistic aligned field as they essentially all have the same structure around the black hole. They also showed that the induced electric structure is such that $\vec{E} \cdot \vec{B}$ has opposite signs near the poles and near the equator of the spinning black hole.

This led Blandford & Znajek (1977) (BZ77) to consider the case of a Kerr BH at the center of an accretion disc which creates an aligned magnetic field. The central disc and the black hole spin are usually aligned by the Bardeen-Petterson effect (Bardeen & Petterson, 1975), therefore this magnetic field should also be aligned with the spin of the black hole. BZ77 noted that in the case where a conducting medium surrounds the black hole, the electric field structure discussed earlier must produce an effective current through the black hole and returning through the conducting medium. Any dissipation of this current's energy in the surrounding material taps into the spin energy of the black hole. This is the Blandford-Znajek mechanism, which is believed to be the main process responsible for jet launching.

This process was investigated in BZ77 using the force-free approximation in a charge-separated collisionless plasma (see also Komissarov, 2004). A number of authors studied this mechanism in the case of the ideal MHD approximation for the surrounding medium often through numerical approaches (see Davis & Tchekhovskoy, 2020; Komissarov & Porth, 2021, for review), as well as Particle-In-Cell (PIC) methods more recently (e.g. Parfrey et al., 2019; Crinquand et al., 2019).

The launching of jets in other systems with no black hole (such as neutron star X-ray binaries or young stellar objects) suggests that the BZ mechanism is not always required for jet launching. Furthermore, the jet production mechanism in X-ray binaries is not consistent with the prediction done with the BZ mechanism, as shown by Russell et al. (2013). Thus, the most likely mechanism according to King & Pringle (2021) would be some form of MHD process resulting from poloidal magnetic field threading the accretion disc (Livio et al., 1999), or a mix of both as Komissarov (2021) concluded the BZ mechanism could not be invalidated by the arguments presented in King & Pringle (2021). Such a disc-based mechanism was already discussed in BZ77 and a more in-depth study was conducted in Blandford & Payne (1982).

This Blandford-Payne (BP) mechanism can be described as follows: an outflow is driven out of the disc and reaches the poloidal component of the magnetic field due to the gas pressure in the corona. Then, this flow is driven centrifugally along the poloidal field lines inclined by an angle $\leq 60°$ with respect to the disc surface. Far away from the disc, the toroidal component collimates and accelerates the outflow into a pair of anti-parallel jets perpendicular to the disc, extracting energy and angular momentum from the disc through magnetic stress.

0.3.2 Non-thermal plasma processes in microquasars

Relativistic plasmas found in microquasar systems are the source of high-energy emissions, as presented in section 0.1.2. These emissions are typically produced when accelerated particles interact with a target, be it a magnetic, photon, or matter field. To paint a more complete picture of the physics of our studied systems, following Bosch-Ramon (2008) we present here the basics of the underlying particle acceleration mechanisms and subsequent emission processes involved in a microquasar.

Particle acceleration mechanisms in microquasar jets

To produce high-energy emissions, an emitting population of particles need to be accelerated. Various acceleration processes may occur in a microquasar jet, depending on the physical parameters where the particles are accelerated, which themselves depend on the considered part of the jet.

At the base where the jet could be magnetically dominated, MHD instabilities may accelerate particles through magnetic energy dissipation (Zenitani & Hoshino, 2001). Another way would be converter mechanisms (Derishev et al., 2003; Stern & Poutanen, 2008) to take place if the jet velocity is high enough, as the photon and matter fields are high at jet base due the proximity to the accretion disc. A non-thermal population of particles may also be directly injected into the jet, produced by either magnetic reconnection in the surrounding corona (see e.g. Gierliński & Done 2003 and references therein) or by magnetocentrifugal mechanism close a rotating black hole (Neronov & Aharonian, 2007; Rieger & Aharonian, 2008).

At the binary system scales, it is the different versions of the Fermi acceleration which are the more plausible: diffusive shock acceleration (first-order Fermi process, see Drury, 1983) at the internal shocks in the jet (some of which originating in the jet-wind interaction), random scattering acceleration (second-order Fermi process, Fermi, 1949) if magnetic turbulence is strong enough (with high Alfven velocities), and gradual shear acceleration in the shear layer surrounding the jet (Rieger & Duffy, 2004). See also Rieger et al. (2007) for a more in-depth discussion of those processes in the context of astrophysical jets.

Internal shocks capable of particle acceleration might still be produced at jet middle scales (from 10^{13} to 10^{16} cm from the compact object), see e.g. Malzac (2013). Intermittent ejections at different velocities at time scales of hours to days could produce internal shocks at distances $\sim 10^{15} - 10^{16}$ cm which could in turn accelerate particles, while second-order Fermi process and shear acceleration are still plausible for continuous outflows at those scales.

Lastly, two shocks may be formed at the jet termination point where the jet advance is stopped by the ambient medium: a termination (or reverse) shock and a bow (or forward) shock. In those conditions, first-order Fermi process can be expected, although diffusion and convection in this region could dampen this process. These shocks happens at distances $\sim 10^{18}$ cm for a steady jet, but this structure is observed at jet head during the jet propagation and will be discussed in more details in the following parts of this thesis.

Due to the fact that a clear identification of the acceleration mechanism behind high-energy radiation is very arduous and that this thesis does not focus on these processes, we will only present here the basic properties of particle acceleration which are enough for our discussions. First of all, from the presence of magnetic fields, a particle of charge q cannot be accelerated if its Larmor radius is greater than the accelerator size l_a. This is the Hillas criterium (Hillas, 1984), which limits the highest achievable energy to:

$$E < qB_a l_a, \tag{10}$$

where B_a is the magnetic field in the accelerator region. Secondly, the result of particle acceleration by a stochastic or diffusive process presents an isotropic distribution of velocities in the emitter frame due to deflection in the randomic component of the local

magnetic field. Finally, the resulting energy distribution is a power-law $\propto E^{-h}$, with $h \sim 2$ in most cases considered (for instance, $h = 2$ in the case of non-relativistic diffusive acceleration by a strong shock in the test-particle limit).

Radiative output of accelerated particles

As mentioned section 0.3.2, the energy distribution of accelerated particles is typically taken with an index $h = 2$. The variety of processes and diversity of physical parameters in a microquasar results in vastly different spectral components as detailed in section 0.1.2, but the basic features of the evolved particle energy distribution can be obtained from the simple case of an homogeneous one-zone emitter with particle flux in the steady regime. In this simple model, the final energy distribution is of the form:

$$N(E) \propto \begin{cases} E^{-p} = E^{-h+1}/\dot{E} & \text{if } E > E_{min}, \\ 1/\dot{E} & \text{otherwise.} \end{cases} \tag{11}$$

The energy E_{min} is the minimum injection energy. Approximating $\dot{E} = -E/t_{cool} \propto E^g$, with t_{cool} the typical timescale of the main cooling process, the rough shape of the final energy distribution can be given from the energy dependency of each process considered: $g = 2$ for synchrotron and Thomson-regime inverse Compton (Thomson IC), $g \sim 0$ for inverse Compton in the Klein-Nishina regime (KN IC) and the ionization losses, $g \sim 1$ for free-free mechanism and proton-proton interactions, and $g = 1$ for adiabatic losses. We now want to obtain the shape of the spectral energy distribution $\nu F(\nu)$, with ν the emitted photon frequency and $F(\nu)$ the specific flux:

$$\begin{aligned} \nu F(\nu) = \nu^2 n(\nu) &= \int_{E_{min}(\nu)}^{E_{max}} N(E) P(E,\nu) dE \\ &\approx \nu \dot{E}_{rad}\left(E(\nu)\right) N\left(E(\nu)\right) \frac{dE(\nu)}{d\nu}, \end{aligned} \tag{12}$$

where $n(\nu)$ is the photon number. The last line is obtained by taking the delta function approximation for the specific power $P(E,\nu)$, which is approximately valid for the radiative processes considered. To push this analysis further, we adopt a dependency of the kind $E(\nu) \propto \nu^l$, which is roughly correct for the mechanisms considered here: $l = 1/2$ for synchrotron and Thomson IC, $l \approx 1$ for KN IC, free-free and proton-proton interactions. Thus, for a particle population emitting at a rate $\dot{E}_{rad}$ (given by the considered emission mechanism) and cooled at rate $\dot{E}_{cool}$ (given by the main cooling mechanism):

$$\begin{aligned} \nu F(\nu) &\propto \nu \frac{\dot{E}_{rad}\left(E(\nu)\right) E(\nu)^{1-h} \nu^{l-1}}{\dot{E}_{cool}\left(E(\nu)\right)} \\ &\propto \nu^{l(g_{rad}-g_{cool}+2-h)}. \end{aligned} \tag{13}$$

Below the minimum injection energy and escape energy, the delta function approximation is not valid anymore and the proper emissivity function of each mechanism needs to be accounted for. This simple scheme is further modified when taking into account more physics, such as the sometimes complex shapes for particle spectrum, the presence of cut-offs at low or high energy as well as extreme slopes or in case of multiple acceleration/emission zones. It nonetheless provides valuable insights into the formation of the observed spectral energy distribution.

0.3.3 Understanding the jets

Jets from AGN

The understanding of jets in microquasars started with the study of AGN jets. The first simulations were performed by Norman et al. (1982), with a 2D hydrodynamical jet propagating through a medium of uniform density. Their detailed results confirmed the picture suggested by Blandford & Rees (1974) of a jet head comprising a Mach disc, a contact discontinuity, and a bow shock, explaining the lobe structure of Cygnus A and other radio galaxies.

The following numerical studies further delved into the structure of relativistic jets, starting from simulations of axisymmetric jets. Martí et al. (1997) explored the evolution of their morphology and identified five dimensionless parameters sufficient to describe jets evolving into an uniform medium. Komissarov & Falle (1998) and Rosen et al. (1999) found lots of similarities between Newtonian and relativistic jets, noting that relativistic jets with high Lorentz factor generates smaller cocoons. 3D simulations were performed by Aloy et al. (1999), where the coherent backflow observed in axisymmetric jets could not be observed while the jets were found to be more stable than their axisymmetric counterparts.

The importance of the Kelvin-Helmholtz instability (KHI) in the jet structure was highlighted in Norman et al. (1984, 1985) as the mechanism behind the formation of observed knots in astrophysical jets. Bodo et al. (1994) divided the evolution of jets into phases depending on the growth of the KHI while the mechanisms behind this instability were further studied by e.g. Perucho et al. (2005, 2006).

The influence of the jet composition was investigated in Scheck et al. (2002) by performing simulations of pure leptonic and baryonic plasmas, which found the morphology and dynamics of the jets to be almost independant of its composition, although it affects the temperature in the cavities inflated by the interaction of the jet with the ambient medium by three orders of magnitude.

The inner structure of the jet was investigated through both hydro and magnetohydrodynamic models of radially stratified jets with a jet spine (Mizuno et al., 2007) which could be rotating (Meliani & Keppens, 2007, 2009), as this jet structuring plays an important role in explaining the morphology of high energy radiation emitted by the jet (Ghisellini et al., 2005; Hardcastle, 2006; Jester et al., 2006, 2007; Siemiginowska et al., 2007; Kataoka et al., 2008)

Jets from microquasars

A first approach to microquasar jets has been to compare them with their AGN counterparts to point out similarities between the two (Gómez, 2001; Hardee & Hughes, 2003) and study their interactions with the interstellar medium.

But in the case of high-mass microquasars, the jet also interacts with a strong stellar wind dominating the ambient medium. This wind may severely impact the jet dynamics on the orbital scale, destroying it before it could escape the binary. A strong shock is then likely to occur, leading to particle acceleration and radiation production. A phenomenological approach to this scenario was conducted by e.g. Romero et al. (2003); Romero & Orellana (2005) to explain γ-ray emission from these sources.

Perucho & Bosch-Ramon (2008) performed 2D simulations of high-mass microquasar jets in cylindrical and planar (slab) geometry at the orbital separation scale, crossing a perpendicular wind with physical parameters similar to those of sources LS 5039 and Cygnus X-1. They provided first estimates of the dynamical impact of the wind of an O-type star on a relativistic jet, suggesting that jets with kinetic power lower than $\sim 10^{36}$ erg s^{-1} could be bent or disrupted. This study was then continued with 3D simulations (Perucho et al., 2010b), raising the disruption limit to a few 10^{36} erg s^{-1} and highlighting the effects of asymmetric Kelvin-Helmholtz instability in jet distortions and disruptions.

A companion paper (Perucho et al., 2010a) highlighted the formation and evolution of a recollimation shock close to jet injection and its potential role in particle acceleration in high-mass microquasars. A larger-scale, non-relativistic, study was performed by Yoon & Heinz (2015) with a simulation box scale of $\sim$ 15 orbital distance, focusing on jet bending at larger scales and obtaining a simple analytical formula for the asymptotic bending angle. A follow up study by Yoon et al. (2016) reconsidered the formation of a recollimation shock, emphasising that such a shock is likely present in Cygnus X-1 while the situation in Cygnus X-3 is less clear.

In addition to the wind thrust, orbital motion may also have an influence on the jet dynamics on large scales, inducing an helical pattern in the jet. Bosch-Ramon & Barkov (2016) characterised this effect through analytical estimates, suggesting the combined effects of wind and binary motion can induce not only non-ballistic helical jet trajectories, but also partial disruption and mixing, asymmetric recollimation shocks and possibly non-thermal emission.

Outline

The present work adds to this picture with a set of 3D hydrodynamical simulations that distinguish themselves from existing work in that they are relativistic, include radiative cooling, and follow the jet evolution over comparatively large spatial distances of around 20 to 75 orbital separations. The comparatively large spatial domain allows us to follow jet evolution from an initial, smooth phase through the non-linear growth of instabilities to a turbulent, auto-similar state, thereby creating a larger scale perspective for some of the results cited above. The parameter study we performed with this general setup is anchored at system parameters inspired by Cygnus X-1 (Orosz et al., 2011) where cooling is moderate, and Cygnus X-3 (Zdziarski et al., 2013) where a strong cooling effect occurs due to the combination of a stronger stellar wind, magnetic field and luminosity with an orbital separation one order of magnitude smaller than in the former.

We obtain typical time scales for the initial instability growth depending on the various parameters and the presence of cooling, highlighting the importance of the beam internal shocks in the growth of the Kelvin-Helmholtz instability and therefore jet structure and dynamics. Cooling is found to play a role only in Cygnus X-3 on the scales covered by our simulations. Once cooling becomes dominant, the jet cocoon is immediately blown away by the stellar wind. Our simulations further suggest that the parameter sensitivities explored somewhat diminish or are more difficult to clearly diagnose later on, when the jet has become fully turbulent. We confirm earlier findings that a too large wind power breaks the jet. We find a strong instability developing at the jet beam - cocoon interface that destroys the beam. A turbulent expanding region develops subsequently, that eventually

expands away from the orbital plane and the jet is recovered. We ultimately took steps towards obtaining the spectral signatures of our jets.

This thesis is organized as follows: in chapter 1, we present the physics of hydrodynamical relativistic jets. The volumic losses from thermal, optically thin, relativistic plasmas are derived in chapter 2, as well as the emission coefficient corresponding to the same radiative processes. In chapter 3, we describe the numerical methods used during this PhD: the A-MaZe toolkit used to perform jet simulations, the post-processing code developed for these studies, concluding with the presentation of a numerical method to calculate the radiations emitted by our hydrodynamical simulations. Lastly, we discuss in 4 the jet propagation, destabilization and structure with the cooling and simulation parameters. The results obtained are summarized and discussed in the Conclusion before presenting the outlooks of this thesis.

Bibliography

Abramowicz M. A., Calvani M., Nobili L., 1989, Accretion: A Collection of Influential Papers, p. 251

Ajello M., et al., 2013, The Astrophysical Journal, 780, 73

Aloy M. A., Ibáñez J. M., Martí J. M., Gómez J.-L., Müller E., 1999, The Astrophysical Journal, 523, L125

Bardeen J. M., 1970, Nature, 226, 64

Bardeen J. M., Petterson J. A., 1975, The Astrophysical Journal, 195, L65

Bardeen J. M., Press W. H., Teukolsky S. A., 1972, The Astrophysical Journal, 178, 347

Beckmann V., et al., 2007, A&A, 473, 903

Begelman M., Meier D., 1982, The Astrophysical Journal, 253, 873

Belloni T. M., Motta S. E., 2016, Transient Black Hole Binaries. p. 61, doi:10.1007/978-3-662-52859-4_2

Belloni T. M., Motta S. E., Muñoz-Darias T., 2011, Bulletin of the Astronomical Society of India, 39, 409

Berger M., van der Klis M., 1994, A&A, 292, 175

Bignami G., et al., 1981, Astronomy and Astrophysics, 93, 71

Blandford R., Payne D., 1982, Monthly Notices of the Royal Astronomical Society, 199, 883

Blandford R., Rees M., 1974, Monthly Notices of the Royal Astronomical Society, 169, 395

Blandford R. D., Rees M. J., 1978, Physica Scripta, 17, 265

Blandford R. D., Znajek R. L., 1977, Monthly Notices of the Royal Astronomical Society, 179, 433

Blandford R., Meier D., Readhead A., 2019, Annual Review of Astronomy and Astrophysics, 57, 467

Bodo G., Massaglia S., Ferrari A., Trussoni E., 1994, Astronomy and Astrophysics, 283, 655

Bolton C. T., 1972, Nature, 235, 271

Bosch-Ramon V., 2008, arXiv preprint arXiv:0805.1707

Bosch-Ramon V., Barkov M., 2016, Astronomy & Astrophysics, 590, A119

Bouchet L., et al., 2003, Astronomy & Astrophysics, 411, L377
Bowyer S., Byram E., Chubb T., Friedman H., 1965, Science, 147, 394
Brocksopp C., 1998, A&A, 343, 861
Brocksopp C., et al., 2002, Monthly Notices of the Royal Astronomical Society, 331, 765
Bulgarelli A., et al., 2012, A&A, 538, A63
Burbidge G. R., 1956, The Astrophysical Journal, 124, 416
Cangemi F., Rodriguez J., Grinberg V., Laurent P., Wilms J., 2018, in Di Matteo P., Billebaud F., Herpin F., Lagarde N., Marquette J. B., Robin A., Venot O., eds, SF2A-2018: Proceedings of the Annual meeting of the French Society of Astronomy and Astrophysics. p. Di (arXiv:1810.12049)
Cangemi F., Rodriguez J., Grinberg V., Belmont R., Laurent P., Wilms J., 2021a, A&A, 645, A60
Cangemi F., et al., 2021b, Astronomy & Astrophysics, 650, A93
Capitanio F., et al., 2008, The Astrophysical Journal, 690, 1621
Capitanio F., Belloni T., Del Santo M., Ubertini P., 2009, Monthly Notices of the Royal Astronomical Society, 398, 1194
Casares J., Charles P. A., Naylor T., 1992, Nature, 355, 614
Chauvin M., et al., 2018, Nature Astronomy, 2, 652
Cheung C., Harris D., et al., 2007, The Astrophysical Journal Letters, 663, L65
Coppi P. S., 1999, in Poutanen J., Svensson R., eds, Astronomical Society of the Pacific Conference Series Vol. 161, High Energy Processes in Accreting Black Holes. p. 375 (arXiv:astro-ph/9903158)
Corbel S., Fender R., Tomsick J., Tzioumis A., Tingay S., 2004, The Astrophysical Journal, 617, 1272
Corbel S., Kaaret P., Fender R., Tzioumis A., Tomsick J., Orosz J., 2005, The Astrophysical Journal, 632, 504
Corbel S., et al., 2012, MNRAS, 421, 2947
Crinquand B., Cerutti B., Dubus G., 2019, Astronomy & Astrophysics, 622, A161
Davidsen A., Ostriker J. P., 1974, The Astrophysical Journal, 189, 331
Davis S. W., Tchekhovskoy A., 2020, Annual Review of Astronomy and Astrophysics, 58, 407
Del Santo M., Malzac J., Belmont R., Bouchet L., De Cesare G., 2013, Monthly Notices of the Royal Astronomical Society, 430, 209
Dent W., 1965, Science, 148, 1458
Derishev E. V., Aharonian F., Kocharovsky V., Kocharovsky V. V., 2003, Physical Review D, 68, 043003
Done C., Gierliński M., Kubota A., 2007, The Astronomy and Astrophysics Review, 15, 1
Drury L. O., 1983, Reports on Progress in Physics, 46, 973
Duro R., et al., 2016, Astronomy & Astrophysics, 589, A14
Eardley D. M., Lightman A. P., Shapiro S. L., 1975, The Astrophysical Journal, 199, L153
Ebisawa K., Ueda Y., Inoue H., Tanaka Y., White N. E., 1996, The Astrophysical Journal, 467, 419
Elvis M., Page C., Pounds K., Ricketts M., Turner M., 1975, Nature, 257, 656

Esin A. A., McClintock J. E., Narayan R., 1997, The Astrophysical Journal, 489, 865
Fath E. A., 1909, Publications of the Astronomical Society of the Pacific, 21, 138
Fender R. P., 2001, Monthly Notices of the Royal Astronomical Society, 322, 31
Fender R. P., Hanson M., Pooley G., 1999, Monthly Notices of the Royal Astronomical Society, 308, 473
Fender R., Belloni T., Gallo E., 2004, Monthly Notices of the Royal Astronomical Society, 355, 1105
Fermi E., 1949, Physical review, 75, 1169
Fermi LAT Collaboration 2009, Science, 326, 1512
Ferrigno C., Bozzo E., Del Santo M., Capitanio F., 2012, Astronomy & Astrophysics, 537, L7
Fomalont E., Geldzahler B., Bradshaw C., 2001, The Astrophysical Journal, 558, 283
Frontera F., et al., 2001, The Astrophysical Journal, 546, 1027
Garcia J., Dauser T., Reynolds C., Kallman T., McClintock J., Wilms J., Eikmann W., 2013, The Astrophysical Journal, 768, 146
Ghisellini G., Tavecchio F., Chiaberge M., 2005, Astronomy & Astrophysics, 432, 401
Giacconi R., Gorenstein P., Gursky H., Waters J., 1967, The Astrophysical Journal, 148, L119
Gierliński M., Done C., 2003, Monthly Notices of the Royal Astronomical Society, 342, 1083
Gierliński M., Zdziarski A. A., Poutanen J., Coppi P. S., Ebisawa K., Johnson W. N., 1999, Monthly Notices of the Royal Astronomical Society, 309, 496
Gies D., Bolton C., 1986, The Astrophysical Journal, 304, 389
Gilfanov M., 2010, in , The Jet Paradigm. Springer, pp 17–51
Gómez J.-L., 2001, in Castro-Tirado A. J., Greiner J., Paredes J. M., eds, Microquasars. Springer Netherlands, Dordrecht, pp 281–288
Grinberg V., et al., 2013, Astronomy & Astrophysics, 554, A88
Haardt F., Maraschi L., Ghisellini G., 1994, ApJ, 432, L95
Hannikainen D., Hunstead R., Campbell-Wilson D., Wu K., McKay D., Smits D., Sault R., 2000, The Astrophysical Journal, 540, 521
Hannikainen D., Campbell-Wilson D., Hunstead R., McIntyre V., Lovell J., Reynolds J., Tzioumis T., Wu K., 2001, in , Microquasars. Springer, pp 45–50
Hanson M., Still M., Fender R. P., 2000, The Astrophysical Journal, 541, 308
Hardcastle M., 2006, Monthly Notices of the Royal Astronomical Society, 366, 1465
Hardee P. E., Hughes P. A., 2003, The Astrophysical Journal, 583, 116
Hazard C., Mackey M., Shimmins A., 1963, Nature, 197, 1037
Hertz P., Joss P. C., Rappaport S., 1978, ApJ, 224, 614
Hillas A. M., 1984, Annual review of astronomy and astrophysics, 22, 425
Hjalmarsdotter L., Zdziarski A. A., Szostek A., Hannikainen D. C., 2008, Monthly Notices of the Royal Astronomical Society, 392, 251
Homan J., Buxton M., Markoff S., Bailyn C. D., Nespoli E., Belloni T., 2005, The Astrophysical Journal, 624, 295
Homan J., Wijnands R., Kong A., Miller J. M., Rossi S., Belloni T., Lewin W. H., 2006, Monthly Notices of the Royal Astronomical Society, 366, 235
Hughes M., 1965, Nature, 207, 178

Hurst G., 1989, Journal of the British Astronomical Association, 99, 161
Jansky K. G., 1933, Nature, 132, 66
Jennison R., Gupta M. D., 1953, Nature, 172, 996
Jester S., Harris D., Marshall H. L., Meisenheimer K., 2006, The Astrophysical Journal, 648, 900
Jester S., Meisenheimer K., Martel A. R., Perlman E. S., Sparks W. B., 2007, Monthly Notices of the Royal Astronomical Society, 380, 828
Joinet A., Jourdain E., Malzac J., Roques J., Schönfelder V., Ubertini P., Capitanio F., 2005, The Astrophysical Journal, 629, 1008
Kajava J., Motta S. E., Sanna A., Veledina A., Del Santo M., Segreto A., 2019, Monthly Notices of the Royal Astronomical Society: Letters, 488, L18
Kantzas D., et al., 2021, Monthly Notices of the Royal Astronomical Society, 500, 2112
Kataoka J., et al., 2008, The Astrophysical Journal, 685, 839
Keel W. C., 1983, The Astrophysical Journal, 269, 466
Kim J.-Y., et al., 2018, Astronomy & Astrophysics, 616, A188
King A., Pringle J., 2021, accepted for publication in ApJL
King A., Lasota J., Kundt W., 1975, Physical Review D, 12, 3037
Koljonen K. I. I., Maccarone T. J., 2017, Monthly Notices of the Royal Astronomical Society, 472, 2181
Koljonen K. I. I., Hannikainen D. C., McCollough M. L., Pooley G. G., Trushkin S. A., 2010, Monthly Notices of the Royal Astronomical Society, 406, 307
Koljonen K. I. I., Maccarone T., McCollough M. L., Gurwell M., Trushkin S. A., Pooley G. G., Piano G., Tavani M., 2018, A&A, 612, A27
Komissarov S., 2004, Monthly Notices of the Royal Astronomical Society, 350, 427
Komissarov S. S., 2021, arXiv preprint arXiv:2108.08161
Komissarov S. S., Falle S. A. E. G., 1998, Monthly Notices of the Royal Astronomical Society, 297, 1087
Komissarov S., Porth O., 2021, New Astronomy Reviews, p. 101610
Körding E., Fender R., Migliari S., 2006, Monthly Notices of the Royal Astronomical Society, 369, 1451
Kuulkers E., Howell S. B., van Paradijs J., 1996, The Astrophysical Journal Letters, 462, L87
Lasota J.-P., 2001, New Astronomy Reviews, 45, 449
Lewis F., et al., 2010, Astronomy & Astrophysics, 517, A72
Liska M., Tchekhovskoy A., Quataert E., 2020, Monthly Notices of the Royal Astronomical Society, 494, 3656
Livio M., Ogilvie G., Pringle J., 1999, The Astrophysical Journal, 512, 100
Lynden-Bell D., 1969, Nature, 223, 690
Makino F., 1989, International Astronomical Union Circular, 4782, 1
Malzac J., 2013, Monthly Notices of the Royal Astronomical Society: Letters, 429, L20
Malzac J., 2014, Monthly Notices of the Royal Astronomical Society, 443, 299
Malzac J., et al., 2006, Astronomy & Astrophysics, 448, 1125
Marcel G., et al., 2018a, Astronomy & Astrophysics, 615, A57
Marcel G., et al., 2018b, Astronomy & Astrophysics, 617, A46
Marcel G., et al., 2019, Astronomy & Astrophysics, 626, A115

Markert T., Canizares C., Clark G., Lewin W., Schnopper H., Sprott G., 1973, The Astrophysical Journal, 184, L67
Martí J. M., Müller E., Font J., Ibáñez J. M. Z., Marquina A., 1997, The Astrophysical Journal, 479, 151
Martí J., Paredes J. M., Peracaula M., 2000, The Astrophysical Journal, 545, 939
McClintock J., Remillard R., 1986, The Astrophysical Journal, 308, 110
McClintock J. E., Remillard R. A., 2006, Black hole binaries. pp 157–213
McClintock J. E., Remillard R. A., Rupen M. P., Torres M. A., Steeghs D., Levine A. M., Orosz J. A., 2009, The Astrophysical Journal, 698, 1398
McCollough M., et al., 1999, The Astrophysical Journal, 517, 951
McConnell M. L., et al., 2002, The Astrophysical Journal, 572, 984
Meier D. L., 1999, The Astrophysical Journal, 522, 753
Meier D. L., 2001, The Astrophysical Journal Letters, 548, L9
Meier D. L., 2003, New Astronomy Reviews, 47, 667
Meliani Z., Keppens R., 2007, Astronomy & Astrophysics, 475, 785
Meliani Z., Keppens R., 2009, The Astrophysical Journal, 705, 1594
Migliari S., Fender R., 2006, Monthly Notices of the Royal Astronomical Society, 366, 79
Miller-Jones J. C., et al., 2021, Science, 371, 1046
Mioduszewski A. J., Rupen M. P., Hjellming R. M., Pooley G. G., Waltman E. B., 2001, The Astrophysical Journal, 553, 766
Mirabel I., Rodriguez L., 1994, Nature, 371, 46
Mirabel I., Rodriguez L., Cordier B., Paul J., Lebrun F., 1992, Nature, 358, 215
Miyamoto S., Iga S., Kitamoto S., Kamado Y., 1993, The Astrophysical Journal, 403, L39
Miyamoto S., Kitamoto S., Hayashida K., Egoshi W., 1995, The Astrophysical Journal, 442, L13
Mizuno Y., Hardee P., Nishikawa K.-I., 2007, The Astrophysical Journal, 662, 835
Motta S., Belloni T., Homan J., 2009, Monthly Notices of the Royal Astronomical Society, 400, 1603
Motta S., Homan J., Munoz-Darias T., Casella P., Belloni T., Hiemstra B., Méndez M., 2012, Monthly Notices of the Royal Astronomical Society, 427, 595
Motta S., Rouco-Escorial A., Kuulkers E., Muñoz-Darias T., Sanna A., 2017, Monthly Notices of the Royal Astronomical Society, 468, 2311
Motta S., et al., 2021, New Astronomy Reviews, p. 101618
Muñoz-Darias T., Fender R., Motta S., Belloni T., 2014, Monthly Notices of the Royal Astronomical Society, 443, 3270
Muñoz-Darias T., et al., 2016, Nature, 534, 75
Narayan R., Yi I., 1994, arXiv preprint astro-ph/9403052
Neronov A., Aharonian F. A., 2007, The Astrophysical Journal, 671, 85
Norman M. L., Winkler K.-H., Smarr L., Smith M., 1982, Astronomy and Astrophysics, 113, 285
Norman M. L., Winkler K.-H., Smarr L., 1984, pete, p. 150
Norman M. L., Smarr L., Winkler K.-H. A., 1985, nuas, p. 88
Oke J., Gunn J., 1974, The Astrophysical Journal, 189, L5
Orosz J. A., Hauschildt P. H., 2000, arXiv preprint astro-ph/0010114

Orosz J. A., McClintock J. E., Aufdenberg J. P., Remillard R. A., Reid M. J., Narayan R., Gou L., 2011, APJ, 742, 84
Parfrey K., Philippov A., Cerutti B., 2019, Physical review letters, 122, 035101
Parsignault D. R., et al., 1972, Nature Physical Science, 239, 123
Patruno A., Maitra D., Curran P., D'Angelo C., Fridriksson J., Russell D., Middleton M., Wijnands R., 2016, The Astrophysical Journal, 817, 100
Pepe C., Vila G. S., Romero G. E., 2015, Astronomy & Astrophysics, 584, A95
Perucho M., Bosch-Ramon V., 2008, Astronomy & Astrophysics, 482, 917
Perucho M., Marti J.-M., Hanasz M., 2005, Astronomy & Astrophysics, 443, 863
Perucho M., Lobanov A. P., Martí J. M., Hardee P. E., 2006, A&A, 456, 493
Perucho M., Bosch-Ramon V., Khangulyan D., 2010a, International Journal of Modern Physics D, 19, 791
Perucho M., Bosch-Ramon V., Khangulyan D., 2010b, Astronomy & Astrophysics, 512, L4
Pottschmidt K., et al., 2003, Astronomy & Astrophysics, 411, L383
Poutanen J., Svensson R., 1996, ApJ, 470, 249
Punch M., et al., 1992, nature, 358, 477
Reber G., 1940, Proceedings of the IRE, 28, 68
Rees M., 1966, Nature, 211, 468
Rees M., 1971, Nature, 229, 312
Reid M. J., McClintock J. E., Narayan R., Gou L., Remillard R. A., Orosz J. A., 2011, The Astrophysical Journal, 742, 83
Rieger F., Aharonian F., 2008, Astronomy & Astrophysics, 479, L5
Rieger F. M., Duffy P., 2004, The Astrophysical Journal, 617, 155
Rieger F. M., Bosch-Ramon V., Duffy P., 2007, in , The Multi-Messenger Approach to High-Energy Gamma-Ray Sources. Springer, pp 119–125
Romero G. E., Orellana M., 2005, A&A, 439, 237
Romero G. E., Torres D. F., Kaufman Bernadó M. M., Mirabel I. F., 2003, A&A, 410, L1
Romero G. E., Vieyro F. L., Chaty S., 2014, Astronomy & Astrophysics, 562, L7
Rosen A., Hughes P. A., Duncan G. C., Hardee P. E., 1999, The Astrophysical Journal, 516, 729
Russell D., Gallo E., Fender R., 2013, Monthly Notices of the Royal Astronomical Society, 431, 405
Safarzadeh M., Loeb A., Reid M., 2019, Monthly Notices of the Royal Astronomical Society: Letters, 488, L90
Salpeter E., 1964, Publications, 1, 165
Salvo T. D., Done C., Życki P. T., Burderi L., Robba N. R., 2001, The Astrophysical Journal, 547, 1024
Sandage A., 1965, The Astrophysical Journal, 141, 1560
Schatz H., Rehm K., 2006, Nuclear physics A, 777, 601
Scheck L., Aloy M., Martí J., Gómez J., Müller E., 2002, Monthly Notices of the Royal Astronomical Society, 331, 615
Scheuer P., 1974, Monthly Notices of the Royal Astronomical Society, 166, 513
Schmidt M., 1963, Nature, 197, 1040
Schmitt J. L., 1968, Nature, 218, 663

Schreier E. J., Gorenstein P., Feigelson E. D., 1982, The Astrophysical Journal, 261, 42
Seyfert C. K., 1943, The Astrophysical Journal, 97, 28
Shakura N. I., Sunyaev R. A., 1973, Astronomy and Astrophysics, 24, 337
Shapiro S. L., Lightman A. P., Eardley D. M., 1989, Accretion: A Collection of Influential Papers, p. 277
Shklovskii I., 1955, Astron. J. USSR, 32, 215
Siemiginowska A., Stawarz Ł., Cheung C., Harris D., Sikora M., Aldcroft T. L., Bechtold J., 2007, The Astrophysical Journal, 657, 145
Singh N., Naik S., Paul B., Agrawal P., Rao A., Singh K., 2002, Astronomy & Astrophysics, 392, 161
Smith H. J., Hoffleit D., 1963, The Astronomical Journal, 68, 292
Soleri P., et al., 2013, Monthly Notices of the Royal Astronomical Society, 429, 1244
Stern B. E., Poutanen J., 2008, Monthly Notices of the Royal Astronomical Society, 383, 1695
Sturner S., Shrader C., 2005, The Astrophysical Journal, 625, 923
Sunyaev R., Titarchuk L., 1980, Astronomy and Astrophysics, 86, 121
Svoboda J., Guainazzi M., Merloni A., 2017, Astronomy & Astrophysics, 603, A127
Szostek A., Zdziarski A. A., 2008, Monthly Notices of the Royal Astronomical Society, 386, 593
Tanaka Y., 1995, X-Ray Binaries, eds. WHG Lewin, J. van Paradijs, & EPJ van den Heuvel
Tananbaum H., Gursky H., Kellogg E., Giacconi R., Jones C., 1972, The Astrophysical Journal, 177, L5
Tavani M., et al., 2009, Nature, 462, 620
Tout C. A., Pringle J., 1996, Monthly Notices of the Royal Astronomical Society, 281, 219
Uttley P., Klein-Wolt M., 2015, Monthly Notices of the Royal Astronomical Society, 451, 475
Van Der Klis M., 1996, in Symposium-International Astronomical Union. pp 301–312
Van Kerkwijk M., 1993, Astronomy and Astrophysics, 276, L9
Van Kerkwijk M., et al., 1992, Nature, 355, 703
Van Kerkwijk M., Geballe T., King D., Van Der Klis M., Van Paradijs J., 1996, arXiv preprint astro-ph/9604100
Van der Klis M., 1997, Advances in Space Research, 19, 75
Vilhu O., Hakala P., Hannikainen D., McCollough M., Koljonen K., 2009, Astronomy & Astrophysics, 501, 679
Wald R. M., 1974, Physical Review D, 10, 1680
Walder R., Melzani M., Folini D., Winisdoerffer C., Favre J. M., 2014, arXiv preprint arXiv:1405.0600
Walker R. C., Hardee P. E., Davies F. B., Ly C., Junor W., 2018, The Astrophysical Journal, 855, 128
Webster B. L., Murdin P., 1972, Nature, 235, 37
Wiita P. J., 1982, The Astrophysical Journal, 256, 666
Yoon D., Heinz S., 2015, The Astrophysical Journal, 801, 55
Yoon D., Zdziarski A. A., Heinz S., 2016, Monthly Notices of the Royal Astronomical

Society, 456, 3638
Yuan F., Narayan R., 2014, Annual Review of Astronomy and Astrophysics, 52, 529
Zdziarski A. A., Gierliński M., 2004, Progress of Theoretical Physics Supplement, 155, 99
Zdziarski A. A., Poutanen J., Paciesas W. S., Wen L., 2002, The Astrophysical Journal, 578, 357
Zdziarski A. A., Gierlinski M., Mikolajewska J., Wardzinski G., Smith D. M., Alan Harmon B., Kitamoto S., 2004, Monthly Notices of the Royal Astronomical Society, 351, 791
Zdziarski A. A., Misra R., Gierliński M., 2010, Monthly Notices of the Royal Astronomical Society, 402, 767
Zdziarski A. A., Lubiński P., Sikora M., 2012, Monthly Notices of the Royal Astronomical Society, 423, 663
Zdziarski A. A., Mikołajewska J., Belczyński K., 2013, MNRAS: Letters, 429, L104
Zel'dovich Y. B., Novikov I. D., 1964, in Doklady Akademii Nauk. pp 811–814
Zenitani S., Hoshino M., 2001, The Astrophysical Journal Letters, 562, L63

Chapter 1

Relativistic hydrodynamical jets

We begin with a summary of our knowledge on hydrodynamical relativistic jets. In section 1.1.1, we present the equations for special relativistic hydrodynamics (SRHD) used to described such outflows. Instabilities, mainly the Kelvin-Helmholtz instability, decide the long-term evolution of jets. A model to derive an estimate of growth times is given section 1.2. We then present 1.3 an overview of the morphology of relativistic jets, as identified in previous studies of AGN jets, before exposing the modifications to this picture introduced by MHD simulations for clearer understanding of those objects. Then, the known effects of stellar winds on the jet in a high-mass microquasar are presented section 1.5.

1.1 Special relativistics hydrodynamics

1.1.1 Covariant hydrodynamics

The covariant equations in special relativistic hydrodynamics are (e.g. Landau & Lifshitz, 1959; Mihalas & Mihalas, 1984):

$$\partial_\alpha(\rho u^\alpha) = 0, \tag{1.1}$$

$$\partial_\alpha T^{\alpha\beta} = 0, \tag{1.2}$$

where Greek indices α, β indicate 4D space-time tensor components, while Latin indices i, j will be used for 3D spatial tensor components. $T^{\alpha\beta} \equiv \rho h u^\alpha u^\beta + p g^{\alpha\beta}$ is the energy-momentum tensor of the flow. The metric tensor $g^{\alpha\beta}$ defines space-time properties, here a Minkowski flat space $g^{\alpha\beta} = \mathrm{diag}\{-1, 1, 1, 1\}$ with coordinates $x^\alpha = (t, x^i)$ will be assumed. The physical quantities are the rest mass density ρ, the thermal pressure p, the relativistic specific enthalpy $h \equiv c^2 + \epsilon + p/\rho$ (ϵ is the specific internal energy) and the 4-velocity $u^\alpha = (\gamma c, \gamma\vec{v})$, where $\gamma \equiv (1 - v^2/c^2)^{-1/2}$ is the Lorentz factor. The system is closed with an ideal gas equation of state with adiabatic index Γ:

$$\epsilon(\rho, p) = p/(\Gamma - 1)\rho. \tag{1.3}$$

The specific enthalpy can thus be written as: $h = c^2 + \Gamma_1 p/\rho$, with $\Gamma_1 \equiv \Gamma/(\Gamma - 1)$. Equations 1.1 and 1.2 can then be cast to obtain the covariant equations for 3D special

relativistics hydrodynamics:

$$\partial_t(\gamma\rho) + \partial_i(\gamma\rho v^i) = 0, \tag{1.4}$$
$$\partial_t(\gamma^2\rho h v^j) + \partial_i(\gamma^2\rho h v^i v^j + pc^2\delta^{ij}) = 0, \tag{1.5}$$
$$\partial_t(\gamma^2\rho h - p) + \partial_i(\gamma^2\rho h v^i) = 0. \tag{1.6}$$

Introducing the conserved relativistic densities of rest-mass $D = \gamma\rho$, momentum $S^i = \gamma^2\rho h v^i$, and energy $\tau = \gamma^2\rho h - p$, also coined as the *conservative* variables, we can rewrite the SRHD equations as:

$$\partial_t\mathcal{U} + \partial_i\mathcal{F}^i = 0, \tag{1.7}$$

where the conservative variables and the corresponding fluxes in the i direction are given by:

$$\mathcal{U} = \begin{bmatrix} D \\ S^j \\ \tau \end{bmatrix}, \quad \mathcal{F}^i = \begin{bmatrix} Dv^i \\ S^j v^i + p\delta^{ij} \\ S^i \end{bmatrix}. \tag{1.8}$$

In the rest of this work, quantities with subscript b, ic and oc will refer respectively to the beam, inner cocoon, and outer cocoon, which will be defined properly section 1.3. Values with subscript w refer to the stellar wind, and j to either injection parameters, or, in some cases of chapter 2, to the local flow of the jet to avoid ambiguities.

1.1.2 Model for jet propagation

We generalize the model for the propagation of a relativistic jet as derived by e.g. Martí et al. (1997) and Mizuta et al. (2004), where multidimensional effects are neglected and one-dimensional momentum balance between the beam with velocity v_b and the ambient gas is assumed in the rest frame of the contact discontinuity at the head of the jet, to the case of an ambient medium with its own (non-relativistic) flow speed v_w. The momentum balance writes:

$$S_b\left[\rho_b h_b \gamma_h^2\gamma_b^2(v_b - v_h)^2 + p_b\right] = S_w\left[\rho_w h_w \gamma_h^2(v_w - v_h)^2 + p_w\right] \tag{1.9}$$

with γ_h the Lorentz factor of jet head propagation speed v_h, S_b and S_w are the cross-section of the beam and jet head. Solving equation 1.9 for v_h, we obtain:

$$v_h = \frac{1}{A\eta^* - 1}\sqrt{A\eta^*(v_b - v_w)^2 - (A\eta^* - 1)\frac{(AK-1)c_{s,w}^2}{\gamma_h^2\Gamma}}, \tag{1.10}$$

with $A \equiv S_b/S_w$ the cross-section ratio and η^* the injected-to-ambient ratio of inertial density $\gamma^2\rho h$. The sound speed of the ambient medium $c_{s,w}$ is negligible before the beam flow speed v_b, therefore we neglect the last term in the square root. We also assume $A = 1$, obtaining the final equation:

$$v_h = \frac{\eta^* v_b - v_w - \sqrt{\eta^*}(v_b - v_w)}{\eta^* - 1}. \tag{1.11}$$

Equation 1.11 recovers the equation derived in e.g. Martí et al. (1997) and Mizuta et al. (2004) by taking $v_w = 0$. This model is useful to describe the early jet evolution, but

several effects such as the growth of instabilities limits its applicability to longer term dynamics. One can also cite jet propagation models which take deceleration into account such as the extended Begelman-Cioffi model from Scheck et al. (2002) and the decelerated momentum balance from Mukherjee et al. (2020), but these models are not adapted to fit the dynamics of our high-mass microquasars jets as they were developed in the context of AGN jets.

1.2 Instabilities in relativistic jets

1.2.1 General picture

During the jet propagation, various hydrodynamical instabilities can be triggered and then perturb the beam, reducing the effective beam speed at the front shock and decelerating the jet. One can first cite the Kelvin-Helmholtz instability (KHI) at relativistic flow interface, which has been extensively studied: Turland & Scheuer (1976); Blandford & Pringle (1976); Ferrari et al. (1978); Hardee (1979); Bodo et al. (1994); Hanasz & Sol (1998); Hardee et al. (1998, 2001); Perucho et al. (2004a,b, 2005); Mizuno et al. (2007); Rossi et al. (2008); Perucho et al. (2010c).

Then, the Rayleigh-Taylor instability (RTI) can be triggered when a lighter fluid supports an heavier one against gravity, or equivalently if the lighter fluid accelerates the heavier one (see Norman et al. 1982; Allen & Hughes 1984; Duffell & MacFadyen 2011 for non-relativistic flows, Matsumoto et al. 2017 for relativistic flows), impacting the jet structures stability when the jet expands radially due to the centrifugal force as studied in e.g. Meliani & Keppens (2007, 2009); Millas et al. (2017) or oscillates radially because of a pressure gradient, see Matsumoto & Masada (2013); Toma et al. (2017). RTI typically manifests as finger-like structures at the interface, induced by an inward pressure gradient.

Other instabilities include the Richtmyer-Meshkov instability (RMI) which develops when a shockwave crosses a corrugated interface separating two fluids with different thermodynamic properties (e.g. the finger-like structures created by the growth of RTI, see Nishihara et al. (2010) for a review and Matsumoto & Masada (2013) for a numerical study), and the Centrifugal instability (CFI) induced by the beam rotation, studied in Gourgouliatos & Komissarov (2018). Finally, let us cite vortex formation and shedding at the contact discontinuity of jet head (see e.g. Norman et al., 1982; Scheck et al., 2002; Mizuta et al., 2004), which increases cross-section of the jet head which therefore diminishes the jet propagation speed. The vortices may also perturb beam flow when they encounter it while propagating in the inner cocoon. Norman et al. (1982) noted the importance of the beam Mach number in the vortex shedding phenomenon, observing that lower Mach numbers produce larger vortices.

Following the footsteps of previous works on relativistic jets structure, this work will focus specifically on KHI through section 1.2.2 as other instabilities develop at the beam radius scale, meaning most of their modes do not appear in large-scale simulations due to grid resolution limitations. We confirm this assumption by deriving a timescale for the growth of the Rayleigh-Taylor instability section 1.2.3

1.2.2 Kelvin-Helmholtz instability

The first works on linear analysis of KHI in relativistic jets were done in Turland & Scheuer (1976) and Blandford & Pringle (1976), who derived and solved a dispersion relation for a single plane boundary between a relativistic flow and the ambient medium. Next, the properties of KHI in cylindrical jets were studied by Ferrari et al. (1978) and Hardee (1979) from the derivation of the dispersion relation in the nonrelativistic case, using the vortex sheet approximation. After numerically solving the dispersion relation, they identified unstable KH modes and classified them into two families: the fundamental and reflection modes. This classification is related to the number of nodes (which we called oblique shocks in section 1.3) across the jet, formed from the composition of oblique waves for which the jet beam is a resonant cavity. Then, Payne & Cohn (1985) discussed the physical meaning of KHI in supersonic jets, showing that the presence of instabilities is associated with overreflection of sound waves on the sheared jet boundaries.

Further studies included the effects of a shear layer replacing the vortex sheet in the nonrelativistic planar case (Ferrari et al., 1982; Ray, 1982; Choudhury & Lovelace, 1984), and those of conical or cylindrical geometry (Birkinshaw, 1984; Hardee, 1984, 1986, 1987). The effects of a cylindrical shear layer in a jet + sheath + ambient medium situation were investigated by Hanasz & Sol (1996, 1998).

An extension to the weakly nonlinear regime has been performed in Hanasz (1995), leading to the conclusion that various nonlinear effects causes KHI to saturate at finite amplitudes. Hanasz (1997) suggested that these nonlinearities result from the relativistic nature of the jet flow, and more precisely from the velocity perturbation not exceeding c in the jet reference frame, which was confirmed by numerical simulations (Perucho et al., 2004a,b).

Studies in the purely nonlinear regime demonstrated that jets with high Lorentz factors and a high internal energy are the most stable (Martí et al., 1997; Hardee et al., 1998; Rosen et al., 1999), further strengthening the inertial density $\xi = \gamma^2 \rho h$ as the main parameter for jet propagation efficiency. The predicted linear modes of KHI do not grow in those cases, which is interpreted as the consequence of a lack of appropriate perturbations as KHI is expected to develop with the highest growth rate in the high internal energy limit.

Linear and nonlinear approaches of jet stability in the relativistic case were combined for the first time by Hardee et al. (1998) in the case of axisymmetric, cylindrical jets, before being extended to the 3D case by Hardee et al. (2001) in the spatial approach, which consists on studying the evolution of a perturbation as it propagates along the jet. The temporal approach, which studies the evolution of a perturbation imposed on a section of an infinite jet considering periodic boundary conditions at the edge of the computational domain, was followed by Perucho et al. (2004a,b) for 2D slab and cylindrical jets, including the case of sheared flows in Perucho et al. (2005).

Perucho et al. (2010c) summarises the results as follows: 1) cold and slow jets, defined by low relativistic Mach number $\mathcal{M}_j$ and Lorentz factor γ_j values, are unstable and are disrupted after the generation of a shock front crossing the boundary between the jet and the ambient medium due to the development of long wavelength KHI modes; 2) hot and slow jets with intermediate values of $\mathcal{M}_j$ and γ_j are also unstable, but disrupted and mixed in a continuous way by the growth of the mixing layer along the propagation, down to the jet axis; 3) faster jets with high values of $\mathcal{M}_j$ and γ_j develop short-wavelength,

high-order modes that grow in the shear layer and saturate the instability growth without a loss of either their collimation or mixing, and generate a hot shear layer around the jet core; and 4) lighter jets are less stable than denser ones.

To derive numerically a linear growth time of the Kelvin-Helmholtz instability, I chose to use the approach introduced in Hanasz & Sol (1996), describing the jet with a 2D slab geometry. This choice is made as the solutions for both the slab and cylindrical geometries have similar behaviour over a large range of physical parameters, apart from slight numerical differences (Ferrari et al., 1982). In this analogy, symmetric and antisymmetric modes in the slab geometry correspond to pinching and helical modes in the cylinder geometry. Only high order fluting modes do not have counterparts in slab jets.

Hanasz & Sol (1996) consider a core-sheet jet made of three layers, namely the beam, cocoon, and ambient medium, and describes the transition layers at all interfaces in the vortex-sheet approximation. In this model, the beam flow is relativistic, the cocoon is non-relativistic and the ambient medium is at rest. In the following, quantities with subscript b refers to the beam, subscript c to the cocoon and w for the ambient medium. We introduce the quantities $\eta_c \equiv \rho_b/\rho_c$ and $\eta_w \equiv \rho_c/\rho_w$ as the beam-cocoon and cocoon-ambient medium density contrast respectively, and $R \equiv r_c/r_b$ as the radius ratio between the sheet and the core. In the steady state, the flow for each layer l can be described by:

$$\rho = \rho_{0l}, \tag{1.12}$$

$$\vec{v_l} = \begin{bmatrix} v_{0l} \\ 0 \\ 0 \end{bmatrix}, \tag{1.13}$$

$$p_l = p_0, \tag{1.14}$$

with a pressure equilibrium between the different layers. A perturbation to this steady state is assumed to be wavelike in $\exp\left[i(k_x x + k_z z - \omega t)\right]$. This wavelike perturbation of the internal interface generates a sound wave with the same frequency and wavenumber that travel in the cocoon layer. As the maxima of the growth rate coincides with acoustic waves that travel an integer multiple of wavelength on their path back and forth across the cocoon (see figure1.1 for an illustration), I chose to focus on those resonances to derive an estimation for the KHI growth time.

Considering a sound wave traveling between the internal and external interfaces with a wavelength $\lambda_c = 2\pi/\sqrt{k_x^2 + k_z^2}$ and a propagation angle α defined by $\tan\alpha = k_x/k_z$, the distance travelled by the wave between the interfaces is $L = (R-1)/\cos\alpha$. From the full derivation of the dispersion relation found in Hanasz & Sol (1996), we have in the cocoon:

$$k_z = \left(\frac{\omega_0^2}{\eta_c \Gamma} - k_x^2\right)^{1/2}, \tag{1.15}$$

$$\omega_0 = \omega - \sqrt{\eta_c \Gamma} M_c k_x. \tag{1.16}$$

Substituting these expressions into the resonance condition $2L = n\lambda_c$, we obtain the following expression:

$$\left[(R-1) - n\pi\left(\frac{\omega^2}{\eta_c\Gamma} + (M_c - 1)k_x^2 + 2\omega k_x \frac{M_c}{\sqrt{\eta_c\Gamma}}\right)^{1/2}\right]\left(\frac{\omega}{\sqrt{\eta_c\Gamma}} - M_c k_x\right) = 0 \tag{1.17}$$

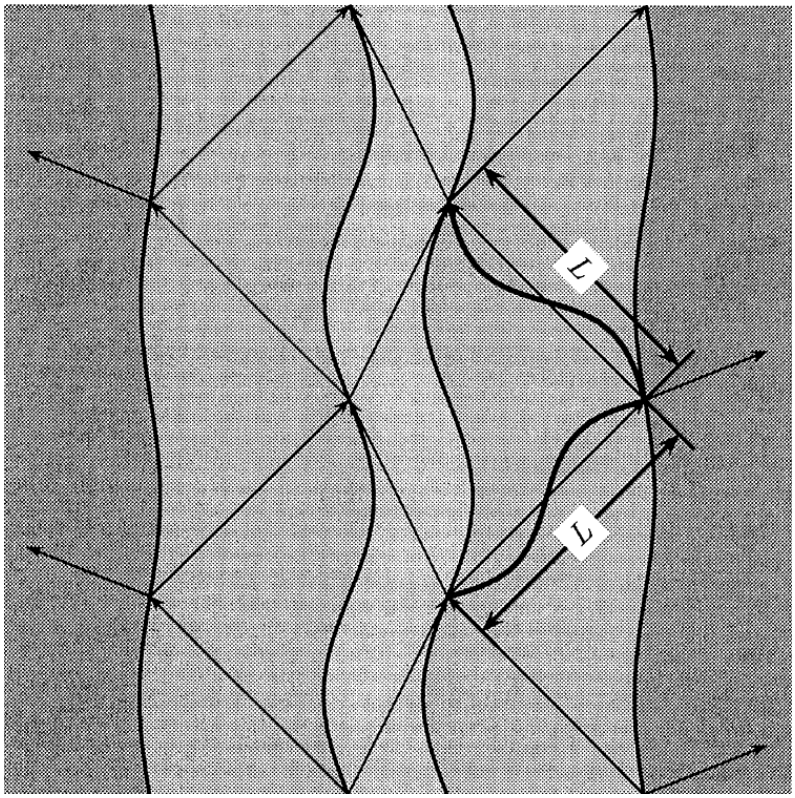

Figure 1.1: From Hanasz & Sol (1996). The sound wave emitted at the internal interface reflects on the external interface, then travels back and interferes with the new emitted wave. The waves drawn in thick line within the cocoon layer represent the integer number of wave periods between the interfaces and not the deformation of the sheet since the acoustic waves are longitudinal.

This equation can then be solved using a Newton-Raphson method and leads to the calculation of the wavenumber k_x maximizing ω with the densities and radii as parameters. Plotting the solutions of equation 1.17 in figure 1.2, we find a roughly quadratic dependance of ω with k_x ($\omega \sim k_x^{2.1}$) for low wavenumbers and a decrease with the square root ($\omega \sim k_x^{-1/2}$) in Cygnus X-1 case at the resonance. This decrease in the growth rate starts at lower k_x when increasing the mode number n. The linear growth time for the KHI is then obtained from $t_{KHI} = \omega^{-1}$ with the maximal growth rate found. Rosen et al. (1999) suggests the growth of KHI is favorized in jets with higher temperature or pressure due to the greater propagation speed (and thus lower crossing time) of the perturbations, which is further confirmed in MHD jets with low magnetisation by Mukherjee et al. (2020).

1.2.3 Rayleigh-Taylor instability

We follow here the derivation from Matsumoto et al. (2017), neglecting the effects of interface curvature to obtain the following dispersion relation at the beam inner-cocoon interface:

$$\omega^2 = -gk\frac{\gamma_b^2\rho_b h_b - \rho_{ic}h_{ic} + \Gamma\gamma_b^2 p_0/c^2}{\gamma_b^2\rho_b h_b + \rho_{ic}h_{ic}} \tag{1.18}$$

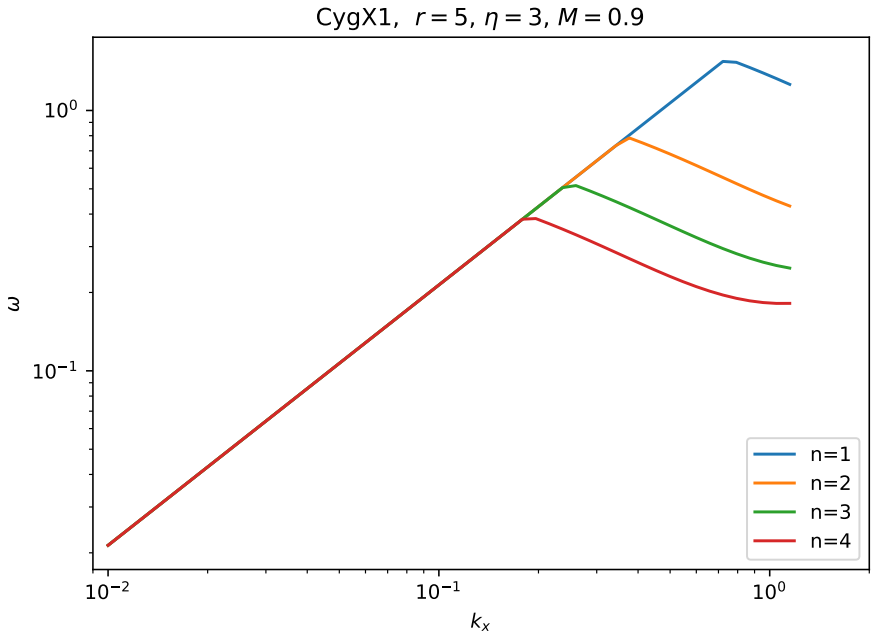

Figure 1.2: Temporal growth rate for the first four modes of the KHI at resonance, using parameters from run CygX1. At low wavenumber, the growth rate grows as $k_x^{\sim 2}$ before decreasing with $k_x^{-1/2}$. This decrease begins at lower k_x when increasing n.

We take $\gamma_{ic} = 1$ (which is verified in all our runs), g is the acceleration of the surface assuming the amplitude of the oscillation is roughly equal to the beam radius and p_0 is the pressure at the interface, we take $p_0 = (p_b + p_{ic})/2$ as a first approximation. We deduce from equations 1.18 that the RTI timescale $t_{RTI} = \mathrm{Im}\,\omega^{-1}$ is proportional to the square root of the wavelength $\lambda = k^{-1}$, meaning the temporal growth of the shorter wavelength modes is faster. However, neglecting the curvature limits the instability to wavelengths smaller than the jet radius and in a numerical grid, only the modes with wavelength of several cell length will matter, restricting the growth of the RTI to few possible wavelengths. This explains the big difference with the growth time of KHI: we find t_{KHI} to be mainly in the range 10^{1-2} s while t_{RTI} is found with values of a few 10^4 to 10^5 s using this derivation.

1.3 Description and classification of relativistic hydrodynamical jets

1.3.1 Jet classification

A relativistic jet is modelled as a hydrodynamical supersonic outflow injected into an ambient medium. The interaction between these two typically results in a richly structured flow field. For any discussion of this complex flow field it is useful to resort to its basic, idealized morphology, characterised by three surfaces separating the flow into four zones. The innermost zone, the jet beam or spine, consists of unprocessed jet material. A combination of discontinuities (including a Mach disk/reverse shock/terminal shock and

potentially shear layers or also reconfinement shocks) separates the jet beam from the inner cocoon, composed of shocked jet material (also called "shear layer", "jet sheath" or simply "cocoon"). A contact discontinuity or working surface marks the transition from inner to outer cocoon (or "cavity"), the latter containing shocked ambient medium. A third discontinuity, a bow or forward shock at the jet head, marks the transition to the ambient medium (good sketches of this structure can be found in other works e.g. Matsumoto & Masada (2019) for a recent example).

Martí et al. (1997) identified five parameters to completely specify a relativistic jet propagating into a homogeneous medium:

1. the density ratio $\eta \equiv \rho_j/\rho_w$,
2. the pressure ratio $K \equiv p_j/p_w$,
3. the beam flow velocity v_j (or its associated Lorentz number γ_j),
4. the beam Mach number M_j,
5. the polytropic index Γ.

Some works also use the relativistic Mach number $\mathcal{M}_j \equiv \gamma_j v_j/\gamma_{s,j} c_{s,j}$, where $c_{s,j}$ is the sound speed in the jet flow and $\gamma_{s,j}$ its associated Lorentz factor. As pointed out by Martí et al. (1997), the propagation efficiency of a relativistic jet is not determined by the density ratio η, but by the ratio η^* between beam and ambient medium inertial mass densities $\gamma^2 \rho h$. This ratio determines the momentum balance at the contact discontinuity in the jet head. Parameters η and η^* are thus linked by the relation:

$$\eta^* = \gamma_b^2 \eta \frac{h_b}{h_w}. \tag{1.19}$$

From those parameters, Martí et al. (1997) classify efficient jets ($\eta^* > 1$) into three cases: dense jets ($\eta > 1$), supersonic jets ($M_j \gg 1$, with high beam flow speeds but non-relativistic temperatures) and hot jets ($h > 1$). Later, another classification based on the width of the mixing layers and the fraction of longitudinal momentum transferred to the ambient medium during the jet evolution was suggested by Perucho et al. (2004b) in the framework of their stability analysis of relativistic jets in regard to the Kelvin-Helmholtz instability:

- Class I: cold, slow jets. They develop wide shear layers and break up as the result of turbulent mixing driven by a shock at the jet-ambient interface.
- Class II: hot and fast jets. Also developing wide shear layers, they transfer more than 50% of their longitudinal momentum to the ambient medium, as a result of the sustained transversal momentum in the jet after saturation of the Kelvin-Helmholtz instability.
- Class III: hot and slow jets. They display intermediary properties between those of class I and II.
- Class IV: warm and fast jets. These jets are the most stable, with limited cocoon expansion and an unperturbed internal flow.

Sufficiently light ($\eta < 0.1$) supersonic jets, as considered in this work, display extended cocoons as the high pressure of the shocked gas drives a backflow towards the source. These jets also display a series of internal oblique shocks in the beam, whose strength and spacing are determined by the Mach number and the gradient in the pressure external to the beam (see e.g. Gómez et al., 1995, 1997, and references therein): the higher these numbers, the stronger and closer to each other these oblique shocks are. Increasing the Mach number also intensifies the cocoon expansion.

The structure of this cocoon is also determined by the adiabatic index Γ: for models with $\Gamma = 5/3$, the cocoon is stable at first but eventually evolves into vortices, producing turbulent structures and generating perturbations at the beam boundary, enriching the beam internal structure. For models with $\Gamma = 4/3$, the first internal conical shock is strong enough for the resulting beam collimation to accelerate the flow. During this acceleration phase, the beam gas is less efficiently redirected to the cocoon downstream, accumulating at jet head. Once this acceleration is over, the continuous flow reestablishes itself, forming small turbulent vortices in the cocoon. The cocoon structure reflects this history, the parts of it formed before and after this beam acceleration phase presenting different morphologies.

In this work, the jet parameters that we derive from the works introduced section 0.2 places our jets in the supersonic case with extended, turbulent cocoons, and a beam with rich internal structure.

1.3.2 Jet propagation

Bodo et al. (1994) observed that during its propagation, a jet will present different structures tightly linked to the evolution of the KHI modes, identifying three phases: in a first *linear phase*, the various modes grow following the linear behaviour, and no shock is present in the beam. The apparition of biconical shocks centered on the beam axis marks the beginning of the *expansion phase*, during which the strength of these shocks grow and the jet radius expands in the post-shock region. Finally, the evolution of the shocks leads to mixing between the jet and the external material, marking the start of the *mixing phase*.

An explanation for the inner structure of non-relativistic jets with adiabatic index $\Gamma = 5/3$ has been suggested by Koessl & Mueller (1988), which still holds for relativistic jets as Rosen et al. (1999) argues the general conclusions for classical jets are valid for relativistic jets with the exception of the velocity field which cannot be scaled up to give the spatial distribution of Lorentz factor, and a few modes of the Kelvin-Helmholtz instability whose growth are affected. Koessl & Mueller (1988) describe the "early" phase (the expansion phase of Bodo et al. 1994) of jet propagation as quasi-periodic due to an intense vortex at the beam cap, driving a strong shock into the beam which is reflected back and forth between beam axis and boundary. This leads to a regular shock structure responsible for the beam collimation even in a substantially overpressured jet (Falle, 1987), as only the velocity component normal to the shock is affected in an oblique shock, being reduced downstream of the shock, while the tangential component is steady. This picture is complicated by the fact that shocks are also the boundary lines of rarefaction waves: plane waves towards the axis and centered waves towards the boundary. The latter are centered on the reflection points of the internal shocks at the boundary, causing a

deflection of velocity away from the axis. The effects of the shock collimation and the centered rarefaction decollimation result in an almost constant beam diameter. This shock structure results in density and pressure having local minima just upstream and local maxima just downstream of the reflection points on the axis, and vice-versa for velocity.

At beam head, the last incident shock interacts with the terminal Mach disk at a triple shock point. The diameter of the Mach disk becomes smaller as the jet propagates, therefore the new reflected shock grows more intense. When the Mach disk degenerates to a regular shock reflection point, a new incident shock and Mach disk are formed very quickly just ahead of the vortex, creating a shock cross-over where the shock wave extending into the cocoon causes the vortex to shed. A new vortex is generated as soon as the old one is shed.

In the later stages of the jet evolution (the jet mixing phase), the instabilities disturb the beam structure, which becomes time-dependant. The initially steady internal shocks begin to propagate downstream in the beam to finally be reflected, causing oscillation in the beam structure. These oscillations are then responsible for periodic variations in the beam head propagation speed: a smaller secondary bow shock is formed when the beam head reaccelerates with a faster propagation than the leading bow shock, interacting with it to form a triple shock point in the bow shock which then appears as a kink propagating away from the axis. The interaction of the third shock extending from this point with the contact discontinuity excites higher KHI modes in the cocoon, creating a feed back loop responsible for the periodic speed variations of the jet head. Koessl & Mueller (1988) also note that this feed back loop seems to be the cause of the decrease in the instability wavelength, whose lower limit was determined by the grid resolution and numerical diffusion.

1.3.3 Steady state structure

After the jet has evolved long enough, a quasi-steady structure takes place. While the transversal jet structure appears naturally from the growth of KHI during the jet evolution, the internal longitudinal structure is governed by shocks whose origin stems from the reaction of the jet to the decreasing pressure profile of the ambient medium.

Laboratory experiments on supersonic hydrodynamical jets showed that steady shocks can be induced by the pressure difference with the surrounding medium, as the jet expands or contracts upon leaving the nozzle in effort to reach pressure equilibrium. Wilson & Falle (1985) shows the presence of shocks depends on the ratio between two length scales l_j/l_a. $l_j \approx 2R_jM_j$ is the length scale over which a jet can react to external pressure changes, corresponding to the distance traveled by the jet fluid in the time it takes a sound wave to cross the jet beam, while l_a is the characteristic length of ambient pressure variation rate. In the case $l_j/l_a \ll 1$, the jet reacts almost instantly to external pressure variations and achieves equilibrium with the ambient medium. They then suggests that the condition for shock production is for l_j/l_a to go through a maximum $\sim O(1)$ and a decrease in the opening angle near that position. This is confirmed by the simulations, and extended to relativistic flows in Wilson (1987).

In the case of an homogeneous ambient medium of constant pressure, the internal structure is governed by the pressure ratio K introduced section 1.3. Martí et al. (2018)

explains that for values $1 < K \lesssim 2$, the adaptation to the ambient medium is mediated by a continuous flow with periodic variations of wavelength $\lambda = l_j$, causing a repeating pattern to form with a repeat length approximatively given by the product $R_j M_j$ downstream of the first recollimation shock (Wilson & Falle, 1985). For $K \gtrsim 2$, the periodic variations saturate into recollimation shock undergoing regular reflection. Finally, as K increases, so does the angle of the incident shock, up to some critical value beyond which the regular reflection of the shock turns into a Mach reflection, characterised by a subsonic flow downstream of it. An illustration of these situations is given figure 1.3.

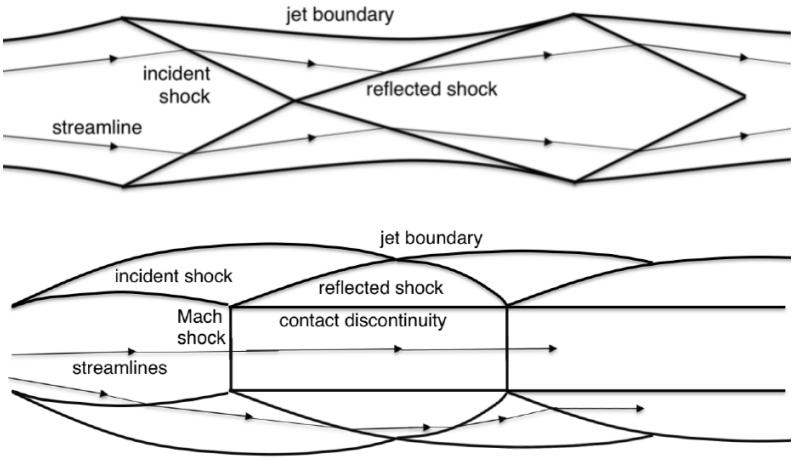

Figure 1.3: From Martí et al. (2018). Internal structure of an overpressured jet propagating through an homogeneous ambient medium for $K \approx 2$ (top) and $K > 2$ (bottom).

In the case of an ambient pressure profile decreasing in $p \propto x^{-\alpha}$, most often used to model the extragalactic environment AGN jets propagate in, Martí et al. (2018) link the scale length l_a and the internal structure of the jet to α: jets expand freely for $\alpha \geq 4$, recollimation shocks able to reach the jet axis form for $\alpha \sim 2$, while between those two values an intermediate regime with an extended shocked layer is formed. For values $\alpha < 2$, the jet suffers such a rapid lateral expansion that the causal communication across the jet is completely lost and global instabilities of any type become totally suppressed.

By letting their simulated jets evolve until they reached a quasi steady state, Perucho et al. (2004b) found that the different jets from their classification (introduced section 1.3) displayed remarkable morphological properties. In class I (cold and slow) jets, the flow pattern is irregular and turbulent and the structure of KH modes are still visible on the background of the highly evolved mean flow pattern. Class II (hot and fast) jets present a regular pattern of "young" vortices visible in the tracer and specific internal energy distributions. They suggest the enhanced transfer of momentum found in the models of this class is probably connected to the presence of these "young" vortices. The flow of class III (hot and slow) jets is well mixed, i.e. tracer, internal energy and Lorentz factor are smoothed along lines parallel to the jet symmetry plane while highly evolved vortices are found, as well as a fossil of KH modes only visible in the pressure waves. Lastly, class IV (warm and fast) jets display no vortices, no chaotic turbulence, very weak mixing, and a very regular structure of KH modes.

1.4 Effects of magnetic field on relativistic jets

Even though MHD effects are out of the scope of this hydrodynamical study, it is worth mentioning the modifications that magnetisation brings to the picture described in section 1.3.

1.4.1 Effects on instabilities growth

Magnetised jets will develop MHD instabilities that may play an important role in the jet dynamics and evolution: the growth of KHI whose role is discussed section in 1.2.2 can be modified by the presence of magnetic field (Bodo et al., 2013, 2019), and current driven instability (CDI) may grow (Nakamura et al., 2007; Mignone et al., 2010; Mizuno et al., 2014; Bromberg & Tchekhovskoy, 2016). These instabilities growth and the way they affect the jet depend on the jet properties such as velocity, magnetisation, and opening angle; and the density profile of the external medium (Porth & Komissarov, 2015; Tchekhovskoy & Bromberg, 2016). In particular, the growth of KHI modes is slower for jets with stronger magnetisation, higher velocities and colder plasma. On the other hand, strongly magnetised and collimated jets are prone to CDI growth. The relative importance of these two main instabilities thus depends on the jet parameters.

Studies of MHD jets have been performed (see e.g. Mignone et al., 2010; English et al., 2016) but did not explore the relative growth of MHD instabilities in a systematic way. A discussion on the onset of MHD instabilities and their impact on jet growth and dynamics for different parameters is given by Mukherjee et al. (2020). In this work, the authors group the type of instabilities into two broad categories: the large scale modes at higher magnetisation, and the small scale modes at lower magnetisation or higher internal pressure.

The large scale modes observed in the first category results from a higher growth rate of CDI with higher magnetisation, which is coherent with the linear analysis of $m = 1$ modes in relativistic MHD jets done in Bodo et al. (2013). Those large scale modes may result in global bending of the jet as well as substantial modifications to the jet and cocoon morphology. But the aforementioned growth rate diminishes with the jet Lorentz factor ($\mathrm{Im}(\omega) \propto \gamma_j^{-4}$), explaining the absence of strong disruptive kink modes in jets with high velocity. Results from Tchekhovskoy & Bromberg (2016) additionally demonstrated that those types of jets remain quite stable even when propagating into steeper density profiles. In the second category with lower magnetisation, the growth of velocity shear driven KHI lead to a higher level of turbulence in the cocoon as well as near the jet axis. These modes are disruptive, resulting in a significant jet deceleration as well as decollimation of the jet axis.

The relative growth of kink and small scale KH instabilities is also determined by jet power: Mukherjee et al. (2020) find the low power jets are susceptible to both modes triggering, with a relative importance depending on the magnetisation. Jets of moderate power are less prone to kink instabilities, but show a strong development of KHI when weakly magnetised. Lastly, and as mentioned previously, powerful jets of high Lorentz factor are the most stable with respect to all instabilities.

1.4.2 Effects on the steady-state structure

An extension to the classification from Martí et al. (1997) is given in Martí et al. (2016), focusing on the internal structure of steady jets depending on the dominant energy: internal energy for hot jets, rest-mass energy for kinetically dominated jets, magnetic energy for Poynting-flux dominated jets; all other injection parameters kept constant. A new effect arising from the jet magnetisation is the development of small azimuthal velocities due to the Lorentz force in all jets, even though they were all injected with purely axial flow velocity.

Martí et al. (2016) also find all in their jet models an equilibration with the external medium through a series of expansions and compressions of the jet flow associated with standing oblique (recollimation) shocks, in a similar fashion to hydrodynamical jets. These oscillations follow definite trends with specific internal energy, magnetosonic Mach number, and magnetisation, depending on the dominant form of energy. In particular, the oscillation wavelength augments (i.e. the angle made by the oblique shocks with respect to the axis diminishes) with the magnetosonic Mach number, again in a similar fashion to the link between this wavelength and the Mach number in hydrodynamical jets described section 1.3.3. For constant magnetosonic Mach number, this wavelength increases with magnetisation but decreases with specific internal energy.

Indeed, the jets dominated by their internal energy present the richest internal structure, with a substantial amount of internal energy converted into kinetic energy and back at the expansions and compressions respectively. Concerning the Poynting flux dominated jets, Martí et al. (2016) suggest, in agreement with the results presented section 1.4.1, that the higher the magnetisation the greater the effect of magnetic pinch modes. They also observed that in such highly magnetised jets, these effects concentrate most of the jet energy in a thin, hot spine centered on the axis. Lastly, the kinetically dominated jets present no internal structure, coherent with the results from Mukherjee et al. (2020).

1.5 Wind effects

The effects of stellar wind on jets were first investigated in Perucho & Bosch-Ramon (2008) with relativistic numerical simulations of 2D slab and cylindrical jets over the scale of one orbital distance, in which the ambient medium is a constant wind perpendicular to the jet injection direction. They found that a strong shock is generated in the wind by the jet head, while strong recollimation shocks could occur in the jet beam due to the initial overpressure compared to the environment. They also suggested that weak jets with kinetic power of 10^{36} erg s^{-1} were disrupted by the strong winds of O-type stars, such as in the case of the Cygnus X-1 system. These results were confirmed with 3D simulations in Perucho et al. (2010b), highlighting the role of asymmetric Kelvin-Helmholtz instabilities in the jet disruption which prevents such jets to propagate over the orbital separation scale. This study suggested that this disruption could happen even for jet powers of several time the previous estimation, setting a lower limit at $\sim 10^{37}$ erg s^{-1} on the kinetic power of the jet in Cygnus X-1. A companion paper (Perucho et al., 2010a) highlighted the formation of the recollimation shock, which they found to propagate very slowly along the jet propagation direction as the pressure in the surrounding cocoon drops with its expansion. This shock is suggested as a candidate region for the production of high-

energy emission.

1.5.1 Jet bending

A larger-scale non-relativistic study was performed in Yoon & Heinz (2015), with a simulation box scale of $\sim 15\ a$, a the orbital distance, with a focus on jet bending due to the wind impact, deriving an analytical formula for the bending angle defined as the angle between the jet trajectory and the jet injection direction.

Considering the jet freely expanding after the initial recollimation shock happening at height x_1, the jet thickness h follows from pressure equilibrium between the jet and the bow shock:

$$h(x) = h_1 \left(\frac{a^2}{a^2 + x^2} \right)^{-1/\Gamma}, \tag{1.20}$$

with h_1 the thickness at the recollimation shock. Estimating the initial opening angle as $\alpha_0 \sim 3/M_j$, we evaluate $h_1 = 2x_1 \sin \alpha_0$. Assuming the longitudinal jet velocity constant and $M_j \gg 1$, the longitudinal jet momentum per unit length is:

$$\Phi_j = \int dA_\perp \rho_j v_j = \frac{L_j}{v_j^2}, \tag{1.21}$$

where L_j is the jet kinetic power and $dA_\perp$ the area perpendicular to the initial jet direction. As the jet propagates, it accumulates transverse momentum from the wind. At a height x, it has accumulated:

$$\begin{aligned}
\Delta\Phi_w &= \frac{1}{v_j} \int_0^x dx' v_{w,\perp}^2(x') \rho_w(x') h(x') \\
&= \frac{1}{v_j} \int_0^x dx' \rho_{w,0} v_w^2 \left(\frac{a^2}{a^2 + x'^2} \right)^2 h_1 \left(\frac{a^2}{a^2 + x'^2} \right)^{-1/\Gamma} \\
&= \frac{h_1 \rho_{w,0} v_w^2}{v_j} \int_0^x dx' \left(\frac{a^2}{a^2 + x'^2} \right)^{2-1/\Gamma} \\
&= \frac{h_1 \dot{M}_w v_w}{4\pi a v_j} \int_0^{x/a} du \left(\frac{1}{1 + u^2} \right)^{2-1/\Gamma}
\end{aligned} \tag{1.22}$$

Then, at the first order approximation, the bending angle is equal to the ratio of transverse to longitudinal momentum:

$$\begin{aligned}
\psi(x) &= \frac{\Delta\Phi_w}{\Phi_j} \\
&= \frac{\dot{M}_w v_w v_j h_1}{4\pi a P_j} \int_0^{x/a} du \left(\frac{1}{1 + u^2} \right)^{2-1/\Gamma},
\end{aligned} \tag{1.23}$$

where the integral is easily evaluated numerically. Its asymptotic limit is also given in terms of elementary gamma functions[1]:

$$\lim_{x \to \infty} \int_0^{x/a} du \left(\frac{1}{1 + u^2} \right)^{2-1/\Gamma} = \frac{\sqrt{\pi}}{2} \frac{\Gamma_E(3/2 - 1/\Gamma)}{\Gamma_E(2 - 1/\Gamma)}. \tag{1.24}$$

[1] written with a subscript E to avoid ambiguity with the adiabatic index Γ

Another slightly different derivation has been made in a following paper (Yoon et al., 2016), but is more appropriate for weaker and strongly bent jets which is not the case of Cygnus X-1 and Cygnus X-3 jets.

1.5.2 Recollimation shock

In the same paper, Yoon et al. (2016) find the condition for the formation of a strong recollimation shock by equating the ram pressures inside and outside the jet, obtaining a quadratic equation in (x/a). This equation has real positive solutions if the kinetic jet power satisfies:

$$L_j \leq L_{cr} \equiv \frac{1}{16}\dot{M}_w v_w v_j. \tag{1.25}$$

In the case of jets tilted by an angle ξ with respect to the perpendicular to the orbital plane, the shock formation criterion is:

$$L_j \leq L_{cr}\left(\frac{1+\cos\xi}{\sin\xi}\right)^2. \tag{1.26}$$

Then, the lower solution x_1 to the aforementioned equation is the shock location, given by:

$$\left(\frac{x_1}{a}\right)^2 = \delta - 1 - \sqrt{\delta^2 - 2\delta}, \quad \delta \equiv \frac{L_{cr}}{2L_j} \leq 2. \tag{1.27}$$

After the shock and up to height x_2, the jet is no longer conical and freely expanding. This height corresponds to the upper solution:

$$\left(\frac{x_2}{a}\right)^2 = \delta - 1 + \sqrt{\delta^2 - 2\delta}. \tag{1.28}$$

Yoon et al. (2016) emphasises that such a shock is likely present in Cygnus X-1 while the situation in Cygnus X-3 is less clear.

1.5.3 Wind clumpiness

In these studies, the wind was considered isotropic or constant, but several papers pointed to the fact that stellar winds are rather clumpy than homogeneous. The effects of wind clumpiness on the jet evolution were explored in Perucho & Bosch-Ramon (2012), concluding that even moderate wind clumping has strong effects on jet disruption, mass loading, bending and likely energy dissipation in the form of emission. A following paper by de la Cita et al. (2017) investigated the gamma ray production of such interactions, concluding that a clump-to-average wind density contrast greater or equal than ten could produce high-energy emissions bright enough to match the observed GeV luminosity in Cygnus X-1 and Cygnus X-3 when a jet is present in those sources.

Bibliography

Allen A., Hughes P., 1984, Monthly Notices of the Royal Astronomical Society, 208, 609
Birkinshaw M., 1984, Monthly Notices of the Royal Astronomical Society, 208, 887

Blandford R., Pringle J., 1976, Monthly Notices of the Royal Astronomical Society, 176, 443
Bodo G., Massaglia S., Ferrari A., Trussoni E., 1994, Astronomy and Astrophysics, 283, 655
Bodo G., Mamatsashvili G., Rossi P., Mignone A., 2013, Monthly Notices of the Royal Astronomical Society, 434, 3030
Bodo G., Mamatsashvili G., Rossi P., Mignone A., 2019, Monthly Notices of the Royal Astronomical Society, 485, 2909
Bromberg O., Tchekhovskoy A., 2016, Monthly Notices of the Royal Astronomical Society, 456, 1739
Choudhury S. R., Lovelace R., 1984, The Astrophysical Journal, 283, 331
Duffell P. C., MacFadyen A. I., 2011, The Astrophysical Journal Supplement Series, 197, 15
English W., Hardcastle M. J., Krause M. G., 2016, Monthly Notices of the Royal Astronomical Society, 461, 2025
Falle S. A. E. G., 1987, in Kundt W., ed., NATO Advanced Study Institute (ASI) Series C Vol. 208, Astrophysical Jets and their Engines. pp 163–170
Ferrari A., Trussoni E., Zaninetti L., 1978, Astronomy and Astrophysics, 64, 43
Ferrari A., Massaglia S., Trussoni E., 1982, Monthly Notices of the Royal Astronomical Society, 198, 1065
Gómez J., Martí J. M., Marscher A., Ibáñez J. M., Marcaide J., 1995, The Astrophysical Journal Letters, 449, L19
Gómez J., Martí J. M., Marscher A., Ibáñez J. M., Alberdi A., 1997, The Astrophysical Journal Letters, 482, L33
Gourgouliatos K. N., Komissarov S. S., 2018, Monthly notices of the Royal Astronomical Society: letters, 475, L125
Hanasz M., 1995, PhD thesis
Hanasz M., 1997, Astronomy & Astrophysics, 327, 813
Hanasz M., Sol H., 1996, Astronomy and Astrophysics, 315, 355
Hanasz M., Sol H., 1998, Astronomy and Astrophysics, 339, 629
Hardee P., 1979, The Astrophysical Journal, 234, 47
Hardee P., 1984, The Astrophysical Journal, 287, 523
Hardee P., 1986, The Astrophysical Journal, 303, 111
Hardee P. E., 1987, The Astrophysical Journal, 318, 78
Hardee P. E., Rosen A., Hughes P. A., Duncan G. C., 1998, The Astrophysical Journal, 500, 599
Hardee P. E., Hughes P. A., Rosen A., Gomez E. A., 2001, The Astrophysical Journal, 555, 744
Koessl D., Mueller E., 1988, Astronomy and Astrophysics, 206, 204
Landau L., Lifshitz E., 1959, Fluid Mechanics, by L.D. Landau and E.M. Lifshitz. Course of Theoretical Physics, Pergamon Press, https://books.google.fr/books?id=CVbntgAACAAJ
Martí J. M., Müller E., Font J., Ibáñez J. M. Z., Marquina A., 1997, The Astrophysical Journal, 479, 151
Martí J. M., Perucho M., Gómez J. L., 2016, APJ, 831, 163

Martí J. M., Perucho M., Gómez J. L., Fuentes A., 2018, International Journal of Modern Physics D, 27, 1844011
Matsumoto J., Masada Y., 2013, The Astrophysical Journal Letters, 772, L1
Matsumoto J., Masada Y., 2019, Monthly Notices of the Royal Astronomical Society, 490, 4271
Matsumoto J., Aloy M. A., Perucho M., 2017, Monthly Notices of the Royal Astronomical Society, 472, 1421
Meliani Z., Keppens R., 2007, Astronomy & Astrophysics, 475, 785
Meliani Z., Keppens R., 2009, The Astrophysical Journal, 705, 1594
Mignone A., Rossi P., Bodo G., Ferrari A., Massaglia S., 2010, Monthly Notices of the Royal Astronomical Society, 402, 7
Mihalas D., Mihalas B. W., 1984, Foundations of radiation hydrodynamics. Courier Corporation
Millas D., Keppens R., Meliani Z., 2017, Monthly Notices of the Royal Astronomical Society, 470, 592
Mizuno Y., Hardee P., Nishikawa K.-I., 2007, The Astrophysical Journal, 662, 835
Mizuno Y., Hardee P. E., Nishikawa K.-I., 2014, The Astrophysical Journal, 784, 167
Mizuta A., Yamada S., Takabe H., 2004, The Astrophysical Journal, 606, 804
Mukherjee D., Bodo G., Mignone A., Rossi P., Vaidya B., 2020, MNRAS, 499, 681
Nakamura M., Li H., Li S., 2007, The Astrophysical Journal, 656, 721
Nishihara K., Wouchuk J., Matsuoka C., Ishizaki R., Zhakhovsky V., 2010, Philosophical Transactions of the Royal Society A: Mathematical, Physical and Engineering Sciences, 368, 1769
Norman M. L., Winkler K.-H., Smarr L., Smith M., 1982, Astronomy and Astrophysics, 113, 285
Payne D., Cohn H., 1985, The Astrophysical Journal, 291, 655
Perucho M., Bosch-Ramon V., 2008, Astronomy & Astrophysics, 482, 917
Perucho M., Bosch-Ramon V., 2012, Astronomy & Astrophysics, 539, A57
Perucho M., Hanasz M., Marti J.-M., Sol H., 2004a, Astronomy & Astrophysics, 427, 415
Perucho M., Marti J.-M., Hanasz M., 2004b, Astronomy & Astrophysics, 427, 431
Perucho M., Marti J.-M., Hanasz M., 2005, Astronomy & Astrophysics, 443, 863
Perucho M., Bosch-Ramon V., Khangulyan D., 2010a, International Journal of Modern Physics D, 19, 791
Perucho M., Bosch-Ramon V., Khangulyan D., 2010b, Astronomy & Astrophysics, 512, L4
Perucho M., Marti J.-M., Cela J., Hanasz M., de La Cruz R., Rubio F., 2010c, Astronomy & Astrophysics, 519, A41
Porth O., Komissarov S. S., 2015, Monthly Notices of the Royal Astronomical Society, 452, 1089
Ray T. P., 1982, Monthly Notices of the Royal Astronomical Society, 198, 617
Rosen A., Hughes P. A., Duncan G. C., Hardee P. E., 1999, The Astrophysical Journal, 516, 729
Rossi P., Mignone A., Bodo G., Massaglia S., Ferrari A., 2008, Astronomy & Astrophysics, 488, 795
Scheck L., Aloy M., Martí J., Gómez J., Müller E., 2002, Monthly Notices of the Royal

Astronomical Society, 331, 615
Tchekhovskoy A., Bromberg O., 2016, Monthly Notices of the Royal Astronomical Society: Letters, 461, L46
Toma K., Komissarov S. S., Porth O., 2017, Monthly Notices of the Royal Astronomical Society, 472, 1253
Turland B., Scheuer P., 1976, Monthly Notices of the Royal Astronomical Society, 176, 421
Wilson M., 1987, Monthly Notices of the Royal Astronomical Society, 226, 447
Wilson M., Falle S., 1985, Monthly Notices of the Royal Astronomical Society, 216, 971
Yoon D., Heinz S., 2015, The Astrophysical Journal, 801, 55
Yoon D., Zdziarski A. A., Heinz S., 2016, Monthly Notices of the Royal Astronomical Society, 456, 3638
de la Cita V. M., del Palacio S., Bosch-Ramon V., Paredes-Fortuny X., Romero G. E., Khangulyan D., 2017, A&A, 604, A39

Chapter 2

Radiative processes in thermal, optically thin, relativistic plasmas

Following Bodo & Tavecchio (2018), radiative losses can be added in SRHD equations by introducing a source term in equation 1.7:

$$\partial_t \mathcal{U} + \partial_i \mathcal{F}^i = \Psi. \tag{2.1}$$

In this work, the source term Ψ reflects the radiative losses of thermal, optically thin, relativistic plasmas. The non-thermal particles are not considered in this work. We present this source term in section 2.1 from the derivation of the radiated power through free-free (or Bremsstrahlung) emission, synchrotron emission, and inverse Compton (IC) scattering, to which a supplementary term from line and recombination cooling is added. The emission coefficient for the same processes are presented section 2.2.

2.1 Energy losses

Given the presence of an external photon field as seeds for IC scattering, the emission pattern is anisotropic in the comoving frame of the emitting region, making the jet recoil. But according to Ghisellini & Tavecchio (2010), this recoil can be neglected in the case of a ion-electron plasma as the majority of the jet momentum is transported by the ions. Both free-free emission and line cooling are dominated by the Coulombian interactions between electrons and ions which are isotropic in the fluid rest frame, this logic also applies to synchrotron losses as the pitch angle (between electron speed and magnetic field direction) distribution is assumed isotropic. In the lab frame, the relativistic beaming leads to anisotropy resulting in momentum loss for the electrons, but we neglect these losses following the same argument as for IC scattering. We can then model the effect of the various radiative losses as a single energy-loss term in the plasma rest frame:

$$\Psi = \begin{bmatrix} 0 \\ \vec{0} \\ P_{rad} \end{bmatrix},$$

where $P_{rad} = P_{IC} + P_{syn} + P_{ff} + P_{line}$ is the power loss density due to inverse Compton scattering, synchrotron emission, free-free emission, and line and recombination cooling.

A thermal plasma distribution of the electrons can be written in a general way using a Maxwell-Jüttner distribution of the electrons in the plasma rest frame from Jüttner (1911), as in Wardzinski & Zdziarski (2000):

$$n_e(\gamma) = \frac{n_e}{\Theta} \frac{\gamma_e(\gamma_e^2 - 1)^{1/2}}{K_2(\Theta^{-1})} \exp(-\gamma_e/\Theta), \tag{2.2}$$

where K_2 is the modified Bessel function of the 2nd kind of order 2 and $\Theta = k_B T/m_e c^2$ is the normalized temperature. In this work, I assumed the proton and electron temperature to be equal everywhere in the flow. I discuss this section 5.2.5. This formulation is adapted to our model as temperatures can exceed 10^{10} K behind shocks. The proton distribution can be at first assumed to be non-relativistic at the temperatures reached by our simulations as $\Theta_p = k_B T/m_p c^2 \ll 1$ for $T < 10^{12}$ K, where the Maxwell-Jüttner and Boltzmann distributions coincide. An improved model should include relativistic treatment of protons and $e^{\pm}$ pair production since some shock zones may approach temperatures where either protons start to become relativistic or where pair creation start to be effective.

The following expressions are derived in the plasma rest frame but the calculated power loss density is invariant with frame as the volume dilatation is compensated by the time dilatation of the boost. The numerical approximation of the Bessel K function used in A-MaZe is detailed section 3.1.3.

2.1.1 Free-free

Free-free radiation is emitted as an electron is accelerated by the Coulomb field of an ion. The expression of the power loss density due to free-free mechanism of electrons in a Hydrogen - Helium plasma, including relativistic corrections, can be found in Rybicki & Lightman (1979):

$$P_{ff} = 1.4 \cdot 10^{-27} T^{1/2} n_e \left(n_H \bar{g}_H + Z_{He}^2 n_{He} \bar{g}_{He} \right) (1 + 4.4 \cdot 10^{-10} T). \tag{2.3}$$

This expression shows a dependence with ρ^2 and $T^{1/2}$ at classical electron temperatures, which becomes $T^{3/2}$ at high temperatures due to relativistic corrections. Rybicki & Lightman (1979) suggested $\bar{g}_H = \bar{g}_{He} = 1.2$ as good numerical approximation for the frequency-averaged Gaunt factor at all temperature ranges, which is the value used for Cygnus X-1 runs. This approximation is good up to $T \sim 10^9$ K but a better approximation is needed as the temperature in the jet can get relativistic. A better evaluation of this term was given in van Hoof et al. (2015) who provided the values for $\bar{g}_H$ and $\bar{g}_{He}$ as functions of a parameter $\propto T^{-1}$. An illustration of the coefficients is given in figure 2.1. These functions have been implemented in Cygnus X-3 runs.

2.1.2 Synchrotron

Ghisellini (2013) derives the synchrotron power emitted by a single electron of Lorentz factor $\gamma_e = (1 - \beta_e^2)^{-1/2}$ and pitch angle θ (the angle between its velocity and magnetic field lines) in the flow frame:

$$P_e(\gamma_e, \theta) = 2\sigma_T c \gamma_e^2 \beta_e^2 \sin\theta \; U_B \; , \tag{2.4}$$

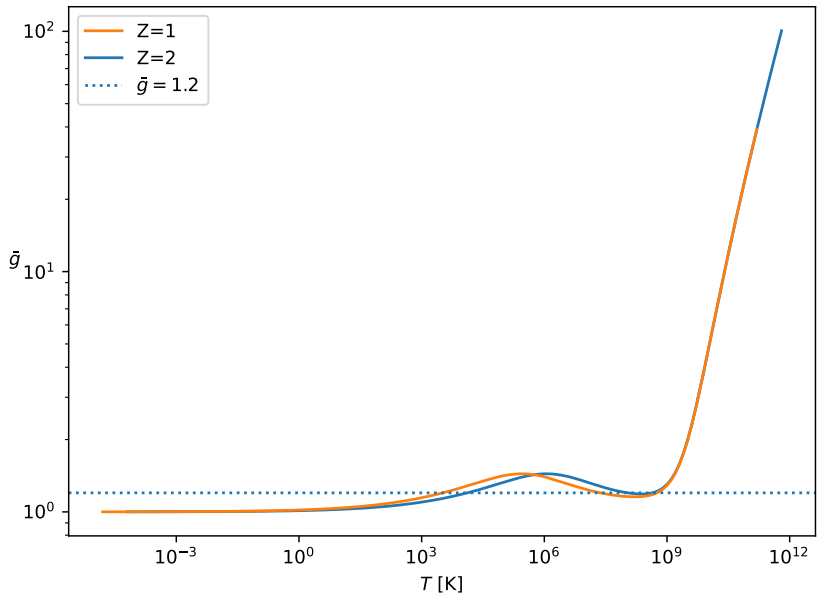

Figure 2.1: Gaunts factor for Hydrogen and Helium across the equivalent tabulated range of temperature covered in van Hoof et al. (2015) and used in our Cygnus X-3 runs. Above 10^9 K, $\bar{g} \propto T^{\sim 3/4}$. The dotted line shows the mean value $\bar{g} = 1.2$ used for Cygnus X-1 runs.

with σ_T the Thomson scattering cross-section and $U_B = B^2/8\pi$ the magnetic field energy density. This power can be averaged over the pitch angle θ as the electron distribution is here assumed to be isotropic:

$$P_e(\gamma_e) = \frac{4}{3}\sigma_T c \gamma_e^2 \beta_e^2 U_B. \tag{2.5}$$

The power loss density is derived by integrating over the electron distribution:

$$\begin{aligned} P_{syn} &= \int P_e(\gamma) n_e(\gamma) d\gamma \\ &= \frac{4}{3}\sigma_T c U_B \frac{n_e}{\Theta K_2(\Theta^{-1})} \int_1^\infty \gamma(\gamma^2-1)^{3/2} e^{-\gamma/\Theta} d\gamma \\ &= 4\sigma_T c n_e \Theta \frac{K_3(\Theta^{-1})}{K_2(\Theta^{-1})} U_B, \end{aligned} \tag{2.6}$$

with K_3 the modified Bessel function of the second kind of order 3. In our simulations, the magnetic energy density is the sum of contributions from the jet and the star, weighted by the tracer J: $U_B = J \times U_{B,j} + (1-J) \times U_{B,\star}$.

These two contributions are modelled differently in the Cygnus X-1 and Cygnus X-3 runs. In Cygnus X-1 case, both the jet and stellar wind magnetic field contribution were taken constant, equal to parameter B_j and $B_\star$ respectively. This choice was made as a first attempt to model losses, at the risk of overestimating synchrotron losses in the long run. Seeing no impact of radiative losses until long simulation times in Cygnus X-1 runs, we chose to launch runs based on Cygnus X-3 and updated our assumptions on the magnetic field. Since many authors such as Perucho (2019) suggested that the jet

magnetic field structure is presumably toroidal, we chose a linear decrease with distance for the jet inner field $B_j = B_{0,j} x_0/x$ to reflect this assumption. The stellar magnetic field was assumed to be a dipole aligned with the normal to the orbital plane, decreasing as r^{-3} with r the distance to the star center. This assumption does not take effects such as increased magnetic field downstream of shocks in consideration and may cause us to underestimate the synchrotron losses in the beam and inner cocoon. A better treatment of synchrotron losses would require magnetohydrodynamical simulations, which are out of the scope of this study.

2.1.3 Inverse Compton scattering

Following Ghisellini (2013), the radiated power per electron in the flow frame is:

$$P_{ph}(\gamma_e, \psi) = \sigma_T c \gamma_e^2 (1 - \beta_e \cos\psi)^2 U_{ph}, \tag{2.7}$$

with ψ the incident photon angle and U_{ph} the radiative energy density in the flow frame. In that frame, the electron distribution is assumed to be isotropic, therefore $(1-\beta_e \cos\psi)^2$ can be averaged over the solid angle, obtaining $1+\beta_e^2/3$. The power loss of a single electron is then:

$$\begin{aligned} P_e(\gamma_e) &= \langle P_{ph}(\gamma_e, \psi) \rangle - \sigma_T c U_{ph} \\ &= \frac{4}{3} \sigma_T c \gamma_e^2 \beta_e^2 U_{ph}. \end{aligned} \tag{2.8}$$

The power loss density in the fluid frame is obtained by integrating over the electron distribution, yielding:

$$P_{IC} = 4 \sigma_T c n_e \Theta \frac{K_3(\Theta^{-1})}{K_2(\Theta^{-1})} U_{ph} \tag{2.9}$$

Considering the star as the sole source of seed photons for inverse Compton scattering, we derive the radiative energy density in the rest frame of the flow moving with a speed $v_j = \beta_j c$. Defining θ as the angle between the photon direction and the flow direction in the star rest frame, the radiative energy density is:

$$U_{ph} = \gamma_j (1 - \beta_j \cos\theta) \frac{\sigma {T_\star}^4}{\pi} \left(\frac{R_\star}{r} \right)^2, \tag{2.10}$$

where r is the distance to the star center in the star rest frame. One may note that synchrotron and inverse Compton cooling follow the same law, their ratio is equal to the ratio between magnetic and stellar photons energy density, respectively U_B and U_{ph}.

One also need to note that this expression is in the Thomson regime. Since we consider a thermal distribution of electrons, the vast majority of their population are at energies where this regime is valid. We verify this assumption easily: the Thomson regime applies as long as the incoming photon energy in the electron rest frame is less than $m_e c^2$, meaning that the scattering of an incoming photon of frequency ν in the flow frame needs to be considered in the Klein-Nishina regime if the electron Lorentz factor γ_e verifies $\gamma_e < m_e c^2 / h\nu$. Taking a normalised temperature $\Theta = 100$ ($T \sim 6 \cdot 10^{11}$ K), the maxima of the Maxwell-Jüttner distribution is at $\log\gamma \sim 2.3$. This translates in the Thomson regime being valid as long as the incoming photon is under $\nu \sim 10^{17}$ Hz. Our source for seed

photons being the companion star, the majority of the incoming photons are at frequency $\nu_0 \sim 10^{15}$ for a star temperature in the 10^4 K range. Thus we consider approximating all scatterings to be in the Thomson regime, and therefore our expression for the IC losses, to be valid.

2.1.4 Line and recombination cooling

This term accounts for collisional excitation of resonance lines and dielectronic recombination, where an ion captures an electron into a high-energy level and then decays to the ground state. In this work we assume solar photospheric abundances and the thermodynamical equilibrium of the plasma (Saha equilibrium) even though, in reality, the recombination may be delayed and not correspond to the actual temperature of the plasma. This term follows the law:

$$P_{line} = \sum_i n_e n_{ion,i} 10^{\Lambda_i(T)}, \tag{2.11}$$

with i the different ion species. For easier calculations, the various ions are taken into account in a single parameter $\Lambda(T)$ from Cook et al. (1989) such that one can take $P_{line} = n_e^2 10^{\Lambda(T)}$. This parametrisation was then extended in temperature range and implemented numerically in Walder & Folini (1996) and subsequent works. In this work we chose an upper temperature of $10^{7.7}$ K for this process, which corresponds to the recombination of fully-ionised iron and the Fe-α line. This very efficient process is only effective in the coolest and most external parts of the cocoon.

2.1.5 Scalings and cooling time

Scaling laws of the radiative losses term

The scalings of the various radiative losses with density, temperature, and distance to the star are consigned in table 2.1. Free-free and line recombination losses both present a quadratic dependency with density, while synchrotron and inverse Compton losses only scale linearly with it. As line cooling only happens when the plasma temperature falls below $10^{7.7}$ K, this implies that free-free can be expected to be the main loss mechanism where the density is high.

The second main parameter for losses intensity is temperature. For free-free losses, the dependency of the Gaunt factors with T modifies the high temperature scaling from $T^{3/2}$ in Cygnus X-1 runs to T^2 in Cygnus X-3 runs. For the synchrotron and inverse Compton losses, the term $K_3(\Theta^{-1})/K_2(\Theta^{-1})$ is constant at low temperatures and proportional to T at relativistic temperatures, explaining the evolution of the scaling with temperature from a linear to a square power-law for both of these processes. Lastly, the line and recombination losses have a non power-law dependency in T. These scalings with temperature are displayed figure 2.2, with the other parameters taken in a part of the outer cocoon still within the binary scale. This allows for a clear showcasing of the losses evolution with temperature, but are not representative of the relative dominance of the various processes over a simulated jet.

At the highest temperatures and if the magnetic or radiative energy density is high enough, the cooling is dominated by respectively synchrotron or inverse Compton processes. Due to the scaling of those energy densities with the distance travelled by the

setup	Cygnus X-1			Cygnus X-3		
variable	ρ	T	r	ρ	T	r
P_{ff}	2	1/2→3/2	0	2	1/2→2	0
P_{syn}	1	1→2	0	1	1→2	-6
P_{ic}	1	1→2	-2	1	1→2	-2
P_{line}	2	/	0	2	/	0

Table 2.1: Power-law exponent of rest mass density, temperature, and distance to the star center in the expression of the different power loss density terms used in code. The exponent dependence with temperature changes while being in the non-relativistic or relativistic regime. The slash indicates a non power-law scaling.

jet, the instances where those processes dominate are expected to be close to the orbital plane.

Cooling time

The cooling time in the observer's frame of a fluid particle with rest frame temperature T and Lorentz factor γ is defined as $t_{cool} = \gamma T/\dot{T}$, where the dot marks the derivation with respect to proper time of the fluid. For a perfect gas, $T = p/\mathcal{R}\rho$ with $\mathcal{R}$ the gas constant divided by the molar mass of the fluid. Therefore:

$$t_{cool} = \gamma \frac{p}{\dot{p} + p\frac{\dot{\rho}}{\rho}} = \gamma \left(\frac{\dot{p}}{p} + \frac{\dot{\rho}}{\rho} \right)^{-1}, \tag{2.12}$$

with all thermodynamic quantities measured in the flow's comoving frame. Two extreme cases can be considered: the isobaric case ($\dot{p} = 0$) where $t_{c,p} = \gamma\rho/\dot{\rho}$ and the isochoric case ($\dot{\rho} = 0$) where $t_{c,\rho} = \gamma p/\dot{p}$.

From the definitions given in section 1.1.1, the variation of the conservative relativistic energy density τ is:

$$\dot{\tau} = 2\gamma(\rho c^2 + \Gamma_1 p)\dot{\gamma} + (\gamma^2\Gamma_1 - 1)\dot{p} + \gamma^2 c^2 \dot{\rho}. \tag{2.13}$$

Then, using $\dfrac{d\tau}{dt} = \gamma^{-1}\dot{\tau} = P_{rad}$ and considering $\dot{\gamma} \ll \dot{p}, \dot{\rho}$ as an approximation in the weakly relativistic case ($\gamma \approx \text{cste} = 1$), these timescales can be approximated as:

$$t_{c,p} = \frac{\gamma^2 \rho c^2}{P_{rad}}, \tag{2.14}$$

$$t_{c,\rho} = \frac{(\gamma^2\Gamma_1 - 1)p}{P_{rad}}. \tag{2.15}$$

The former can be linked to the rest-mass contribution to the flow enthalpy while the latter to the internal energy contribution. Assuming $\gamma^2 = 1$ to approximate those cooling times, $t_{c,p} \propto 10^{21}\rho/P_{rad}$ and $t_{c,\rho} \propto 1.5p/P_{rad}$.

2.2 Volume emission

We now present the derivation of the emission coefficient, relative to the emitted power per frequency, for the radiative processes considered in this study. This quantity is obtained

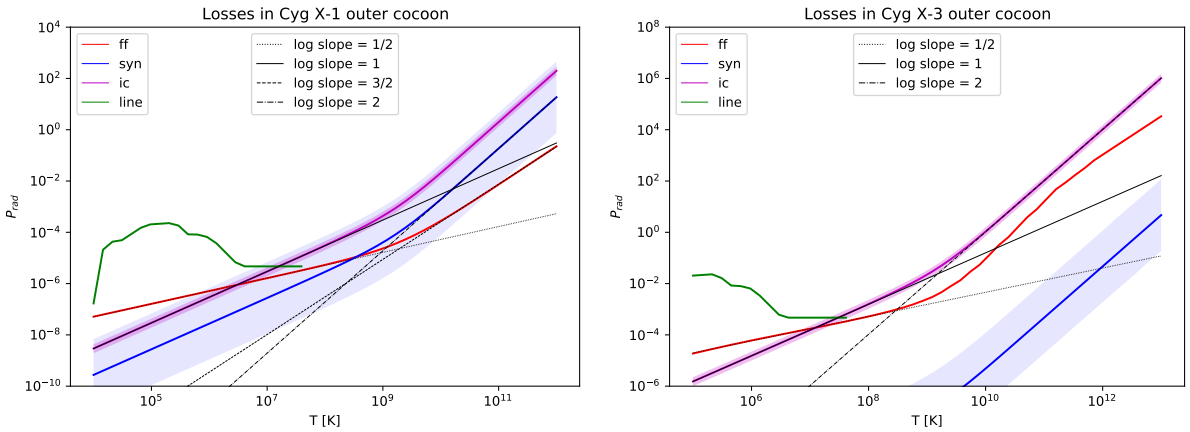

Figure 2.2: Evolution of the losses term with rest frame temperature in Cygnus X-1 (left) and Cygnus X-3 (right). The thin black lines shows the various temperature scalings detailed table 2.1. Line recombination losses ("line", green) are not drawn for $T > 10^{7.7}$ as they are disabled above this temperature. Coloured shading shows synchrotron losses ("syn", blue) when stellar magnetic field $B_\star$ is either multiplied or divided by 5, and the shading around inverse Compton losses ("ic", purple) illustrates a $\pm 10\%$ uncertainty on $T_\star$. The values for the physical quantities have been chosen in the downwind outer cocoon in fiducial runs.
For Cygnus X-1: $\rho = 10^{-15}$ g cm^{-3}, $B_\star = 10$ G, $T_\star = 3 \cdot 10^4$ K, $(x, y, z) = (1.5 \cdot 10^{12}, 4.05 \cdot 10^{13}, 4 \cdot 10^{13})$ cm, $(v_x, v_y, v_z) = (10^8, 10^8, 10^8)$ cm s^{-1}.
For Cygnus X-3: $\rho = 10^{-14}$ g cm^{-3}, $B_\star = 100$ G, $T_\star = 8 \cdot 10^4$ K, $(x, y, z) = (1.5 \cdot 10^{12}, 3.05 \cdot 10^{13}, 3 \cdot 10^{13})$ cm, $(v_x, v_y, v_z) = (10^8, 5 \cdot 10^8, -10^3)$ cm s^{-1}.

by integrating the total emission per unit time per unit volume per unit frequency range $P_\nu(\gamma)$ of an electron due to a given radiative process with the Maxwell-Jüttner distribution (Jüttner, 1911), in a similar fashion to the preceding chapter where we integrated the total emission per unit time per unit volume, while retaining the same hypotheses. All the following derivations are done in the plasma comoving frame.

2.2.1 Free-free

The derivation of the total emission per unit time per unit volume per unit frequency range of the free-free mechanism is given equation (5.11) from Rybicki & Lightman (1979) for a plasma with electron density n_e and ion density n_i:

$$P_\nu^{ff} = \frac{16\pi e^6}{3\sqrt{3}c^3 m_e^2 v} n_e Z^2 n_i g_{ff}(v, \nu), \tag{2.16}$$

where v is the electron velocity and g_{ff} the Gaunt factor introduced section 2.1.1. The emission coefficient is then obtained by integrating P_ν^{ff} over the probability density of electrons following the Maxwell-Jüttner distribution $f(\gamma) = \gamma(\gamma^2 - 1)^{1/2} e^{-\gamma/\Theta} / \Theta K_2(1/\Theta)$. This integral cannot be performed for $\gamma = 1 \ldots \infty$ because the kinetic energy of the electron $(\gamma - 1)m_e c^2$ needs to be greater than the energy of the photon created $h\nu$. This cut-off in the lower limit of the integration over electron Lorentz factor is called a *photon*

discreteness effect. Thus we perform the integral:

$$\begin{aligned} j_\nu^{ff} &= \frac{\int_{\gamma_{min}}^{\infty} P_\nu^{ff}(\gamma) f(\gamma) d\gamma}{\int_1^{\infty} f(\gamma) d\gamma} \\ &= \frac{\int_{\gamma_{min}}^{\infty} P_\nu^{ff} \gamma(\gamma^2-1)^{1/2} e^{-\gamma/\Theta} d\gamma}{\int_1^{\infty} \gamma(\gamma^2-1)^{1/2} e^{-\gamma/\Theta} d\gamma} \\ &= \frac{16\pi e^6}{3\sqrt{3} m_e^2 c^4} \frac{n_e Z^2 n_i \bar{g}_{ff}(T)}{\Theta K_2(1/\Theta)} \int_{\gamma_{min}}^{\infty} \gamma^2 e^{-\gamma/\Theta} d\gamma \end{aligned} \tag{2.17}$$

where $\gamma_{min} = 1 + (h\nu/m_e c^2)$, and the Gaunt factor has been replaced by its frequency-averaged value. The identities $\gamma\beta = (\gamma^2-1)^{1/2}$ and $\int_1^{\infty} \gamma(\gamma^2-1)^{1/2} e^{-\gamma/\Theta} d\gamma = \Theta K_2(1/\Theta)$ were used between the last two lines. Performing the last part of the integral yields:

$$\begin{aligned} \int_{\gamma_{min}}^{\infty} \gamma^2 e^{-\gamma/\Theta} d\gamma &= \Theta^3 \left[\frac{1}{\Theta}(1 + \frac{h\nu}{m_e c^2}) \left(\frac{1}{\Theta}(1 + \frac{h\nu}{m_e c^2}) + 2 \right) + 2 \right] e^{-\frac{1}{\Theta}(1 + h\nu/mc^2)} \\ &\approx (\Theta + 2\Theta^2 + 2\Theta^3) e^{-1/\Theta} e^{-h\nu/\Theta mc^2}. \end{aligned} \tag{2.18}$$

The last line is obtained under the assumption $h\nu/mc^2 \ll 1$, which is valid up to γ-ray frequencies, yielding the final formula:

$$j_\nu^{ff} = \frac{16\pi e^6}{3\sqrt{3} m_e^2 c^4} n_e Z^2 n_i \bar{g}_{ff}(T) \frac{(1 + 2\Theta + 2\Theta^2) e^{-1/\Theta}}{K_2(1/\Theta)} e^{-h\nu/kT}. \tag{2.19}$$

We verify the validity of our expression by taking the nonrelativistic limit $kT \ll m_e c^2 \iff \Theta \ll 1$: using the asymptotic expansion of Bessel K functions for large arguments $K_2(1/\Theta) \sim \sqrt{\pi/2}\Theta^{-1/2}$, found equation (9.7.2) in Abramowitz & Stegun (1964), we obtain:

$$j_\nu^{ff}(T) \sim \frac{32\pi e^6}{3 m_e c^3} \left(\frac{2\pi}{3km} \right)^{1/2} T^{-1/2} n_e Z^2 n_i \bar{g}_{ff}(T) e^{-\frac{h\nu}{kT}} \tag{2.20}$$

which is the formula for thermal non-relativistic free-free emission given equation (5.14a) from Rybicki & Lightman (1979).

2.2.2 Synchrotron

The synchrotron emission coefficient of a thermal relativistic plasma in its comoving frame was derived by Wardzinski & Zdziarski (2000):

$$j_\nu^{syn} = \frac{\pi e^2}{2c} (\nu\nu_c)^{1/2} \chi(\gamma_0) n_e f(\gamma_0) \left(1 + 2\frac{\cot^2\vartheta}{\gamma_0^2} \right) [1 - (1 - \gamma_0^{-2}) \cos^2\vartheta]^{1/4} \mathcal{Z}(\vartheta, \gamma_0). \tag{2.21}$$

ϑ is the angle between the magnetic field direction and the direction toward the observer and $\nu_c = eB/2\pi m_e c$ is the cyclotron frequency.

The functions introduced are defined as:

$$\mathcal{Z}(\vartheta,\gamma)=\left\{\frac{t\exp\left[(1+t^2)^{-1/2}\right]}{1+(1+t^2)^{1/2}}\right\}^{2n},\quad t\equiv(\gamma^2-1)^{1/2}\sin\vartheta,\quad n\equiv\frac{\nu(1+t^2)}{\nu_c\gamma} \tag{2.22}$$

$$\chi(\gamma)=\begin{cases}\left[\frac{2\Theta(\gamma^2-1)}{\gamma(3\gamma^2-1)}\right]^{1/2}, & \Theta\lesssim 0.08\\ \left(\frac{2\Theta}{3\gamma}\right)^{1/2}, & \Theta\gtrsim 0.08\end{cases} \tag{2.23}$$

$$\gamma_0=\begin{cases}\left[1+\left(\frac{2\nu\Theta}{\nu_c}\right)\left(1+\frac{9\nu\Theta\sin^2\vartheta}{2\nu_c}\right)^{-1/3}\right]^{1/2}, & \Theta\lesssim 0.08\\ \left[1+\left(\frac{4\nu\Theta}{3\nu_c\sin\vartheta}\right)^{2/3}\right]^{1/2}, & \Theta\gtrsim 0.08\end{cases} \tag{2.24}$$

Note that approximations 2.23 and 2.24 have a small discontinuity at $\Theta\sim 0.08$ ($T\sim 4.7\cdot 10^8$ K). The relativistic transformation of the magnetic field from the star frame to jet flow frame must be taken in account before determining the angle ϑ.

2.2.3 Inverse Compton

In this subsection, the quantities in the comoving frame are denoted by a prime for clarity. The observed νF_ν spectrum resulting from Compton scattering of stellar radiation for a uniform emitting region filled with an isotropic comoving distribution of electrons is given equation (3) of Dermer & Böttcher (2006):

$$f_\epsilon^{C\star}=\frac{3c\sigma_T u_\star^0\delta_D^2\epsilon^2}{32\pi d_L^2}\int_{\epsilon/\delta_D}^{\infty}d\gamma\frac{N_e'(\gamma)}{\gamma^2}a^2\left[g^{-2}\left(y+\frac{1}{y}\right)I_1-\frac{2\epsilon}{\delta_D\gamma ybg}I_2+\left(\frac{\epsilon}{\delta_D\gamma yb}\right)^2 I_3\right], \tag{2.25}$$

where $y=1-(\epsilon/\delta_D\gamma)$,

$$\delta_D=[\gamma_j(1-\beta_j\mu)]^{-1} \tag{2.26}$$

is the Doppler factor with $\mu=\cos\theta$ where θ is the angle between the velocity of the emitting zone β_j and the observers direction. $\epsilon=h\nu/m_ec^2$ is the dimensionless observed radiation, $N_e'(\gamma)=V_b'n_e'(\gamma)$ is the differential number of electrons with Lorentz factor γ in emitting volume V_b', and d_L the luminosity distance to the source. $u_\star^0=15L_\star/(4\pi^5c\Theta_\star^4r^2)$ is the photon energy density from the star black-body radiation ($L_\star$ and $\Theta_\star$ are the luminosity and the normalized surface temperature respectively). The functions a,b,g,I_1,I_2,I_3 are defined as:

$$a=\gamma_j(1+\beta\mu_\star'),\quad b=\gamma(1-\cos\bar{\psi}'),\quad g=a/\Theta$$

$$I_1=I_1(u_1)-I_1(u_2),\quad I_1(u)=\int_u^\infty dx\frac{x}{e^x-1}\approx\begin{cases}\zeta(2)-u & u\le 1\\ (1+u)e^{-u} & u\ge 1\end{cases}$$

$$I_2=\ln\left(\frac{1-e^{-u_2}}{1-e^{-u_1}}\right),$$

$$I_3=I_3(u_1)-I_3(u_2),\quad I_3(u)=\int_u^\infty dx\frac{1}{x(e^x-1)}\approx\frac{e^{-u}}{u}.$$

ζ is the Riemann zeta function, $\zeta(2) = \pi^2/6$. The quantities involved are:

$$
\begin{aligned}
u_1 &= \frac{a\epsilon'_l}{\Theta}, \quad u_2 = \frac{a\epsilon'_u}{\Theta} \\
\epsilon'_l &= \frac{\epsilon'}{2\gamma(\gamma-\epsilon')(1-\cos\bar{\psi}')}, \quad \epsilon'_u = \frac{2\epsilon'}{1-\cos\bar{\psi}'}, \quad \epsilon' = \frac{\epsilon}{\delta_D} \\
\mu'_\star &= \frac{\bar{\mu}_\star - \beta}{1-\beta\bar{\mu}_\star}, \quad \bar{\mu}_\star = \frac{x}{r}, \quad \mu'_s = \frac{\mu-\beta}{1-\beta\mu} \\
\cos\bar{\psi}' &= \mu'_\star\mu'_s - \sqrt{1-\mu'^2_\star}\sqrt{1-\mu'^2_s}\cos\bar{\phi}_\star
\end{aligned}
$$

with $\bar{\phi}_\star$ the orbital phase in the stationary star frame. The quantities with a bar are measured in the star's stationary frame.

Then, using equation (A6) of the same work:

$$
f_\epsilon^{C\star} = \frac{\delta_D^4}{d_L^2}\epsilon' V'_b j'_{\nu'}, \tag{2.27}
$$

we obtain the formula for the emission coefficient in the fluid comoving frame :

$$
j'_{\nu'} = \frac{3\sigma_T u^0_\star h}{32\pi m_e c^2}\delta_D^{-1}\nu' \int_{\epsilon'}^{\infty} d\gamma \frac{n_e(\gamma)}{\gamma^2} a^2 \left[g^{-2}(y+y^{-1})I_1 - \frac{2\epsilon'}{\gamma y b g} I_2 + \left(\frac{\epsilon'}{\gamma y b}\right)^2 I_3 \right]. \tag{2.28}
$$

Figure 2.3 compares the approximations for $I_1(u)$ and $I_3(u)$ with numerical integrations. These approximations introduce at most $\approx 10-20\%$ errors over a narrow range.

Bibliography

Abramowitz M., Stegun I. A., 1964, Handbook of mathematical functions with formulas, graphs, and mathematical tables. Vol. 55, US Government printing office

Bodo G., Tavecchio F., 2018, A&A, 609, A122

Cook J., Cheng C.-C., Jacobs V., Antiochos S., 1989, APJ, 338, 1176

Dermer C. D., Böttcher M., 2006, The Astrophysical Journal, 643, 1081

Ghisellini G., 2013, Radiative processes in high energy astrophysics. Vol. 873, Springer

Ghisellini G., Tavecchio F., 2010, MNRAS: Letters, 409, L79

Jüttner F., 1911, Annalen der Physik, 339, 856

Perucho M., 2019, in High Energy Phenomena in Relativistic Outflows VII. p. 99 (arXiv:1912.00235)

Rybicki G. B., Lightman A. P., 1979, Radiative processes in astrophysics. John Wiley & Sons

Walder R., Folini D., 1996, A&A

Wardzinski G., Zdziarski A. A., 2000, Monthly Notices of the Royal Astronomical Society, 314, 183

van Hoof P., Ferland G. J., Williams R., Volk K., Chatzikos M., Lykins M., Porter R., 2015, MNRAS, 449, 2112

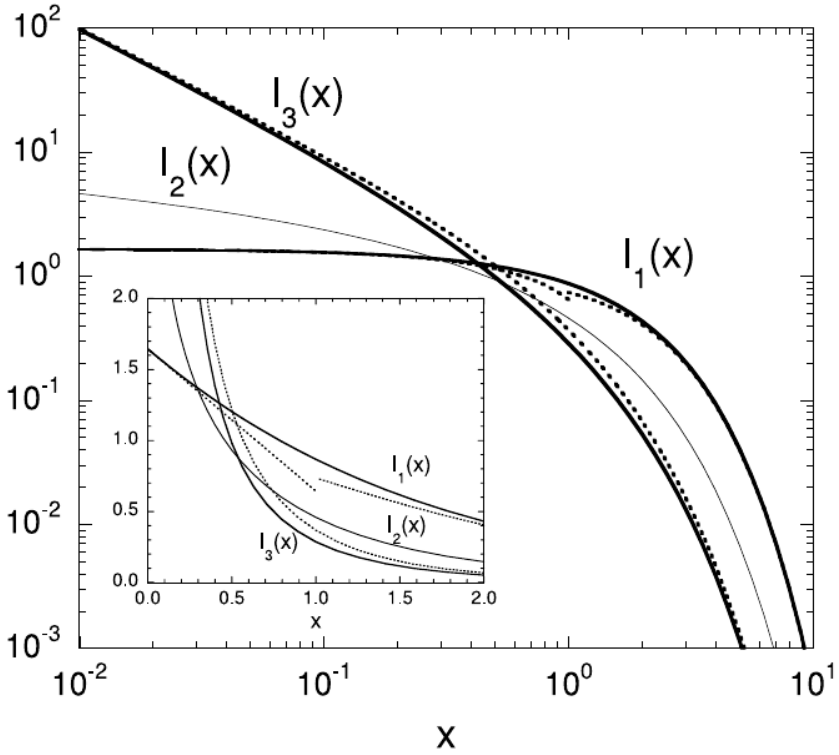

Figure 2.3: From Dermer & Böttcher (2006). Solid lines are the integrals $I_1(u)$, $I_2(u)$, $I_3(u)$, and dotted lines are the approximations for $I_1(u)$ and $I_3(u)$ respectively. The inset shows the comparison on a linear scale.

Chapter 3

Numerical methods and setups

In this chapter, I will present the various numerical tools used during this PhD, beginning with the A-MaZe toolkit used to perform the simulations in section 3.1. This PhD began with the implementation of the relativistic solver in A-MaZe, we thus present benchmarks for the code in section 3.2. The numerical setups for the performed simulations are presented 3.3. The post-processing code I wrote during this PhD to produce scientific datas will be presented section 3.4. Lastly, the procedure to calculate emission from an hydrodynamical simulation is provided section 3.5

3.1 The A-MaZe Toolkit

Simulations were performed with the A-MaZe simulation toolkit (Walder & Folini, 2000; Folini et al., 2003; Melzani et al., 2013) as described in Popov et al. (2019): a collection of adaptive mesh (Berger & Oliger, 1984; Berger & Colella, 1989; Folini et al., 2003) multi-scale, multi-physics codes and analysis tools to support simulations of a various range of astrophysical objects. These studies include accretion and blasts in novæ (Walder et al., 2008), full-scale simulations of X-ray binaries (Walder et al., 2014), colliding winds and emitted spectra (Nussbaumer & Walder, 1993; Folini & Walder, 1999, 2000), particle acceleration in relativistic magnetic reconnection (Melzani et al., 2014b,a), supersonic turbulence (Folini & Walder, 2006a; Folini et al., 2014a) as well as the dynamics of circumstellar material (Folini et al., 2004b; Georgy et al., 2013). The integration scheme used in A-MaZe is described section 3.1.1. For the sake of this work we implemented an inversion routine detailed section 3.1.2 and whose benchmark can be found section 3.2 to solve the equations for relativistic hydrodynamics on a Cartesian, static mesh and without the well-balanced option described in Popov et al. (2019).

3.1.1 Integration scheme

Equation 1.7 is solved using with a finite volume discretisation on mapped grid (Calhoun et al., 2008) for general curvilinear coordinates: a regular Cartesian mesh, the computational mesh, is mapped to the desired mesh in physical space (the physical mesh). In this work, the physical mesh is a 3D Cartesian mesh. We also added the advection of a passive tracer J distinguishing the jet material ($J = 1$) from the ambient medium ($J = 0$).

Semi-discretising equation 1.7 in space results in

$$\frac{\partial \mathbf{U}_{i,j,k}}{\partial t} + \frac{\mathbf{F}_{i+1/2,j,k} - \mathbf{F}_{i-1/2,j,k}}{dx} + \frac{\mathbf{G}_{i,j+1/2,k} - \mathbf{G}_{i,j-1/2,k}}{dy} + \frac{\mathbf{H}_{i,j,k+1/2} - \mathbf{H}_{i,j,k-1/2}}{dz} = \mathbf{\Psi}_{i,j,k}. \tag{3.1}$$

Here, dx, dy, and dz, represents the spatial discretisation in the x-, y-, and z-direction and $\mathbf{U}_{i,j,k}$ is the vector of the discrete conserved variables at cell centers (i, j, k). i, j, and k vary respectively between 1 and N_x, N_y, and N_z, the number of cells in the $x-$, $y-$, and $z-$direction of computational space. Half indices denote cell faces. $\mathbf{F}_{i\pm1/2,j,k}$, $\mathbf{G}_{i,j\pm1/2,k}$, and $\mathbf{H}_{i,j,k\pm1/2}$ denote the fluxes through the cell faces in x-, y-, and z-direction. $\mathbf{\Psi}_{i,j,k}$ represents the source terms, which are also evaluated at cell centers.

In this work, the time integration of the $N_x \times N_y \times N_z$-dimensional system of ordinary differential equations 3.1 is done with a first order Runge-Kutta method (forward Euler method), although A-MaZe also offers strong stability preserving (SSP) higher order integration schemes (Shu & Osher, 1988; Gottlieb et al., 2001). A simple central scheme is used to evaluate the fluxes, as detailed here for the flux through the right x-interface of cell (i, j, k):

$$\mathbf{F}_{i+1/2,j,k} = \frac{F(\mathbf{U}^L_{i+1/2,j,k}) + F(\mathbf{U}^R_{i+1/2,j,k})}{2} - \frac{\lambda_{max}}{2}\left(\mathbf{U}^R_{i+1/2,j,k} - \mathbf{U}^L_{i+1/2,j,k}\right), \tag{3.2}$$

where λ_{max} is the largest characteristic speed and $\mathbf{U}^L_{i+1/2,j,k}$, $\mathbf{U}^R_{i+1/2,j,k}$ are the limited reconstructed variable values to the left and the right of the cell interface $i + 1/2, j, k$ using linear reconstruction and minmod limiters. This integrator is relatively diffuse but easy to implement for any hyperbolic system of equations and for an arbitrary equation of state.

3.1.2 Inversion scheme

We see from equations (1.4, 1.5, 1.6) that primitive variables (ρ, v^j, p) are also necessary to compute the fluxes $\mathcal{F}^i$. The following system is obtained from the definition of the conservative variables:

$$\rho = D/\gamma, \tag{3.3}$$
$$v^j = S^j/\xi, \tag{3.4}$$
$$p = \xi - \tau, \tag{3.5}$$

where $\xi = \gamma^2 \rho h$ needs to be determined to derive the primitive variables. A method adapted to the polytropic EoS is suggested in Del Zanna & Bucciantini (2002). Using equation 3.5, one obtains:

$$\xi = \frac{\gamma^2 \Gamma_1 \tau - \gamma D c^2}{\gamma^2 \Gamma_1 - 1}. \tag{3.6}$$

Using the definitions of the Lorentz factor and $\vec{S}$:

$$\xi^2 = \frac{S^2}{c^2(1 - \gamma^{-2})}. \tag{3.7}$$

The two expressions for ξ are combined to obtain the final equation for γ:

$$\left(\frac{\gamma^2\Gamma_1\tau - \gamma Dc^2}{\gamma^2\Gamma_1 - 1}\right)^2 c^2(1-\gamma^{-2}) - S^2 = 0, \tag{3.8}$$

which is solved numerically using the Brent method (Brent, 1973). Primitive variables are then computed using the formulas:

$$\begin{aligned}
\rho &= D/\gamma, \\
\xi &= \frac{\gamma^2\Gamma_1\tau - \gamma Dc^2}{\gamma^2\Gamma_1 - 1}, \\
v^j &= S^j/\xi, \\
p &= \gamma^{-2}\Gamma_1^{-1}(\xi - \gamma Dc^2).
\end{aligned}$$

This method, albeit quite efficient, is only valid for a polytropic EoS with constant adiabatic index. Mignone & McKinney (2007) suggested a discussion on the validity of this EoS and an inversion method suitable for all EoS, but we find that the method described above is suitable in our case.

3.1.3 Numerical approximation of Bessel K functions

Equation 2.2 and therefore equations 2.6 and 2.9 use the modified Bessel function of the second kind (also called Bessel K function or Macdonald function), especially the ratio K_3/K_2. A Fortran 90 implementation of this function by Moreau (2005) was ported to A-MaZe, but as both functions tends to zero at low temperature, a simple division of $K_3(\Theta^{-1})$ by $K_2(\Theta^{-1})$ caused underflows during calculations, pushing us to modify the method to derive the ratio directly. Figure 3.1 compares our Fortran method with the built-in Bessel K functions from the SciPy package and shows the stability of our method over the whole temperature range compared to a simple division.

3.2 Benchmark for the scheme

Central schemes similar to the one used during this PhD have been widely used to perform (magneto-)hydrodynamical simulations (for instance Del Zanna & Bucciantini, 2002; van der Holst et al., 2008; Del Zanna et al., 2007). Such schemes are easy to implement and very robust, but have the disadvantage to be relatively diffuse (see e.g. Tóth & Odstrčil 1996 for a discussion). As these schemes are not based on (even partial) characteristic decomposition, contact interfaces in particular are smeared out relatively strongly, with consequences on the growth of instabilities along such interfaces.

Central schemes have become more popular again as more sophisticated Riemann solvers – in particular exact solvers – are very CPU costly. Moreover, they are also not really adapted to the situation when more complex physics is involved besides of (M)HD. Flows which include radiation, gravity, and/or particles show a different wave pattern and waves have different velocities than pure (M)HD waves.

There are two ways to overcome this shortcoming: 1) to use higher order spatial reconstruction schemes as e.g. suggested in Del Zanna et al. (2007); or 2) to use meshes

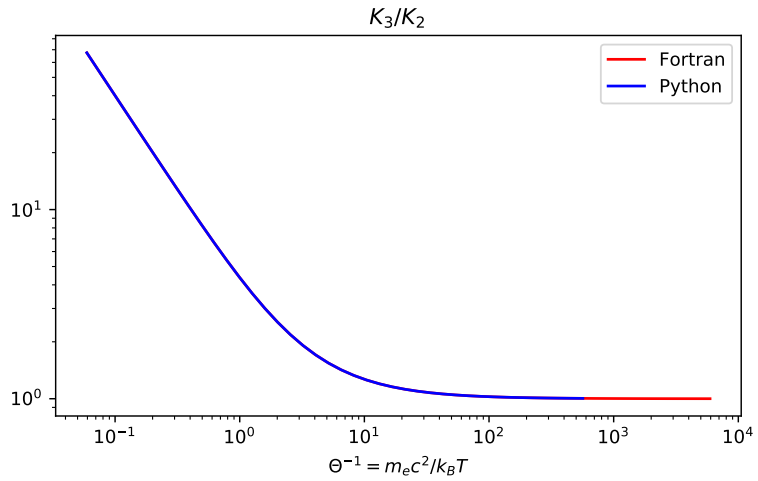

Figure 3.1: Comparison of our Fortran method for the ratio K_3/K_2 with the simple division of both terms using the functions defined in Python package SciPy. Our Fortran method avoids underflows for large values of Θ^{-1} with a relative error never exceeding 10^{-8}.

with a finer spatial discretisation, be it static or through adaptive mesh refinement. This latter approach has been chosen for this work, where we used concentrated static fine meshes along the beam of the jet where instabilities develop, as displayed figure 3.4. Ideally, one may combine the two approaches.

3.2.1 Basic tests of the adiabatic scheme

The central scheme has been used by the authors for other work (Folini et al., 2004a). We tested the implementation of SR by performing about 20 tests as suggested in the literature and found that we can well reproduce these results. We will show two of these tests here. The first is the relativistic blast wave problem as originally proposed by Donat et al. (1998). This Riemann-problem is defined by setting the state to the left/right of the original interface located at 0.5 to $(\rho, v, p)_L = (1, 0, 1000)$ and $(\rho, v, p)_R = (1, 0, 0.01)$, resulting in a $\gamma = 6$ blast shock propagating to the right and a strong rarefaction fan propagating to the left. The solution at $t = 0.35$ on a very fine mesh of 25600 cells is shown in the left panel of figure 3.2. The problem is a tough one and demonstrates why relativistic hydrodynamics is a numerical challenge.

Donat et al. (1998) presented a solution based on a third order scheme combined with the Marquina-solver which is using the full spectral decomposition. Del Zanna & Bucciantini (2002) presented two solutions of the same problem based on a mesh of 400 cells. The first solution is computed with a third order scheme based on the HLL solver (which is using only a part of the spectral information) and using a MC limiter (their CENO3 scheme), the second solution is based on the same method as used in this paper, the second order Lax-Friedrichs-scheme and minmod limiters. The hard part to compute is the thin high-density shell between the shock wave and the contact interface. Such shells are typical for relativistic flows. In figure 3.2, it is located at $t = 0.35$ between $x = 0.84$ and $x = 0.85$, where the density jumps by about two orders of magnitude in the

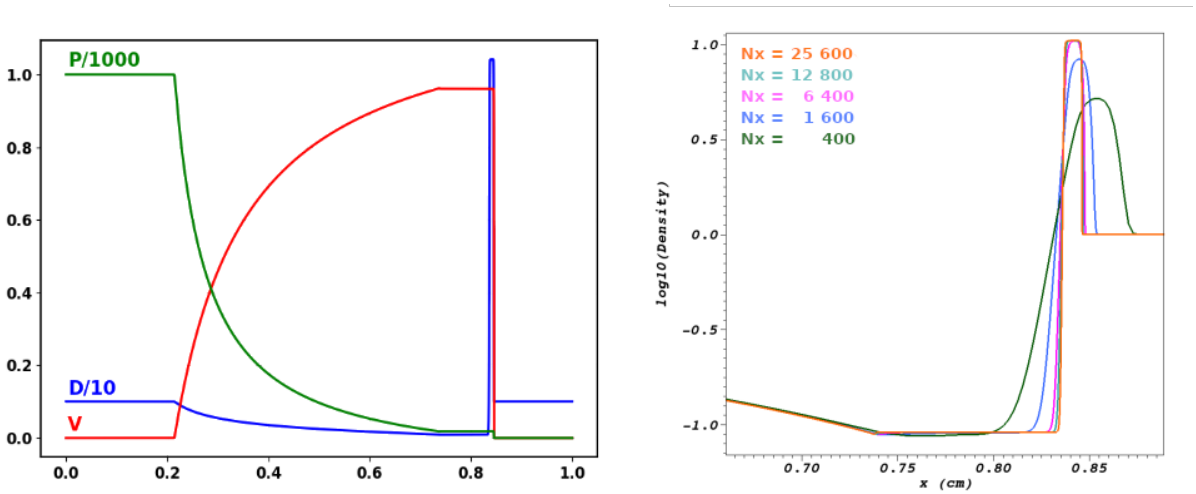

Figure 3.2: The solution of the relativistic blast problem with a Lorentz factor $\gamma = 6$ shock detailed in the text at time $t = 0.35$.
Left: pressure (P), density (D) and velocity (V) as computed on a very fine mesh (25600 cells) showing the shock, the contact discontinuity and the rarefaction fan. **Right:** zoom into the small high density layer between the shock and the contact discontinuity, the most difficult feature to resolve. Shown are the solutions based on different resolutions: 400 cells (black), 1600 cells (blue), 6400 cells (pink), 12800 cells (green), and 25600 cells (orange).

shock wave and three orders of magnitude in the contact interface. Most of the mass is concentrated within a region covering only about 1% of the domain.

Based on a discretisation of 400 cells, none of the described schemes resolved the shell: the third order schemes of Donat et al. (1998) and Del Zanna & Bucciantini (2002) reached a density of about 7.3 in 1-2 cells; the second order LF-scheme in Del Zanna & Bucciantini (2002) reached a density of about 6.5 over 1-2 cells; while the correct value is about 10.5. The convergence of our scheme to the correct density value is demonstrated in the right panel of figure 3.2. With 400 cells, our scheme is in line with the one of Del Zanna & Bucciantini (2002). When using 1600 cells, the density peaks at about 9.0 in 1-2 cells and at near the correct value when using 6400 cells. With 12800 cells the density peak is well resolved, but the contact interface is still somehow smeared out. The simulation using 25600 cells fully resolves the thin shell with some tens of cells and the transition to the contact is quite sharp. We note that the computational costs for our scheme on 1600 cells is probably not (much) more than using a third order scheme and a Riemann solver based on spectral decomposition on 400 cells. This demonstrates that a strategy based on fine meshes and a simple solver can be efficient, but this is at the cost of heavier data files than those produced on a 400 cell mesh.

The second test is the jet-test-case from Del Zanna & Bucciantini (2002): in cylindrical geometry, a $\gamma = 7.1$ jet is launched into a uniform environment with a low pressure, corresponding to a relativistic Mach number of about 17.9. This test is harder to simulate than the jets presented in this paper. The number of cells covering the beam-width is 20, the mesh in the domain is 160×400 in radial- and z-direction respectively. Comparing the result obtained with our code (see figure 3.3) with figure 9 of Del Zanna & Bucciantini

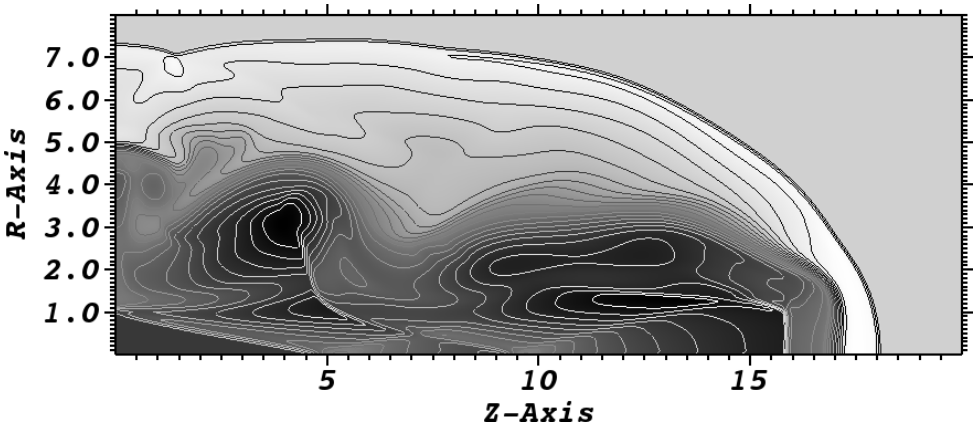

Figure 3.3: Logarithmic density contours and shades for the $\gamma = 7.1$ (Mach ≈ 17.9) jet proposed in Del Zanna & Bucciantini (2002) and reproduced by the scheme used for this work. The image shows $t = 40$ (in code units) and can be directly compared with figure 9, last panel, of Del Zanna & Bucciantini (2002).

(2002), we observe an excellent agreement in the position of the front bow shock, the position of the Mach stem at the end of the beam, the position of the cross shocks in the beam, and the general shape of the cocoon. In our case, the interface between inner and outer cocoon is more smeared out. The smaller modes in the instability developing along this interface are less resolved than in Del Zanna & Bucciantini (2002). This discrepancy is natural as Del Zanna & Bucciantini (2002) used the more accurate CENO3-scheme, while our result is based on the 2nd order in space LF method. However, this drawback can be overcome by using a finer mesh (not shown). In the simulations presented in this work, the mesh resolution is about a factor of 1.5 to 2.5 higher than in the simulation shown in figure 3.3, depending on the exact position of beam and cocoon.

3.2.2 Uncertainty for simulations of turbulent and cooling flows

The exactness of the simulations presented in this paper is harder to estimate. The flows are turbulent and cooling introduces more instabilities, waves, and interfaces. The turbulent region of the cocoon has no fixed boundary but is embedded by shocks and material interfaces into the environment: interior turbulent fluctuations will impact the shape of the interfaces and, inversely, the dynamics of the interfaces will act on the interior turbulence. From these arguments, one cannot expect to find a converged solution in the sense demonstrated in figure 3.2. One thus has to trust the general correctness of the scheme and needs to give some reasons why the presented solutions are close to correct. A rigorous error analysis based on statistical analysis of many simulations that differ slightly in their initial conditions would be desirable, but is sophisticated, complex, and computationally expensive – and thus out of reach for the present study. A step in this direction is nonetheless presented in figure 3.5. We list in the following some points that allow to shed some light on the uncertainties.

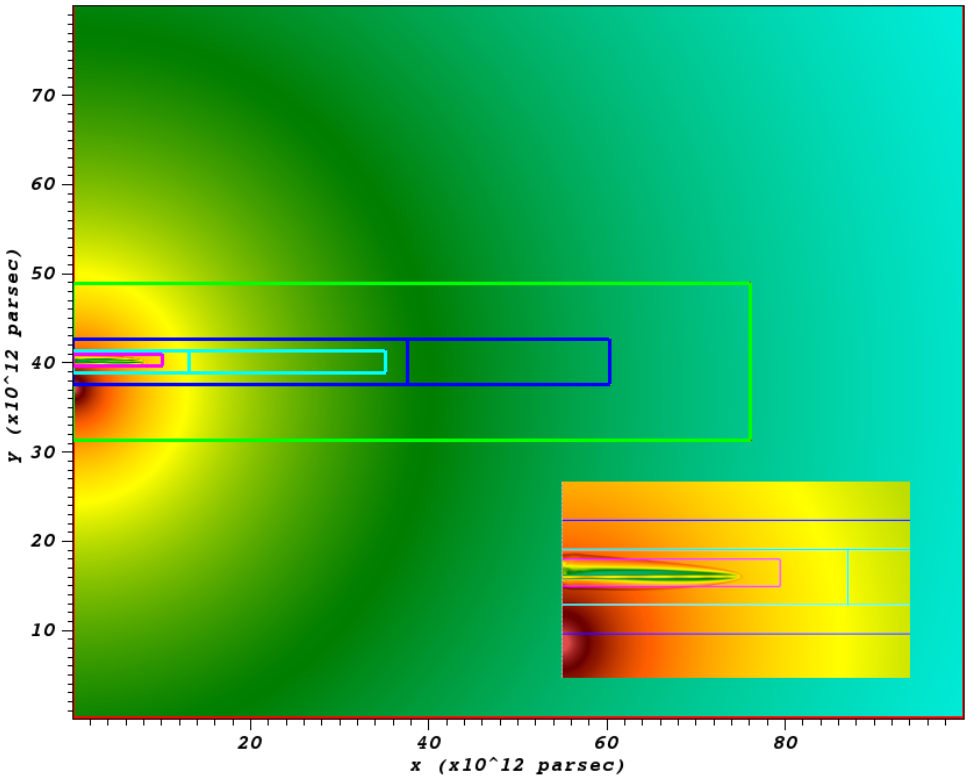

Figure 3.4: Structure of the computational grid over the whole domain, illustrated in the case of a rest mass density slice along the plane containing star and jet center. Density scale goes from 10^{-19} (deep blue) to 10^{-12} g cm^{-3} (red), same as figure 4.1. The grid contains 5 refinement levels: the whole domain is refined twice (green and blue interfaces) by a factor of 4 and then twice more (cyan and magenta interfaces) by a factor of 2 to attain a factor of 64 in the finest level, which are better shown in the zoom on jet injection at orbital scale bottom right of the picture. Cell sizes change suddenly between levels.

Turbulence

Reynolds numbers are too high to resolve the turbulent cascade with any numerical scheme. Moreover, ideal hydrodynamics do not treat diffusion explicitly. But a numerical scheme implicitly introduces a certain diffusion (Hirsch, 2006; LeVeque et al., 2002), which is in astrophysical rarefied flows much larger than the physical diffusion. However, as pointed out by Boris et al. (1992) and further explored by Porter et al. (1992) and Porter & Woodward (1994), finite volume methods as the one used here cut the turbulent cascade in a way not leading to an energy pile-up or -sink at the numerical diffusion scale, thus cutting the cascade correctly at least to first order. Such an approach is termed MILES (Monotone Integrated Large-Eddy Simulation). A more rigorous study to the MILES approach is given e.g. in Garnier et al. (1999) and summary of the idea and more references can be found in Folini & Walder (2006b). These studies show that turbulent flows are relatively well captured by finite volume methods without introducing large errors.

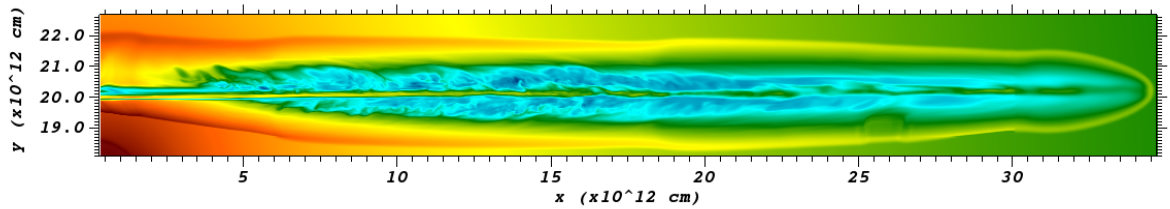

Figure 3.5: Simulation of the fiducial case of CygX1 on a mesh 2 times finer than the simulation presented in figure 4.1. Shown is the simulation at 6000 s, corresponding to the middle panel of figure 4.1.

Cooling

Radiative shocks are prone to an overstability whenever the slope of the cooling law is sufficiently shallow or negative. For a radiative cooling parametrised as a function of density and temperature $\dot{\tau}(\rho, T) = \rho^2 \Lambda(T)$ with $\Lambda(T) = \Lambda_0 T^\beta$, which applies for free-free and line cooling, Chevalier & Imamura (1982) and Bertschinger (1986) have shown that the overstability is present whenever $\beta \lesssim 0.4$ (fundamental mode), and, respectively, $\beta \lesssim 0.8$ (first overtone mode). Previous studies have shown (Walder & Folini, 1996) that presence and amplitude of the overstable modes in a numerical study critically depend on the numerical resolution, as smeared out interfaces radiate more than better resolved ones. The resolution we chose for the simulations are sufficient to resolve the overstability (not shown). It is, however, worth to add two remarks: firstly, the used numerical model does not include mass- and, particularly, heat-diffusion which physically determines the smearing of the interface. It is thus not clear whether we under- or over-estimate this particular effect. Secondly, radiative multi-dimensional shocks can generate and drive turbulence (Walder & Folini, 1998) and turbulent thin-shells (Folini & Walder, 2006b; Folini et al., 2014b).

Resolution comparison

The fiducial case of CygX1 has been simulated on a mesh 2 times finer than the generic mesh up to about 10 000 s. The snapshot at 6000 s is shown in figure 3.5. This can be compared to the snapshot of the generic case shown in the middle panel of figure 4.1. The comparison shows that the instability sets in at about the same time in both of the simulations. However, in the simulation on the finer mesh, the jets propagates about 10% faster than in the simulation on the generic mesh. We also observe similar effects, of the same order, in 1D test simulations. This is expected on the basis of the arguments given in the point above. Better resolving the contact interface at the head of the jet will reduce cooling there, leaving slightly more energy to push the bow shock to a larger distance. Note that an error of 10% is already a quite good result for most hydrodynamical simulations. We stress again that the correct jet speed depends on the physical diffusion.

To even improve the confidence in the solutions presented in this paper, we ran a 2D resolution study using the generic and the finer mesh from the 3D case. This study also covers the turbulent phase. Again we find that the essential features of the jet such as

number and location of the cross shocks, cocoon shape, time when the instability and the turbulence sets in, are independent of the resolution. Note, however, that the 2D simulations cannot be directly compared to the 3D simulations as the character of the turbulence is different in 2D and 3D.

3.3 Numerical setups

We define runs CygX1 and CygX3 as our fiducial runs for Cygnus X-1 and Cygnus X-3 respectively. The main parameters values for these two runs are given in table 3.1. The choice of physical values have been inspired by Orosz et al. (2011) and Yoon & Heinz (2015) for Cygnus X-1, and by Zdziarski et al. (2013) and Dubus et al. (2010) for Cygnus X-3. Parameter choices for the various sensitivity studies are listed in tables 3.2 and 3.3, while their corresponding dimensionless parameters (introduced section 1.3) are given table 3.4.

Our simulations were set in a static grid made of five refinement levels centered on the jet injection nozzle, as shown in Fig. 3.4. Cells from the coarse grid had a $4 \cdot 10^{11}$ cm edge, and the edge of the highest-level cells was 64 times lower for a maximum resolution of $6.25 \cdot 10^{9}$ cm. The number of coarse level grid cells was $250 \times 200 \times 200$ and $250 \times 150 \times 150$ for Cygnus X-1 and Cygnus X-3, respectively. The associated physical domain sizes are given in Table 3.1. The cfl number was set to 0.15. The time step was refined along with the spatial grid. On the coarse grid, it was about 2 s for Cygnus X-1 and 5 s for Cygnus X-3. The jet was injected perpendicular to the orbital plane (y-z plane) by fixing $(\rho_j, \vec{v}_j, T_j)$ on a few cells at $x = 0$, always imposing at least 20 cells of the finest grid to fix the diameter of the beam. The environment was set by fixing the wind velocity and density at the stellar surface, resulting in an isotropic wind with constant speed modulus and density in r^{-2}. The boundary condition the at x=0 plane was reflective, while the other boundaries of the simulation grid had outflow conditions.

3.3.1 Physical parameters

Table 3.1 shows the value of the environment parameters relevant for jet radiative losses as well as the parameters of the respective fiducial runs. The characteristics of the Cygnus X-3 system mean the radiative losses will be stronger overall. We chose a higher magnetic field base value for Cygnus X-3 to compensate the addition of the distance scaling detailed in section 2.1.5, and the luminosity of the two companion stars are about the same (the companion star in Cygnus X-3 is hotter but smaller), but the smaller orbital distance implies stronger synchrotron and inverse Compton losses by a factor 100. Secondly, the beam density ρ_j was chosen 10 times greater than in Cygnus X-1 runs, implying stronger line and free-free losses by a factor 100 also. The jets have roughly the same internal energy density in both cases, being launched with the same temperature T_j, but will cool a ~ 100 times faster in Cygnus X-3 case. We verify this by comparing position and speed diagrams figures 4.6 and 4.7: the first cooling effects are seen after 7600 s in Cygnus X-1 case, when the first cooling effects are visible after 100 s in Cygnus X-3 case.

	Cygnus X-1	Cygnus X-3	unit
ρ_j	$1.3 \cdot 10^{-15}$	$1.4 \cdot 10^{-14}$	g cm^{-3}
v_j	10^{10}	$2.25 \cdot 10^{10}$	cm s^{-1}
T_j	10^8	10^8	K
d_{orb}	$3 \cdot 10^{12}$	$2.6 \cdot 10^{11}$	cm
$R_\star$	16.2	2.3	$R_\odot$
$T_\star$	$3 \cdot 10^4$	$8 \cdot 10^4$	K
$B_\star$	10	100	G
$\dot{M}_\star$	$3 \cdot 10^{-6}$	10^{-5}	$M_\odot$yr^{-1}
v_∞	1000	1500	km s^{-1}
x_{max}	10^{14}	10^{14}	cm
y_{max}, z_{max}	$8 \cdot 10^{13}$	$6 \cdot 10^{13}$	cm

Table 3.1: Main parameters of fiducial runs, environment base values and domain size for Cygnus X-1 and Cygnus X-3 runs. The choice of physical parameters has been inspired by Orosz et al. (2011) for Cygnus X-1 and Zdziarski et al. (2013) for Cygnus X-3.

	CygX1	_noLoss	_wind	_mP	_T7	_T9	units
L_j	5.1	5.1	5.1	0.51	5.1	5.1	10^{36} erg s^{-1}
ρ_j	1.3	1.3	1.3	0.13	1.3	1.3	10^{-15} g cm^{-3}
v_j			10^{10}				cm s^{-1}
r_0			$5 \cdot 10^{10}$				cm
T_j	10^8	10^8	10^8	10^8	10^7	10^9	K
B_j	10	0	10	10	10	10	G
$\dot{M}_\star$			$3 \cdot 10^{-6}$				$M_\odot$ yr^{-1}
v_∞	1000	1000	1500	1000	1000	1000	km s^{-1}
$T_\star$			$3 \cdot 10^4$				K
$B_\star$	10	0	10	10	10	10	G

Table 3.2: Simulation parameters of runs based on Cygnus X-1.

	CygX3	_noLoss	_mW	_mP	_mPmW	_mPmmW	units
L_j	10	10	10	5.0	5.0	5.0	10^{37} erg s^{-1}
ρ_j	14	14	14	7.0	7.0	7.0	10^{-15} g cm^{-3}
v_j				$2.25 \cdot 10^{10}$			cm s^{-1}
r_0				$2 \cdot 10^{10}$			cm
T_j				10^8			K
B_j				10			G
$\dot{M}_\star$	1	1	.75	1	.75	.75	$10^{-5} M_\odot$ yr^{-1}
v_∞	1500	1500	1000	1500	1000	750	km s^{-1}
$T_\star$				$8 \cdot 10^4$			K
$B_\star$				100			G

Table 3.3: Simulation parameters of runs based on Cygnus X-3.

setup name	β_j	M_j	$\mathcal{M}_j$	η	η^*	K
CygX1	0.334	67	71	0.077	0.087	258
CygX1_noLoss	0.334	67	71	0.077	0.087	258
CygX1_wind	0.334	67	71	0.116	0.130	387
CygX1_mP	0.334	67	71	0.008	0.009	26
CygX1_T7	0.334	211	224	0.077	0.087	26
CygX1_T9	0.334	21	22	0.077	0.087	2577
CygX3	0.75	150	228	0.0028	0.0065	3.5
CygX3_noLoss	0.75	150	228	0.0028	0.0065	3.5
CygX3_mW	0.75	150	228	0.0025	0.0058	3.1
CygX3_mP	0.75	150	228	0.0014	0.0032	1.8
CygX3_mPmW	0.75	150	228	0.0013	0.0029	1.6
CygX3_mPmmW	0.75	150	228	0.0009	0.0022	1.2

Table 3.4: Dimensionless parameters of the runs performed.

3.3.2 The need for a relativistic solver

Given that the computational costs are considerably higher for a relativistic simulation, one may ask whether it is necessary to perform relativistic simulations to obtain correct solutions for the mildly relativistic problems presented in this paper, with $\gamma_b \approx 1.06$ for CygX1 and $\gamma_b \approx 1.51$ for CygX3. However, even these small Lorentz factors lead to a significant difference in the jet propagation between a relativistic and a Newtonian simulation. This is illustrated in figure 3.6 which shows 1D simulations at (observer) time $t = 6500$ s of the jet propagation of CygX3, all parameters similar to the fiducial case including all cooling terms, over a 12 800 cells mesh. The jet head is located in the thin high-density shell. In the Newtonian case this shell is located, in the observers frame, at about $x = 45 \cdot 10^{12}$ cm. The shell in the relativistic case is located at $x = 71 \cdot 10^{12}$ cm. Thus, the relativistic jet head propagates about 1/3 faster than the Newtonian one. This can be explained on the basis of equation 1.19: the ratio between η^* and η for CygX3 (see table 3.4) is about 2.3, resulting in a difference in the jet-propagation speed of about 45%. There is less difference for CygX1, but still about 5%. Note that in 1D the shocked beam will cool down, in contrast to the multi-D simulations where the beam is regularly re-heated by the cross-shocks.

3.4 Post-processing methods

To perform quantitative analysis on our simulations, efficient post-processing methods are required as each simulation snapshot is ∼15 GB of data. Simulation snapshots use the hdf5 file format and are structured into subgrids, therefore the Python code to hold the data and perform analysis reproduce this structure in a tree of NumPy arrays. The code for this computational tree loading A-MaZe simulation data files into a Python object had already been written by Maxime Viallet several years ago for simple data visualisation, it served as the core component of the post-processing code I will detail here.

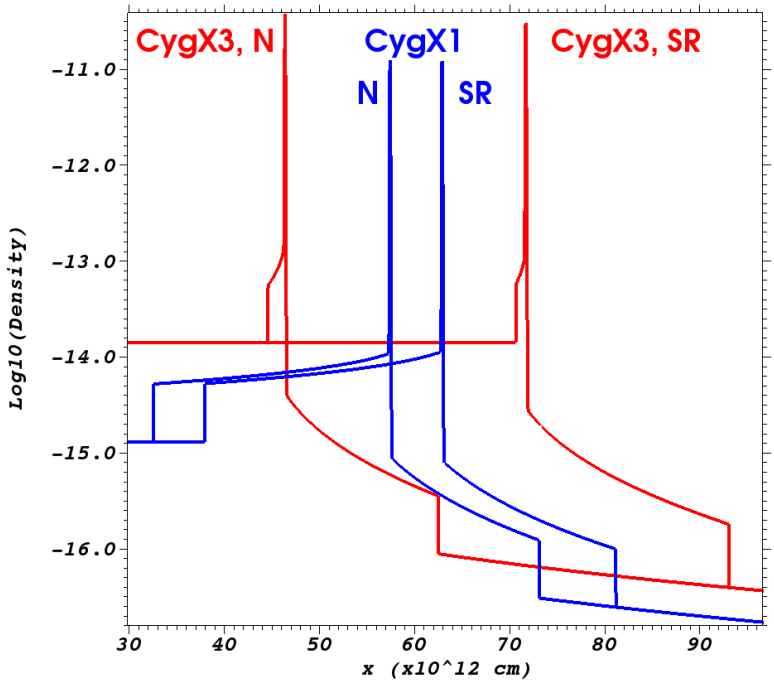

Figure 3.6: Comparison in density profiles of 1D simulations for parameters similar to the fiducial cases. Shown is, in the observer frame, the comparison between a Newtonian and a relativistic simulation for CygX1 at 30'000 s (blue) and for CygX3 for 6500 s (red). The simulations include all cooling terms. The pattern with forward and reverse shock and a thin layer of cooled gas to the left of the contact interface between beam and environment material is similar for all simulations. The mesh consists of 12800 cells, about as much as the mesh covering the beam in the 3D simulations presented in the paper.

3.4.1 Data tree

The first step in the post-processing procedure consists in creating a tree class to hold all the datas from a simulation snapshot, loading them into the RAM for faster access. The tree is designed to reflect the structure of data files produced by A-MaZe: the simulation box is divided in levels, each level divided in a certain number of grids. Each grid contains 1D data tables (or 2D for vector values such as the velocity), the range in the x, y and z directions in the chosen length unit (cm in our case), and the number of cells in each direction: n_x, n_y, and n_z. Thus, the tree is built by reading the data file level after level, for each one creating a level in the tree, and for each grid of the said level in the data file, a corresponding grid is created in the tree. This tree grid contains the values of the data grid, one NumPy array per variable, which are then reshaped as (n_x, n_y, n_z) (or $(3, n_x, n_y, n_z)$ for the velocity). It is to be noted that A-MaZe is a FORTRAN code, and one must be careful of the ordering when reshaping datas: the $n_x \times n_y \times n_z$ 1D array needs to be reshaped as (n_z, n_y, n_x) and then transposed for the datas to be in the correct order for later NumPy array operations. For each tree grid, the coordinates are reconstructed using the ranges and the number of cells in each direction, and the meshgrid method is used to construct coordinates arrays with the same shape as the arrays containing the

datas.

3.4.2 Jet structure and cell identification

Once all the datas from an A-MaZe output file have been loaded in a tree, the first step needed to analyse the jet evolution is separating the jet from the ambient medium in the data. From the description of the jet zones introduced 1.3, we chose the following rules for the various interfaces of the jet: the separation between ambient material and outer cocoon is made at $p = .01$ Ba & $T = 10^7$ K, the working surface between inner and outer cocoon is defined where $J = 0.05$ following the definition for the mixing layer in Perucho et al. (2004), and cells are considered part of the beam if $\zeta \equiv (v_x/v_j)J > 0.8$. This criterion is defined in Yoon & Heinz (2015), we found choosing 0.8 as threshold value identifies the beam up to the reverse shock with more success than a criterion purely based on J, especially in the latter phases of the jet outbreak when beam and inner cocoon mixes. The value $J = 0.05$ has been found to segregate correctly the low-density, high-temperature inner cocoon from the outer cocoon. These criterions are deemed correct in the sense that their limits correspond to the jumps in the various physical quantities between jet zones. Redundant cells between the different refinement levels are then ignored to avoid errors. This is performed by applying the following algorithm: for each grid with nonzero values of 'Structure' in a refinement level, we check the intersection in terms of coordinates with grids of the lower (i.e. less refined) level. If this intersection is nonzero, the 'Structure' value of cells from the lower level grid in that intersection is set to zero.

3.4.3 Data extraction

After having identified each computational cell as part of a zone, several diagnostics can be performed. The first kind is measuring length of the different jet zones, which is easily obtained by iterating over the grids to find the x-most position of the cells with set value: for example, finding the x-most position with Structure = 2 returns the length of the inner cocoon, which is assumed to be the position of the contact discontinuity at jet head. Adding the volume of cells with a set Structure value gives us the volume of each jet zone, this process is also used to obtain various volume-averaged values (rest-mass density, temperature, velocity, pressure, internal energy density, kinetic energy density, power losses due to the radiative mechanism) over a specific jet zone. The same process is also used to obtain partition density function (PDF) for quantities such as temperature over the jet. These datas are extracted for each snapshot of a simulation run and written in plain text files for later use without needing to re-extract these datas from the simulation output. This extraction is a lengthy process of a few minutes per file, analysing an entire run takes about two days. The longest step in this process is the construction of the tree whose speed is bound by the bandwidth between the data storage and the RAM of the machine used.

3.4.4 Data analysis

Once the relevant datas have been extracted from a simulation run, we can proceed to their analysis in the framework of our physical models. This begins with reading the

numerical setup of a run (jet density, jet speed, jet temperature, stellar radius, stellar temperature, stellar mass-loss rate, etc.) from the metadatas of a simulation output, assigning the corresponding values to variables defined in a dedicated module, which also contains all the relevant physical constants. Several analytical estimates are then derived from these environment variables such as the position of the initial recollimation shock and the jet bending (Yoon & Heinz, 2015; Yoon et al., 2016) or the 1D propagation speed derived section 1.1.2.

Reading the extracted datas allows for more diagnostics such as the derivation of the KHI growth timescale as derived section 1.2.2: the variables from equation 1.17 are read from the first simulated timesteps of a run and the equation is solved for the first modes ($n \leq 4$) for each of these first timesteps. The jet structure establishing itself over the first few simulation timesteps[1], the KHI growth time is determined once it is the case as the lowest values from all the considered modes.

3.4.5 Data access and visualisation

The last part of my post-processing code is the data visualisation and plotting. Data visualisation is performed with the interactive parallel visualization and graphical analysis tool VisIt, using scripts to generate e.g. slices of a simulation variable automatically zoomed on the jet. Repeating this over a full run allows the production of movies of the simulations. The plotting of the extracted datas is done using the matplotlib library for Python. Automated scripts allows for easy plotting of any variable of interest versus the simulated time: jet propagation and speed, per-zone pressure (derived from the volume-averaged densities and temperature), zone volumes, etc. We also define a proxy for the jet aspect ratio as $(\pi l^3/V)^{1/2}$ with l and V total length and volume of the jet respectively. This is equivalent to the ratio $l/r_{j,eff}$, where $r_{j,eff}$ is the radius of a cylindrical jet of length l and volume V.

To render the plotting process as easy as possible, dictionaries containing all the relevant informations on a run such as the respective folders where simulation output and extracted datas are stocked or the run name were created in a dedicated module. The various functions presented in sections 3.4.3, 3.4.4 and here call to these dictionaries to automatically perform all the described tasks. In particular, the script automatically plots comparison of a chosen variable between several runs by giving the run names as arguments. The figures in section 4 were all plotted using these methods.

3.5 Numerical calculation of the radiation emitted by a relativistic source

We detail here the procedure to calculate the radiation emitted by a relativistic source as presented in De Colle et al. (2012), following Granot & Ramirez-Ruiz (2012). In comparison to De Colle et al. (2012), we neglect the effects of the cosmological expansion due to the very low redshift of our sources of interest Cygnus X-1 and Cygnus X-3. The geometry of the problem is presented figure 3.7. θ_{sd} is the angle between the local direction

[1] since the initial conditions as t = 0 s are a cylinder with jet values surrounded by ambient material, a few timesteps are needed before the beam/inner cocoon/outer cocoon structure is established

$\hat{n}$ of the contributing part of the jet to the observer and $\hat{n}_d$ the direction of the observer, which is perpendicular to the differential area of the detector dA and pointing towards the detector. This angle is always very small in practice as the source size is much smaller than the distance to the observer, $\theta_{sd} \ll 1$ thus $\cos\theta_{sd} \approx 1$. The solid angle sustended by the contributing portion of the source is defined as $d\Omega_{sd} = d\phi_{sd} d\cos\theta_{sd}$. The aim goal is to calculate the observed flux density $F_\nu = dE/dAd\nu dt$, defined as the energy received by the observer per unit area, frequency, and time.

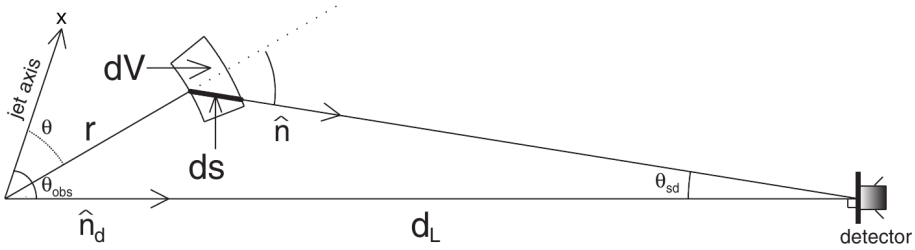

Figure 3.7: Figure and description from De Colle et al. (2012). Contribution of a volume element dV to the flux observed by a distant observer $dF_\nu(\vec{n_d}) = I_\nu(\vec{n})\cos\theta_{sd} d\Omega_{sd}$. θ_{sd} is the angle between the direction opposite to that at which the detector is pointing ($\vec{n_d} = \vec{e_x}$ in the figure) and the local direction from a small emitting region (of volume dV) within the source to the detector. Since the observer is faraway, the direction of emission in the observer frame is almost parallel to the x-axis.

Introducing $I_\nu(\hat{n}) = dE/dAd\Omega d\nu dt$ as the specific intensity, which is the energy per unit area, time, and radiation frequency directed within the solid angle $d\Omega$ centered on the direction $\hat{n}$, the differential contribution to the flux can be written as

$$dF_\nu(\hat{n}_d) = I_\nu(\hat{n})\cos\theta_{sd} d\Omega_{sd} \approx I_\nu(\hat{n}) d\Omega_{sd} = I_\nu dS_\perp / d_L^2, \tag{3.9}$$

where d_L is the distance between the source and the observer and $dS_\perp$ the differential area in the plane of the sky.

$I_\nu = \int j_\nu ds$ for an optically thin source, where $j_\nu = dE/dV d\Omega d\nu dt$ is the emission coefficient, defined as the emitted energy per unit volume, solid angle, frequency, and time, and ds is the differential path length along the trajectory of a photon reaching the observer a the time t_{obs} when the flux F_ν is measured. The emitting element moving with a velocity $\vec{\beta}c$ in the source frame, the emission coefficient in the source frame is

$$j_\nu = \delta_D^2 j'_{\nu'}, \tag{3.10}$$

with $\delta_D = \left[\gamma(1 - \hat{n}\cdot\vec{\beta})\right]^{-1}$ the Doppler factor as defined equation 2.26, and $j'_{\nu'}$ is measured in the comoving frame of the emitting material. This gives the following expression for the flux:

$$F_\nu(t_{obs}, \hat{n}) = \frac{1}{d_L^2}\int d^4x\, \delta\left(t - \frac{\hat{n}\cdot\vec{r}}{c} - t_{obs}\right)\delta_D^2 j'_{\nu'}, \tag{3.11}$$

where t is the coordinate time in the source frame, $\nu' = \gamma(1 - \hat{n}\cdot\vec{\beta})$, and $t_{obs} = \left(t - \frac{\hat{n}\cdot\vec{r}}{c}\right)$. $t_{obs} = 0$ corresponds to a photon emitted at the origin ($\vec{r} = 0$) at $t = 0$.

Two main approaches exist to calculate F_ν from the results of a numerical simulation. The first one consists in numerically calculating I_ν along the line of sight and then computing $dF_\nu = I_\nu dS_\perp / d_L^2$, it can therefore properly handle the optically thick regime and

even provides the observed image of the source (I_ν on the sky plane) as a by-product, at the cost of needing to access many simulation snapshots at the same time to properly follow the world line of the photons reaching the observer. Due to the size of such snapshots, this method cannot be applied without huge RAM capacities and is therefore not chosen for this work.

The second approach avoid this difficulty by dividing the range of observed times t_{obs} into a finite number of time bins of width $\Delta t_{obs,i}$ centered on $t_{obs,i}$: the i-th bin corresponds to $t_{obs,i} - \Delta t_{obs,i/2} < t_{obs} < t_{obs,i} + \Delta t_{obs,i/2}$. If the time bins density is such that the second-order derivative $\partial^2_{t_{obs}} F_\nu$ is correspondingly small, the flux can be approximated by its average value within the i-th time bin:

$$F_\nu(t_{obs,i}, \hat{n}) = \frac{1}{\Delta t_{obs,i}} \int_{t_{obs,i}-\Delta t_{obs,i/2}}^{t_{obs,i}+\Delta t_{obs,i/2}} dt_{obs} F_\nu(t_{obs}, \hat{n}). \tag{3.12}$$

From this equation and using the following property of the δ function: $\delta\left[f(x - x_0)\right] = \delta(x - x_0)/f'(x_0)$ when the function f has a single root at x_0, one obtains:

$$F_\nu(t_{obs,i}, \hat{n}) = \frac{1}{d_L^2 \Delta t_{obs,i}} \int d^4x H\left(\frac{\Delta t_{obs,i}}{2} - \left|t_{obs} - t + \frac{\hat{n}\cdot\vec{r}}{c}\right|\right) \delta_D^2 j'_{\nu'}, \tag{3.13}$$

where $H(x)$ is the Heaviside step function. Then, by considering the simulation snapshots as a collection of 4D space-time cells of time-width $\Delta t_j = (t_{j+1} - t_{j-1})/2$ around the snapshot done at time t_j, and evaluating for each cell the fraction f_{ijk} of its 4 volume $\Delta V^{(4)}_{jk} = \Delta t_j \Delta V^{(3)}_{jk}$ that falls within each observer time bin (subscript k refers to the k-th 3D cell of a simulation snapshot), De Colle et al. (2012) obtain this discretised form of equation 3.13:

$$F_\nu(t_{obs,i}, \hat{n}) = \frac{1}{d_L^2 \Delta t_{obs,i}} \sum_{j,k} f_{ijk} \Delta V^{(4)}_{jk} \delta^2_{D,jk} j'_{\nu',jk}. \tag{3.14}$$

The order of summation is not important, and thus one can evaluate the contributions of each 4D cell by iterating over the snapshots. A last simplification consists in attributing all of the contribution from any given 4D cell to a single observer time interval corresponding to the cell center:

$$\Delta F_{\nu,i,jk}(\hat{n}) = \frac{1}{d_L^2} \frac{\Delta V^{(4)}_{jk}}{\Delta t_{obs,i}} \delta_{D,jk} j'_{\nu',jk} \qquad \text{for } \left|t_{obs,i} - t_j + \frac{\hat{n}\cdot\vec{r}_{jk}}{c}\right| < \frac{\Delta t_{obs,i}}{2}. \tag{3.15}$$

The contributions $\Delta F_{\nu,i,jk}(\hat{n})$ are then summed to obtain the desired flux.

Bibliography

Berger M. J., Colella P., 1989, Journal of computational Physics, 82, 64

Berger M. J., Oliger J., 1984, Journal of computational Physics, 53, 484

Bertschinger E., 1986, ApJ, 304, 154

Boris J. P., Grinstein F. F., Oran E. S., Kolbe R. L., 1992, Fluid Dynamics Research, 10, 199

Brent R., 1973, Algorithms for Minimization without Derivatives, Prentice-Hall, Englewood Cliffs, NJ

Calhoun D. A., Helzel C., LeVeque R. J., 2008, SIAM review, 50, 723
Chevalier R. A., Imamura J. N., 1982, ApJ, 261, 543
De Colle F., Granot J., López-Cámara D., Ramirez-Ruiz E., 2012, The Astrophysical Journal, 746, 122
Del Zanna L., Bucciantini N., 2002, Astronomy & Astrophysics, 390, 1177
Del Zanna L., Zanotti O., Bucciantini N., Londrillo P., 2007, Astronomy & Astrophysics, 473, 11
Donat R., Font J. A., Ibáñez J. M. S. S., Marquina A., 1998, Journal of Computational Physics, 146, 58
Dubus G., Cerutti B., Henri G., 2010, MNRAS: Letters, 404, L55
Folini D., Walder R., 1999, in Symposium-International Astronomical Union. pp 352–353
Folini D., Walder R., 2000, Astrophysics and Space Science, 274, 189
Folini D., Walder R., 2006a, Astronomy & Astrophysics, 459, 1
Folini D., Walder R., 2006b, A&A, 459, 1
Folini D., Walder R., Psarros M., Desboeufs A., 2003, in Stellar Atmosphere Modeling. p. 433
Folini D., Heyvaerts J., Walder R., 2004a, A&A, 414, 559
Folini D., Heyvaerts J., Walder R., 2004b, Astronomy & Astrophysics, 414, 559
Folini D., Walder R., Favre J. M., 2014a, Astronomy & Astrophysics, 562, A112
Folini D., Walder R., Favre J. M., 2014b, A&A, 562, A112
Garnier E., Mossi M., Sagaut P., Comte P., Deville M., 1999, Journal of Computational Physics, 153, 273
Georgy C., Walder R., Folini D., Bykov A., Marcowith A., Favre J. M., 2013, Astronomy & Astrophysics, 559, A69
Gottlieb S., Shu C.-W., Tadmor E., 2001, SIAM Review, 43, 89
Granot J., Ramirez-Ruiz E., 2012, Gamma-ray Bursts, 51, 215
Hirsch C., 2006, Numerical Computation of Internal and External Flows. Butterworth-Heinemann Limited, https://books.google.ch/books?id=bvnhAAAACAAJ
LeVeque R., Ablowitz M., Davis S., Hinch E., Iserles A., Iserles U., Ockendon J., Olver P., 2002, Finite Volume Methods for Hyperbolic Problems. Cambridge Texts in Applied Mathematics, Cambridge University Press, https://books.google.ch/books?id=0_ZjpMSZiwoC
Melzani M., Winisdoerffer C., Walder R., Folini D., Favre J. M., Krastanov S., Messmer P., 2013, Astronomy & Astrophysics, 558, A133
Melzani M., Walder R., Folini D., Winisdoerffer C., Favre J. M., 2014a, Astronomy & Astrophysics, 570, A111
Melzani M., Walder R., Folini D., Winisdoerffer C., Favre J. M., 2014b, Astronomy & Astrophysics, 570, A112
Mignone A., McKinney J. C., 2007, Monthly Notices of the Royal Astronomical Society, 378, 1118
Moreau J.-P., 2005, Numerical Analysis by Jean-Pierre Moreau, http://jean-pierre.moreau.pagesperso-orange.fr
Nussbaumer H., Walder R., 1993, Astronomy and Astrophysics, 278, 209
Orosz J. A., McClintock J. E., Aufdenberg J. P., Remillard R. A., Reid M. J., Narayan R., Gou L., 2011, APJ, 742, 84

Perucho M., Marti J.-M., Hanasz M., 2004, Astronomy & Astrophysics, 427, 431
Popov M. V., et al., 2019, A&A, 630, A129
Porter D. H., Woodward P. R., 1994, ApJS, 93, 309
Porter D. H., Pouquet A., Woodward P. R., 1992, Theoretical and Computational Fluid Dynamics, 4, 13
Shu C.-W., Osher S., 1988, Journal of Computational Physics, 77, 439
Tóth G., Odstrčil D., 1996, Journal of Computational Physics, 128, 82
Walder R., Folini D., 1996, A&A
Walder R., Folini D., 1998, A&A, 330, L21
Walder R., Folini D., 2000, in Thermal and Ionization Aspects of Flows from Hot Stars. p. 281
Walder R., Folini D., Shore S. N., 2008, Astronomy & Astrophysics, 484, L9
Walder R., Melzani M., Folini D., Winisdoerffer C., Favre J. M., 2014, arXiv preprint arXiv:1405.0600
Yoon D., Heinz S., 2015, The Astrophysical Journal, 801, 55
Yoon D., Zdziarski A. A., Heinz S., 2016, Monthly Notices of the Royal Astronomical Society, 456, 3638
Zdziarski A. A., Mikołajewska J., Belczyński K., 2013, MNRAS: Letters, 429, L104
van der Holst B., Keppens R., Meliani Z., 2008, Computer Physics Communications, 179, 617

Chapter 4

Structure and dynamics of cooled high-mass microquasar jets

The results we are going to present are, to the best of our knowledge, the first 3D simulations of jets in high-mass microquasars that are relativistic and include radiative cooling in parametrised form. They cover the evolution of the jet from its launching, over the onset of instabilities and radiative cooling, to the turbulent phase at the end of our simulations.

More specifically, we discuss the propagation of the jet through the stellar wind, from its outburst close to the black hole up to scales of about $6 \cdot 10^{13}$ cm for Cygnus X-1, corresponding to about 20 times the separation between the two stellar components d_{orb}, and respectively $2 \cdot 10^{13}$ cm $\approx 75\ d_{orb}$ for Cygnus X-3 (the values for d_{orb} are consigned table 3.1). We begin with a presentation of our fiducial simulations in section 4.1, with particular focus on the development of KHI and its role in different phases of jet propagation, as well as cocoon evolution. Then, the impact of radiative losses on jet structure and dynamics is investigated section 4.2, before performing a small parameter study section 4.3 over the jet temperature, kinetic power and stellar wind.

4.1 Cygnus X-1 and Cygnus X-3 fiducial cases

We start with a description of the fiducial cases for Cygnus X-1 and Cygnus X-3, respectively, against which all other sensitivity studies will be compared later on. Converting the numerical values of the parameters to the dimensionless quantities introduced section 1.3 (table 3.4) places our jets in the supersonic case with extended, turbulent cocoons and a beam with rich internal structure. Our fiducial runs indeed follow these expectations: the evolution of the jet is shown figures 4.1 and 4.2 for the CygX1 run, 4.3 and 4.4 for CygX3. Several features catch the eye, which we further elaborate on below. First, there is qualitative change in the appearance of the jet, from an early 'well ordered' state to a turbulent state later on. This change is also reflected in the propagation of the jet head and three phases of the jet evolution can be identified. Second, the aspect ratio of the jet is different for Cygnus X-1 and Cygnus X-3. Third, jet bending due to the lateral wind impact is observed in all simulations. Fourth, the jet is asymmetric due to the wind of the companion star.

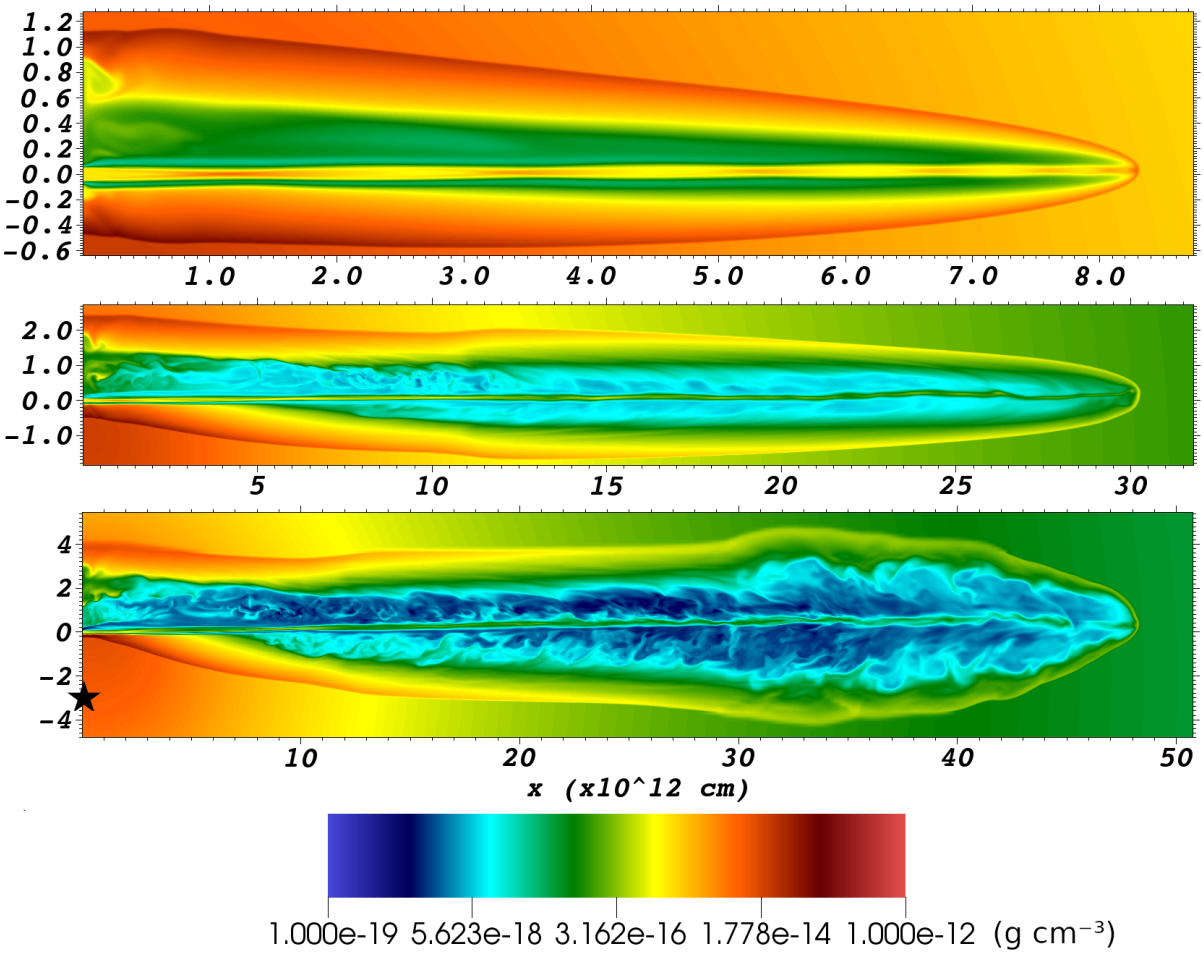

Figure 4.1: Rest-mass density slices of run CygX1 at times (top to bottom) t = 2000, 6000 and 12000 s, showcasing the 3 evolutionary phases detailed in the text section 4.1. The approximate position of the star on the grid (not visible on this slicing) is shown by the star symbol.

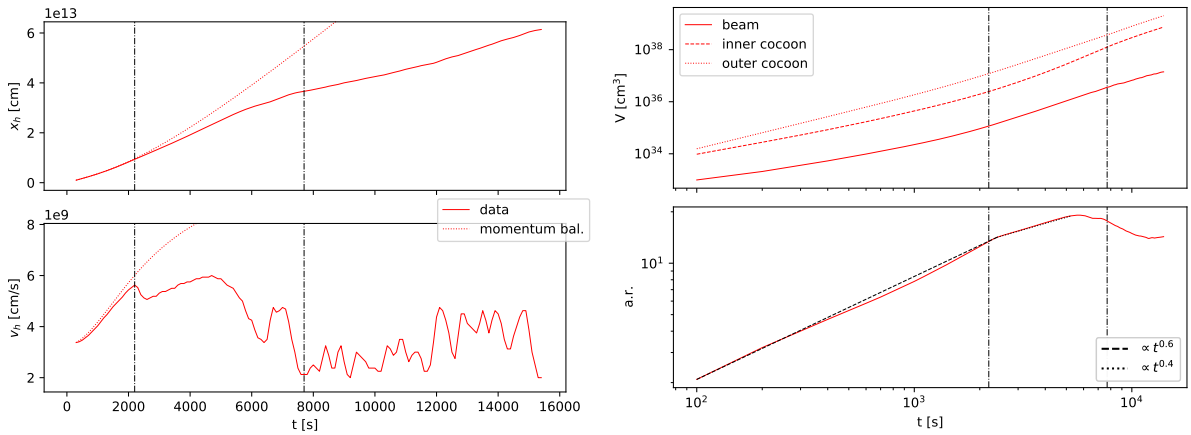

Figure 4.2: **Left:** Position and speed of jet head for fiducial run CygX1. **Right:** jet volume (beam, inner and outer cocoon) and aspect ratio. The limits of each evolutionary phase are marked by the vertical, dash-dotted lines on the various panels.

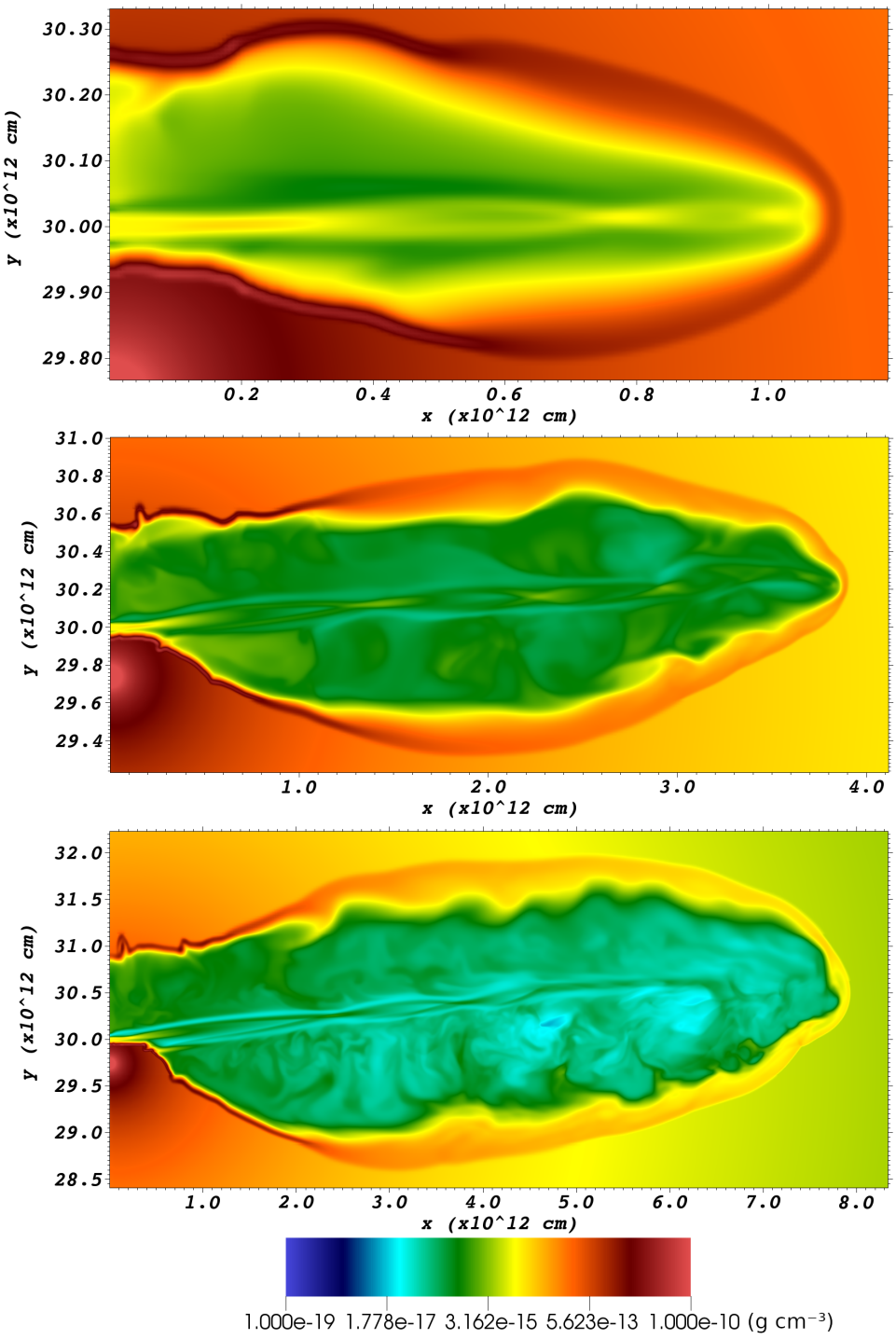

Figure 4.3: Rest-mass density slices of run CygX3 at times (top to bottom) t = 400, 1200 and 2500 s, showcasing the 3 evolutionary phases detailed in the text section 4.1

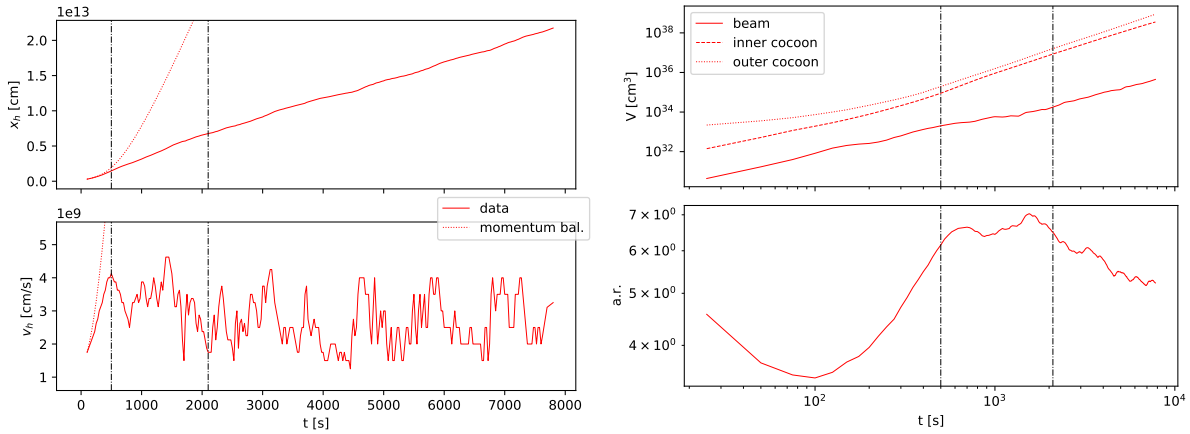

Figure 4.4: **Left:** Position and speed of jet head for fiducial run CygX3. **Right:** jet volume (beam, inner and outer cocoon) and aspect ratio. The limits of each evolutionary phase are marked by the vertical, dash-dotted lines on the various panels.

Instability growth and phases of jet propagation

The structure of our jets goes through three phases, common to both Cygnus X-1 and Cygnus X-3 runs. We refer to these three evolution stages as the *smooth*, *instability growth* and *turbulent* phases respectively according to their inner structure. An illustration via rest-mass density slices is given figures. 4.1 and 4.3. The three phases also leave an imprint on the time series data shown figures. 4.2 and 4.4.

During the first phase, the beam flow is surrounded by a smooth cocoon which is symmetrical at its head. A few internal shocks are present in the beam, starting with a strong recollimation shock situated at a few $\sim 10^{12}$ cm downstream from the injection. Its existence and position are coherent with the criterion and analytical prediction from Yoon et al. (2016) obtained by equating wind ram pressure $p_{ram,w} = \rho_w v_w^2$ and lateral ram pressure in the beam $p_{ram,j} = L_j/(\pi x^2 v_j)$. The aspect ratio of the jet defined in section 3.4 gradually increases. It roughly follows a power law in time in the early propagation phase with an exponent of ~ 0.6. For Cygnus X-3, the aspect ratio in the same phase decreases at first before increasing with what could be a power law of similar exponent to CygX1 case. This may be explained by the strong asymmetry of the cocoon during this phase due to the strong stellar winds. A small deviation of CygX3 beam can already be observed at that point. The jet head position and velocity follows the theoretical 1D result from section 1.1.2. Deviations indicative of the transition from phase one (smooth) to phase two (instability growth) occur after roughly 2000 seconds in the case of CygX1 and much earlier, after a few hundred seconds, in the case of CygX3. In particular, the speed diagram for CygX3 breaks almost immediately from the theoretical profile. This may be a consequence of the already-existing bending of the beam.

In the second phase, instabilities grow in the jet which perturb the flow in both inner cocoon and beam head. While the jet volume tends to grow faster now than during the first phase, the growth of the aspect ratio slows down with a ~ 0.4 exponent for CygX1 case and the jet head velocity overall decreases while the position breaks from the theoretical values. In CygX1, the number of over- and under-pressure regions in the beam (see figures 4.16 and 4.17) stays approximately constant before increasing after

about 5000 seconds. Ultimately, the growing instabilities cause oscillations of the beam head perpendicular to its propagation direction. In CygX3 case, these oscillations induce speed fluctuations even though the beam still retains its structure.

In the last phase, after about 6000 seconds in CygX1 and 2000 seconds in CygX3, the perturbations have reached the beam core. They modify the beam structure at jet head severely, while the inner cocoon has become turbulent. This also marks a change in shape of both the cocoon and jet head. The modification of the jet head shape can be linked to oscillations of the beam region ending in the reverse shock, as a beam head misaligned with general jet propagation direction leads to beam material flowing at higher speed and same direction as the cocoon expansion, deforming it. The jet head position evolves with an approximatively constant mean velocity, with fluctuations up to roughly 30% visible on the speed plots, in line with the persisting motion of the jet head position perpendicular to the jet axis. The volume of the outer cocoon evolves roughly as a power law in time with exponent around three for CygX3 and half as much for CygX1. The volume of the beam features a similar time dependence in the case of CygX1 but a shallower one for CygX3, with a power law exponent rather around two instead of three. The aspect ratio decreases somewhat before becoming constant, at least in the case of CygX1.

This classification can be compared to the one from Bodo et al. (1994) given in section 1.3, but their linear phase escapes our data analysis because we dump data frames only every 100 seconds and 25 seconds for CygX1 and CygX3 respectively, while the estimated KHI linear growth time scale is typically on the order of a few tens of seconds for Cygnus X-1, a few seconds for Cygnus X-3 (see table 4.1). Our first two phases (smooth and instability growth) appear to be subdivisions of their *expansion* phase, while our turbulent and their *mixing* phase match.

run name	t_{KHI} (s)	run name	t_{KHI} (s)
CygX1	71.4	CygX3	0.80
CygX1_noLoss	68.0	CygX3_noLoss	18.4
CygX1_wind	60.8	CygX3_mW	2.7
CygX1_mP	/	CygX3_mP	0.12
CygX1_T7	207.0	CygX3_mPmW	7.1
CygX1_T9	26.8	CygX3_mPmmW	10.0

Table 4.1: Linear growth time of KHI for our different runs, derived from the approach detailed section 1.2.2. No value could be found for run CygX1_mP, where the beam is heavily disrupted by the stellar wind and the approximations made are no longer valid.

These phases are also visible in the speed diagram of jet head displaying the same trend for Cygnus X-1 and Cygnus X-3 fiducial runs in figures 4.2 and 4.4: we can link the smooth phase with the initial acceleration, the deceleration and concave part with the instability growth, followed by the turbulent phase. The first two of these three phases are of interest in the context of dedicated studies on instability onset and growth. Although a large body of associated literature exists, we are not aware of any such studies for relativistic jets in high-mass microquasars including radiative cooling.

The link between the internal structure and the dynamic was discussed in Martí et al. (2016), suggesting that the growth of KHI is related to the strength of these oblique internal shocks inside the beam: KHI grows as the sound wave travels back and forth

between the beam surface and the contact discontinuity, therefore more and stronger internal shocks produce a greater number of reflections within a given time or distance and ultimately accelerate the growth of KHI. The ripple-like structures observed in the cocoon, similar to pressure perturbations in Perucho et al. (2004), could be viewed as markers of such sound waves.

Returning to the density in figures 4.1 and 4.3, although the beam and cocoon mix together at jet head the flow is not slowed down until the very end of the jet. The jets are bent away from the star, almost as soon as the jet establishes for Cygnus X-3 runs but also in Cygnus X-1 runs after enough lifetime of the jet. This bending angle ψ, defined in Yoon & Heinz (2015) as the angle between the local and the initial velocity vector (see section 1.5.1), can be compared to the analytical value found with equation 1.23. For run CygX1, we find $\psi = 0.1$ rad for a beam end at $x = 6.8 \cdot 10^{13}$ cm, which is close to $\psi = 0.09$ found analytically. For CygX3, we find $\psi = 0.04$ rad for a beam end at $x = 1.52 \cdot 10^{13}$ cm and 0.03 analytically, showing good agreement of our runs with the analytical estimate.

Cocoon evolution and radiative losses

Over the course of the initial jet outburst, the outer cocoon expands in the direction perpendicular to the jet propagation due to its overpressure compared to the ambient medium. Upwind and closest to injection, the interface between cocoon and wind is a bow shock and its dynamics is determined at first order by the balance between wind ram pressure and internal thermal pressure of the cocoon: depending on this balance, the interface will move either away or closer to the beam. Further away from the plane of orbit, the wind ram pressure becomes negligible and the interface dynamics is driven by the balance between internal and external thermal pressure. Downwind, the cocoon expands in the same direction as the wind speed. The resulting asymmetry of the cocoon is apparent at early times in both CygX1 and CygX3. At later times, the difference between upwind and downwind diminishes as the wind speed is more and more aligned with the propagation direction of the jet, as shown figures 4.1 and 4.3.

As the cocoon cools down with time, either adiabatically due to expansion and/or from radiative cooling, the thermal pressure of the cocoon diminishes, which will increase the influence of the wind on its dynamics. Figure 4.5 displays the volumic power losses per jet zone per process for fiducial runs CygX1 and CygX3, measured over all the jet cells for two data points per evolutionary phase. In both cases, free-free losses dominate the cooling in beam and inner cocoon, with a stronger cooling in the beam than in the inner cocoon. The colder outer cocoon is dominated by the very efficient line recombination cooling. This result holds true for all our simulated runs.

Also, the gas in the cocoon has a velocity component in the positive x-direction. Thus the cocoon moves outward of the system with the beam, albeit at a slower pace. Ultimately, no trace of the original cocoon is left in the innermost parts of the jet. A thin interface of shocked stellar wind only a few r_b wide has formed instead between the wind and the beam (late times in figures 4.1 and 4.3). This "naked beam" is of interest as it represents a (quasi) stationary state structure studied in the literature (e.g. Wilson 1987; Komissarov et al. 2015 for hydrodynamical jets, Martí et al. 2016; Bodo & Tavecchio 2018 for MHD jets) and can be related to direct observations.

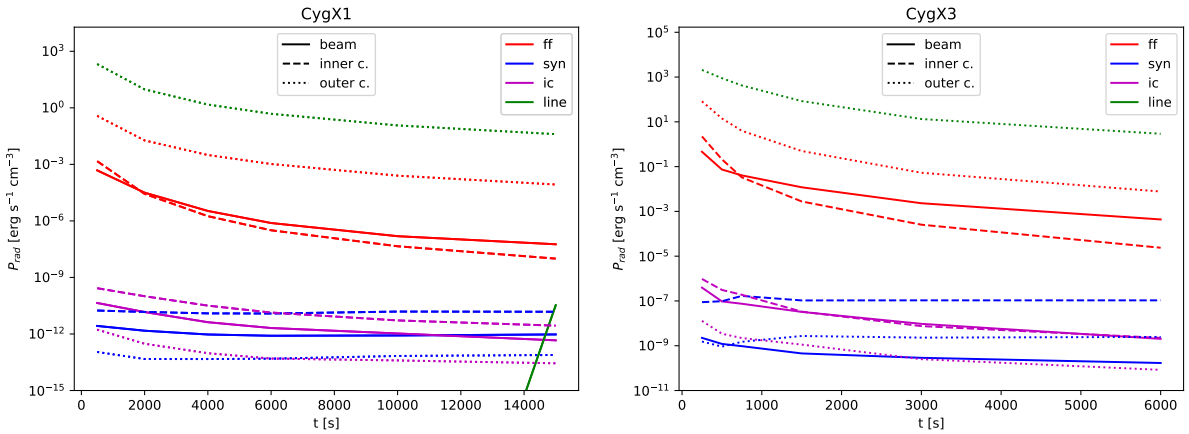

Figure 4.5: Time evolution of radiative losses for fiducial runs CygX1 (left) and CygX3 right), derived at each cell and summed per zone, at timesteps t = (500, 2000, 4000, 6000, 10000, 15000) s for CygX1 and t = (250, 500, 750, 1500, 3000, 6000) s for CygX3 (two data points per evolutionary phase). In both cases, free-free losses dominates cooling in the inner cocoon and beam while line cooling dominates the outer cocoon.

4.2 Effects of losses on jet structure and dynamics

Cooling times in our two fiducial cases are such that over the time covered by our simulations, radiative losses have no significant impact on CygX1 as shown figure 4.6. Even the jet head velocity evolves remarkably similar with and without radiative losses during the first two phases of jet evolution (figure 4.6, right panel). In the case of CygX3, by contrast, radiative losses lead to a loss of much of the outer cocoon on distances of a few 10^{12} cm as visible on the temperature slices figure 4.7 left panel, and slow down the jet head (figure 4.7, right panel). Therefore, we restrict the following discussion mostly to CygX3.

4.2.1 Beam destabilising effect through cocoon pressure

The addition of the loss terms has a destabilising effect on the beam through its interaction with the inner cocoon: free-free cooling, shown figure 4.5 to be the dominant process in both the beam and the inner cocoon, diminishes pressure in the jet with a different intensity depending on jet zone: the beam cools faster than the inner cocoon, causing a stronger pressure gradient between inner cocoon and beam. This strengthens the oblique internal shocks (figure 4.8, left panels), which in turn accelerates the growth of KHI as detailed section 4.1. Thus KHI grows faster in the cooled case, changing the dynamical behavior of the cooled jet as seen figure 4.7. Pressure in each zone is derived from the mean rest mass density and temperature measured over the corresponding marked cells defined section 3.4.

The cocoon-to-beam pressure ratio for runs CygX3 and CygX3_noLoss is shown top panel of figure 4.8. It is to be noted that this ratio is greater than 1 at all time, ensuring a pressure collimation of the beam. In the non-cooled case, after the initial decrease due to the jet structure settling in, the overpressure grows in two phases with a transition around $\sim$ 2000 s. In the cooled case, the growth rate seems constant from the start with

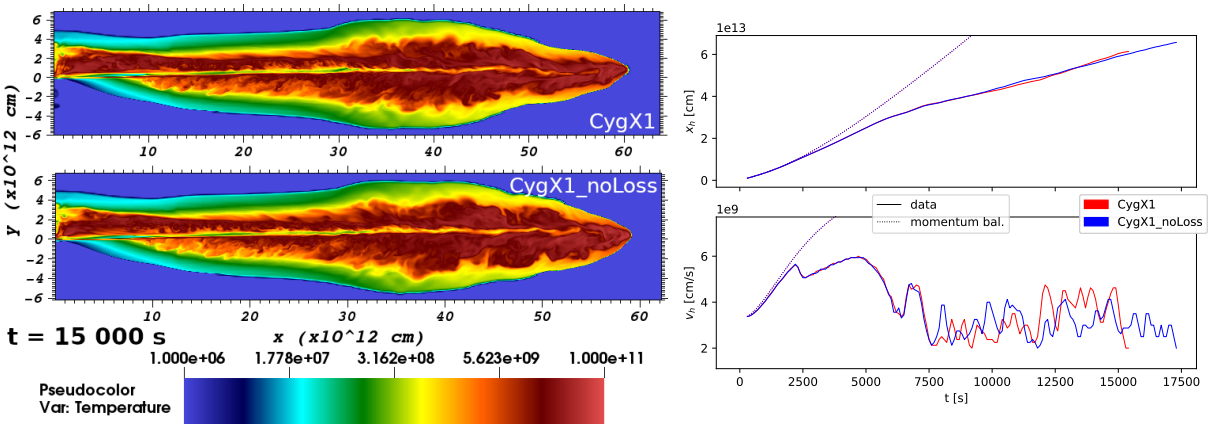

Figure 4.6: Effects of losses on CygX1 structure and dynamical properties.
Left: Temperature slices of runs CygX1 and CygX1_noLoss at time t = 15 000 s. Both jets display similar structures, with the exception of a slightly larger outer cocoon at the head of the non-cooled jet. **Right:** jet head propagation and speed of the same runs, CygX1 in red and CygX1_noLoss in blue, theoretical 1D propagation (equation 1.11 from section 1.1.2) is drawn in dotted lines following the same color coding. The propagation is identical between both runs until the start of the turbulent phase, after which speed fluctuations differ but the average propagation speed is identical between the two runs with almost no difference in the jet head position plot.

the exception of a strong increase starting at t = 650 s, peaking at $\sim$ 1000 s and joining the overall trend at 1350 s. This happens as the jet transitions from the instability growth to the turbulent phase: t = 600 s indeed marks the apparition of strong oblique shocks in the cooled case. This stronger overpressure explains the difference in beam structure that can be seen in the bottom panel of figure 4.8 displaying longitudinal slice of the jet material tracer at t = 750 s including the plane containing the star center: a higher inner cocoon to beam pressure gradient causes the stronger oblique shocks in CygX3 runs.

4.2.2 Effects on outer cocoon expansion

Volumes of individual jet zones are affected by radiative cooling in different ways (figure 4.9). As detailed in section 4.1, the dynamics of the wind-cocoon interface near the injection zone is mostly controlled by the inner thermal pressure of the outer cocoon. Therefore, the more efficient the cooling, the smaller the outer cocoon and the faster the evolution of the cocoon up to the "naked beam" situation. In Cygnus X-3 case, the effect on the cocoon can be seen on the volume diagram figure 4.9: very quickly, the outer cocoon evolves to be consistently of greater volume in the non-cooled case. On the contrary, the volume of both inner cocoons are similar in the smooth and turbulent phases: in the former, the cooling effects on the inner cocoon are negligible as it is both the hottest and least dense part of the jet, while in the latter phase the instability-induced turbulence dominates the cocoon flow. The period during which the volume of the inner cocoon differs is likely due to the different starting time of the mixing phase between those runs, as explained in section 4.2.1.

Once the turbulent phase is reached, both inner and outer cocoon volume show a

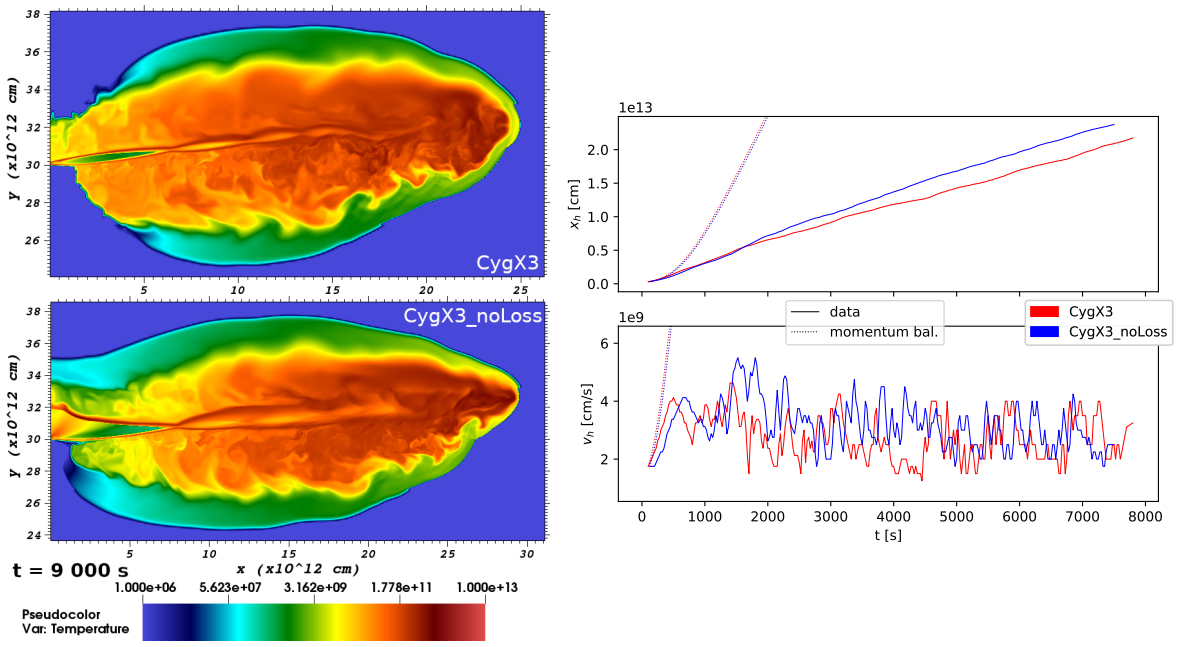

Figure 4.7: Effects of losses on CygX3 structure and dynamical properties.
Left: Temperature slices of runs CygX3 and CygX3_noLoss at time t = 9 000 s. Two main differences appear: 1) the cooled beam is thinner with its envelope following closely the internal shocks structure in contrast to the non-cooled case 2) the cocoon of the non cooled jet expands further at its basis, almost wrapping around the star, whereas in the cooled case the cocoon has almost disappeared because ambient material has cooled enough to be blown back by the wind. **Right:** same as figure 4.6. The cooled jet (in red) is initially faster but leaves the smooth phase earlier, after which point it is slower in average as seen on the propagation plot.

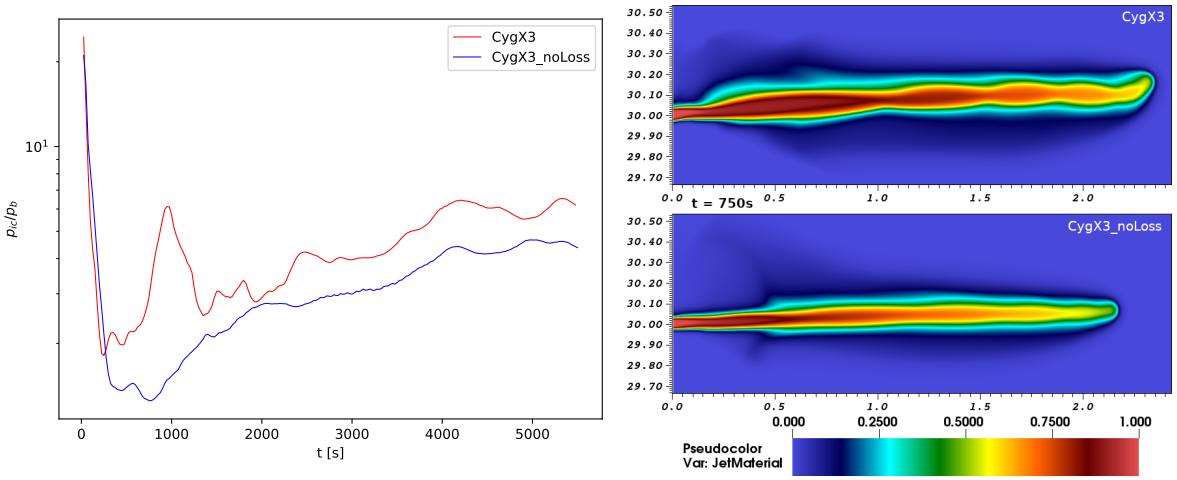

Figure 4.8: Effects of radiative losses on CygX3 beam structure.
Left: Ratio of volume-averaged pressure between inner cocoon and beam for runs CygX3 (red) and CygX3_noLoss (blue). The overpressure is always greater in the cooled case **Right:** Tracer density at t = 750 s for runs CygX3 and CygX3_noLoss. The cooled jet features stronger oblique shocks.

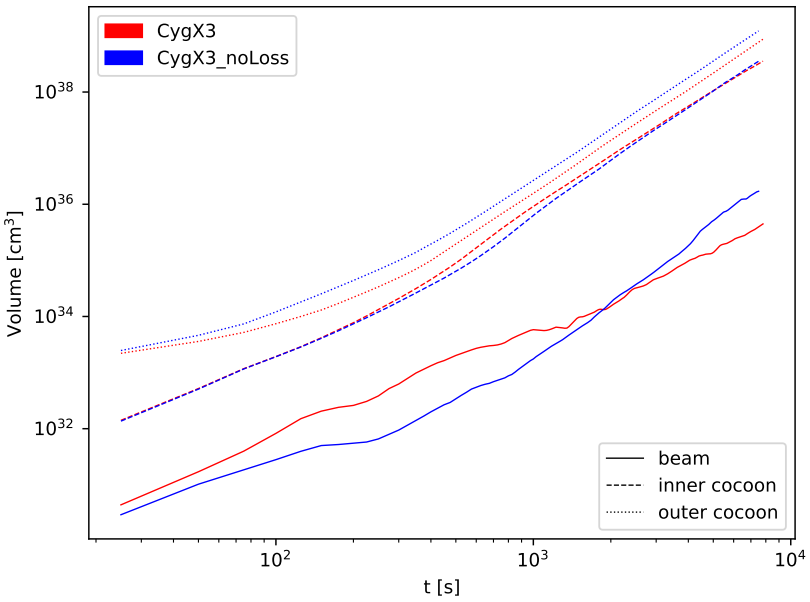

Figure 4.9: Effects of radiative losses on CygX3 zones.
The volumes of the different jet zones as a function of time are affected differently by radiative cooling. The outer cocoon is bigger without losses, while volumes are comparable for the inner cocoon. The power-law dependence on time of the cocoon is robust for the cocoon but not for the beam.

similar power law dependence on time of roughly t^3, independent of whether or not radiative losses are included. By contrast, the beam volume displays a different power law dependence in the cooling and non-cooling case. The relative volume of outer to inner cocoon is much larger in the no-loss case than in the loss case. This may be an issue if radiative losses are diagnosed only during post-processing from adiabatic solutions.

The cocoon form is also affected: comparing runs CygX3 and CygX3_noLoss top of figure 4.7, the expansion is strong enough in the non-cooled case to make the cocoon almost wrap around the star before being blown back as the cocoon pressure diminishes, while in the cooled case the cocoon is almost immediately blown back to a thin shell by the strong stellar winds.

4.3 Parameter sensitivities

We start section 4.3.1 by investigating sensitivities to the assumed beam temperature, which gets comparatively little coverage in the literature and is thus somewhat more extensively dealt with here. Sensitivities to beam power and wind parameters follow sections 4.3.2 and 4.3.3, respectively.

4.3.1 Effects of jet temperature on instabilities growth

Raising the jet injection temperature T_j lowers the beam Mach number, we expect the jet to display a smaller cocoon and to be less stable as the distance between internal shocks in

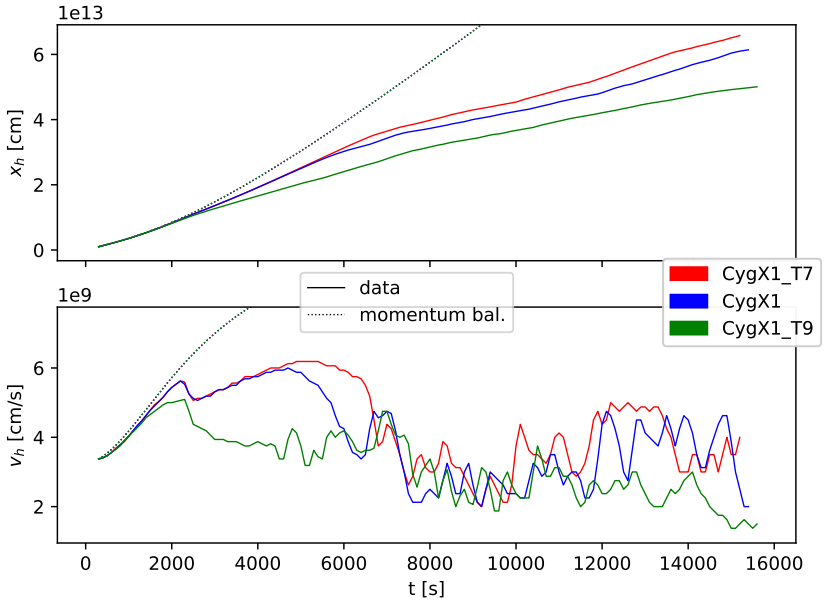

Figure 4.10: Jet head propagation and speed for runs CygX1_T7 (red), CygX1 (blue) and CygX1_T9. Run CygX1 slows down to turbulent phase earlier than CygX1_T7, but display the same average speed during turbulent phase as seen from the close-to-parallel propagation curves. Run CygX1_T9 displays a different behaviour, decelerating to a plateau in the instability growth phase and with lower average speed than the other two runs, seemingly decelerating after t = 12 000 s.

the beam diminishes with it. This is true when going from 10^8 to 10^9 K, but not from 10^7 to 10^8 K. We ascribe this difference to the action of the first recollimation shock, which heats up the beam of CygX1_T7 to similar values of those found in CygX1. Increasing T_j also results in a greater over-pressure between the inner cocoon and the beam, further strengthening the aforementioned effects of oblique shocks, leading to faster destabilisation of the beam as explained in section 4.1.

This destabilisation is visible in the speed diagrams figure 4.10, showing colder jets to be more stable than hot jets: CygX1_T7 shows similar dynamics as the fiducial run with a longer instability growth phase. On the contrary, the run CygX1_T9 displays different dynamics in this phase as the other two: the jet propagation speed slows down to a plateau instead of exhibiting a progressive acceleration. This difference in dynamical regime can be linked to the mean beam temperature top panel of figure 4.11: beams associated to runs with $T_j = 10^7$ and 10^8 K almost display the same temperature due to the heating at the initial recollimation shock which raises them to a few 10^9 K with very little differences. They begin to deviate from each other around the same time as the jet propagation speed does. With $T_j = 10^9$ K the temperature upstream of the shock is of the same order of the downstream one, resulting in an higher effective beam temperature meaning internal shocks that are closer to each other. This observation is confirmed by drawing the probability density function (PDF) of temperature figure 4.12, representing the volume fraction of the jet which is at a given temperature. At t = 4000 s (full lines, during instability growth phase), the PDF for CygX1 and CygX1_T7 are identical while CygX1_T9 differs for temperatures over $\sim 4 \cdot 10^9$ K. At t = 10 000 s the PDF of the

three runs differ by roughly the same amount, especially at the peak around $2 \cdot 10^{10}$ K. This can be interpreted as the turbulence in the cocoon distributing the available thermal energy and therefore making the difference in injected temperature visible.

Bottom panel of figure 4.11 shows the pressure ratio between inner cocoon and beam for the same three runs, where the pressure is derived from the mean temperature and rest mass density obtained by averaging over the marked cells. The pressure ratio in run CygX1_T9 displays a different behaviour as the other two runs, showing higher values as soon as t = 1000 s, resulting in stronger internal shocks in the beam, while the values for runs CygX1_T8 and T7 are similar up to time t $\sim$ 6000 s, meaning the internal structure of those two jets are similar during that period. These two effects both accelerate the growth of KHI modes, which is confirmed by the derived values of t_{KHI} of 207, 71.4 and 26.8 s found in table 4.1 for runs CygX1_T7, CygX1, and CygX1_T9 respectively.

Turning from the early beam evolution and instability growth to the turbulent phase, we find much less effect of the different beam temperatures. The velocity of the jet head is comparable to within its fluctuation range, except for possibly the very late time still covered by our simulations when the jet head velocity for the hottest jet seems to slow down slightly as compared to the two simulations with cooler jets. This would suggest that as soon as a more generic, turbulent behaviour takes over the dynamics, the importance of beam injection temperature lessens.

4.3.2 Effects of injected power

Lowering the jet kinetic power lowers its propagation efficiency as well as its stability. Starting from our fiducial test cases CygX1 and CygX3, we reduced the jet power by a factor of 10 (CygX1_mP) and 2 (CygX3_mP) via reduction of the jet density at constant beam speed, as detailed in table 3.4 section 3.3. In these modified settings, the jets are expected to propagate slower and to be more prone to instabilities due to a smaller inertial mass density as long as the jet isn't disrupted by the stellar wind as pointed out in Perucho et al. (2010). This disruption happens for run CygX1_mP as visible figure 4.14. At constant beam speed v_b, the amplitude of speed variations along the trend defined in the beginning of this section and the timescales at which they occur are controlled by the injected kinetic power but the trend itself is not affected.

Figure 4.13 shows propagation plots for runs CygX1 (red) and CygX1_mP (blue), with the same parameters except for ρ_j which is 10 times smaller in the latter case. The weak jet displays a different behaviour as the beam is strongly bent away by the wind and then broken down by instabilities after t = 8000 s, as visible in red figure 4.14 drawn at t = 10 000 s. The beam mixes with the cocoon further away from the contact discontinuity and the momentum flowing from the reverse shock at beam head is partly dissipated in the cocoon. This smoothes the effects of beam head oscillations on the jet head dynamics as well as slowing down the jet propagation.

The propagation of runs CygX3 and CygX3_mP is shown left of figure 4.15, ρ_j is here divided by 2 between the two runs. We chose to divide by 2 and not by 10 as in Cygnus X-1 runs due to the much stronger impact of the wind on the jet in Cygnus X-3 case since the orbital distance is smaller by a factor of 10. In this case, the same remark about the shape of the speed plot holds: weaker jets show a similar evolution with smaller amplitudes in the global variations of jet velocity. But, contrary to the Cygnus X-1 case, a

diminution of the density destabilises the jet: the first speed peak which occurs when the jet propagation breaks from the momentum balance model happens earlier in the weak case, as well as the beginning of the speed fluctuations.

4.3.3 Wind effects on jet propagation

Increasing wind ram pressure shortens the instability growth phase, showing a link between this deceleration and the wind impact on the beam. In Cygnus X-1 runs, the impact of a 50% higher stellar wind speed and therefore 50% increase in wind ram pressure at constant mass loss rate $\dot{M}_\star$ is shown figure 4.13 by comparing CygX1 (red) and CygX1_wind (green) runs: the stronger the wind speed, the shorter the instability growth phase. The beginning of this phase also happens to start a bit earlier: at 1800 s for CygX1_wind versus 2200 s in the fiducial case. One must also note that the ambient density drops a bit from CygX1 to CygX1_wind since $\dot{M}_\star$ is constant between the two runs, meaning higher η and therefore easier jet propagation through the medium, explaining the difference in starting propagation speed between the two runs. Theoretical 1D estimates for position and speed strays from the measured values earlier in the strong wind case as multidimensional effects are stronger. Increasing the wind speed induces a small plateau in jet speed at the very beginning of its propagation, which cannot be modeled by our 1D theoretical estimate.

For Cygnus X-3 runs, right panel of figure 4.15 compares the fiducial run CygX3 (red) with run CygX3_mW (blue) where the wind is slower, all other parameters kept constant with the exception of massloss rate to ensure same η value between the runs and halving the wind ram pressure on the jet, while the right panel shows this same modification using the weaker jet setup (runs CygX3_mP and CygX3_mPmW). In the first case, the initial accelerating phase is twice as long for run CygX3_mW than run CygX3, and the second phase in run CygX3_mW consists only of a global deceleration as no reacceleration is observable. After this deceleration, run CygX3_mW shows a slightly higher median propagation speed.

When comparing runs CygX3_mP and CygX3_mPmW on the bottom right of figure 4.15, a new effect arises: instead of a deceleration, the initial acceleration phase of run CygX3_mPmW is followed by a plateau. The velocity fluctuations around the trend also appear later but with a greater amplitude when the wind is weaker. After this speed plateau, the jet decelerates to a median value similar to the strong wind case, while the speed fluctuation timescale also diminishes to a similar value as the strong wind case. This happens after $t \sim 3000$ s, when the jet has propagated to a distance of $\sim 5\,10^{12}$ cm ($= 20\ d_{orb}$). At this point, the wind is almost colinear with the jet propagation and its lateral ram pressure on the jet is negligible.

Bibliography

Bodo G., Tavecchio F., 2018, A&A, 609, A122

Bodo G., Massaglia S., Ferrari A., Trussoni E., 1994, Astronomy and Astrophysics, 283, 655

Komissarov S. S., Porth O., Lyutikov M., 2015, Computational astrophysics and cosmology, 2, 1

Martí J. M., Perucho M., Gómez J. L., 2016, APJ, 831, 163
Perucho M., Hanasz M., Marti J.-M., Sol H., 2004, Astronomy & Astrophysics, 427, 415
Perucho M., Bosch-Ramon V., Khangulyan D., 2010, Astronomy & Astrophysics, 512, L4
Wilson M., 1987, Monthly Notices of the Royal Astronomical Society, 226, 447
Yoon D., Heinz S., 2015, The Astrophysical Journal, 801, 55
Yoon D., Zdziarski A. A., Heinz S., 2016, Monthly Notices of the Royal Astronomical Society, 456, 3638

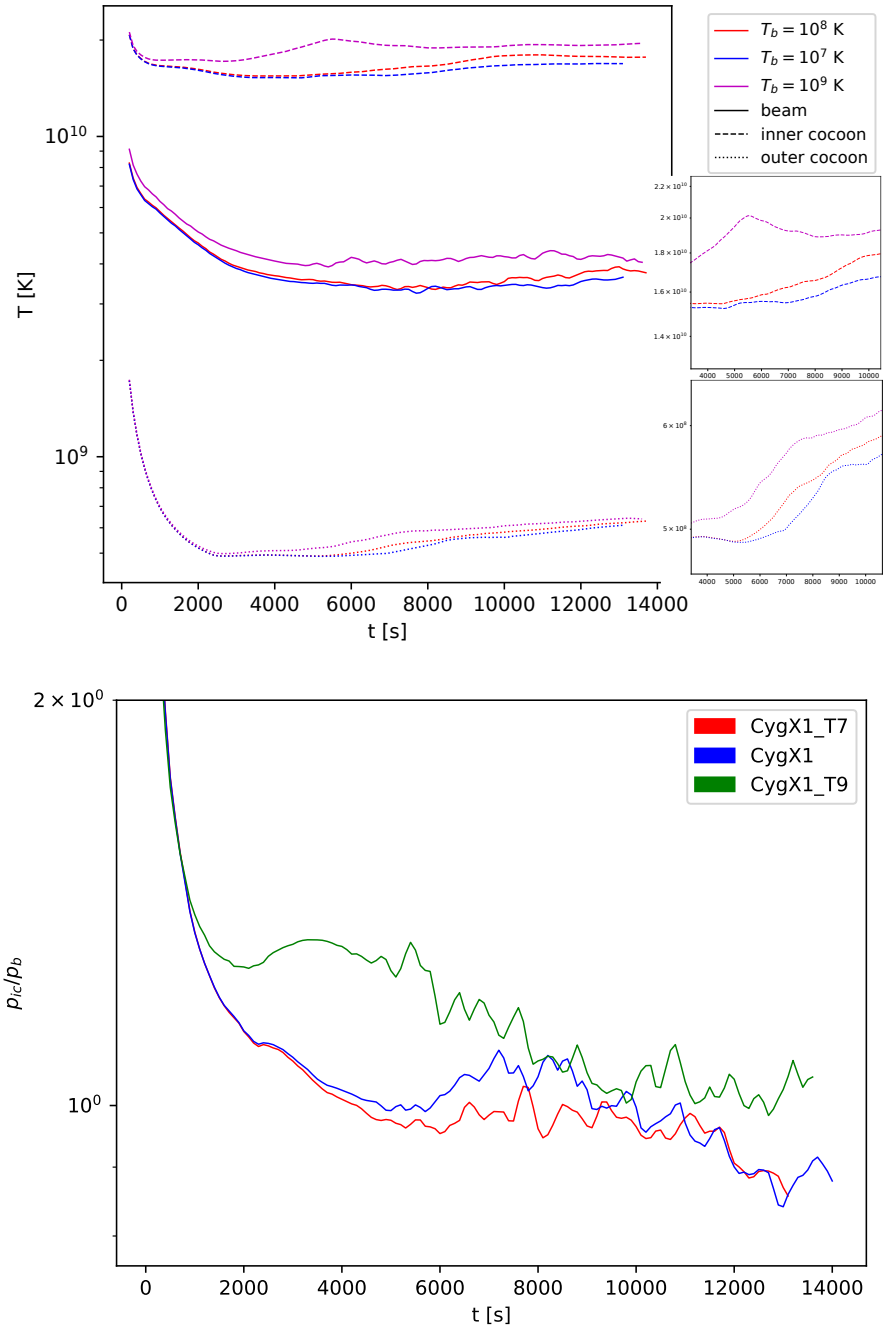

Figure 4.11: Comparison of temperature and overpressure of runs CygX1_T7, CygX1 and CygX1_T9, the color coding is the same as in figure 4.10. **Top:** Evolution of the zone-averaged temperature with simulation time. CygX1 and CygX1_T7 differ only slightly at first then start evolving differently after the 5000 s mark. CygX1_T9 shows an overall higher temperature, with a small peak in inner cocoon temperature around t=6000 s. **Bottom:** Evolution of the inner cocoon to beam pressure ratio as defined section 4.2.1. CygX1 and CygX1_T7 present similar values up to t $\sim$ 5 000 s, while CygX1_T9 presents a stronger overpressure.

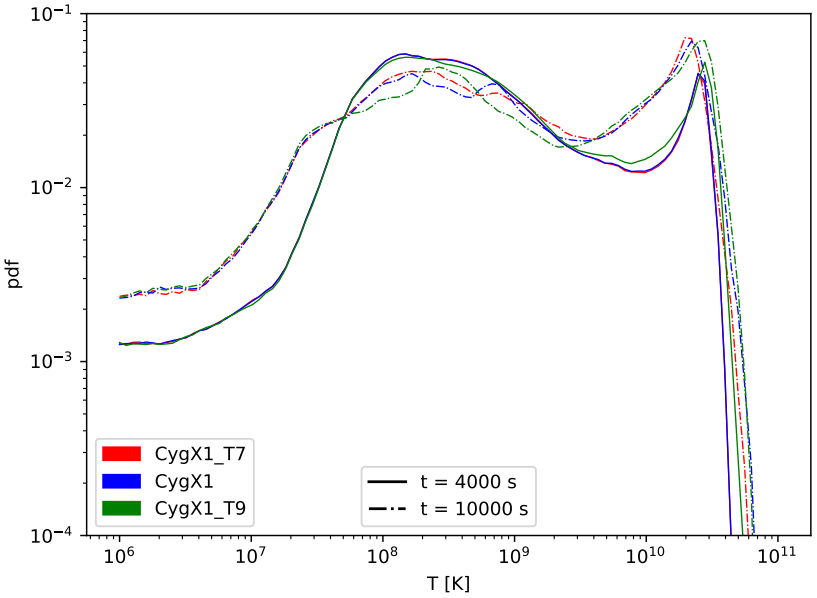

Figure 4.12: Comparison between runs CygX1 (red), CygX1_T7 (blue) and CygX1_T9 (magenta). Probability density function of temperature at t = 4000 s (full lines) and t = 10 000 s (dash-dotted lines). In early stages, CygX1 and CygX1_T7 are indistinguishable from each other while CygX1_T9 is a bit hotter with more of its volume over $\sim 5 \cdot 10^9$ K. In the mixing phase, the temperature repartition is more in line with the injected temperature.

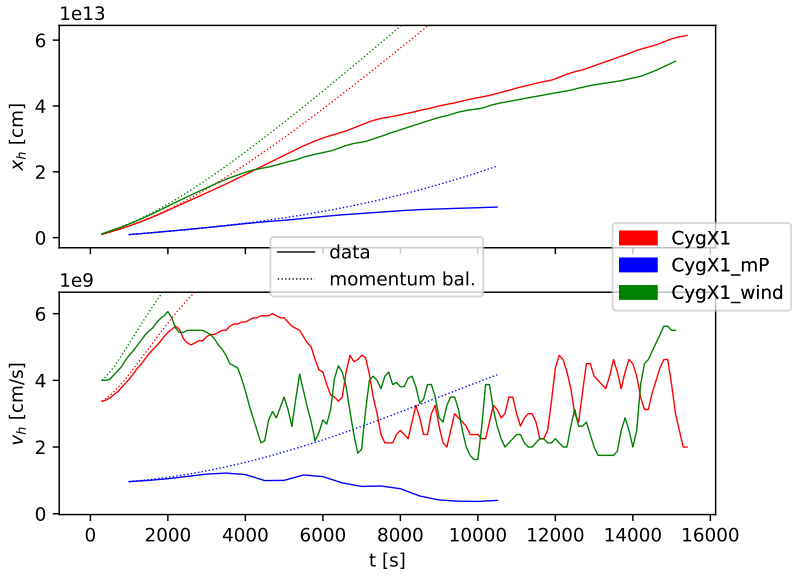

Figure 4.13: Sensitivity of jet head position and speed to kinetic power and wind ram pressure for Cygnus X-1. Jet kinetic power is divided by 10 from CygX1 (red) to CygX1_mP (blue). In the weak case the jet is slower, but the position fits the theoretical evaluation for a longer time. The speed diagram shows no oscillations. Wind speed is increased by 50% for run CygX1_wind (green), which results in a higher starting speed, a shortening of the reacceleration phase and a weakening of the bump in the 2nd deceleration phase. The average speed in the turbulent phase is weaker. Both speed and position plot strays from theoretical 1D values faster in the strong wind case.

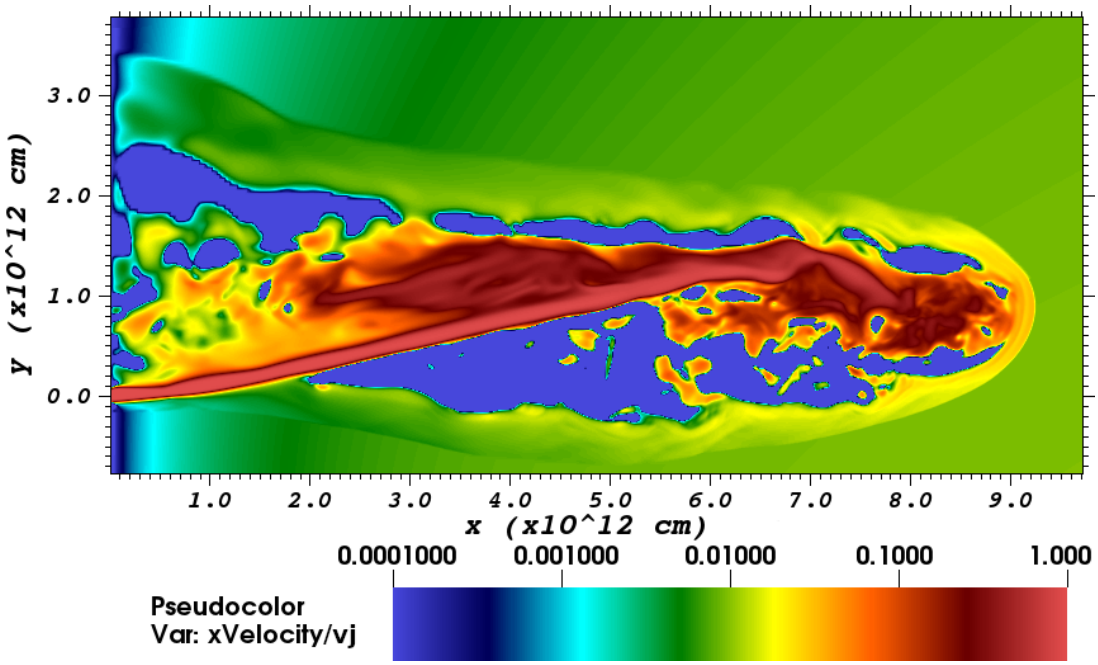

Figure 4.14: v_x/v_j slice for run CygX1_mP at time t = 10 000 s. The jet has been heavily bent from the wind effects and its velocity breaks down before arriving at the head.

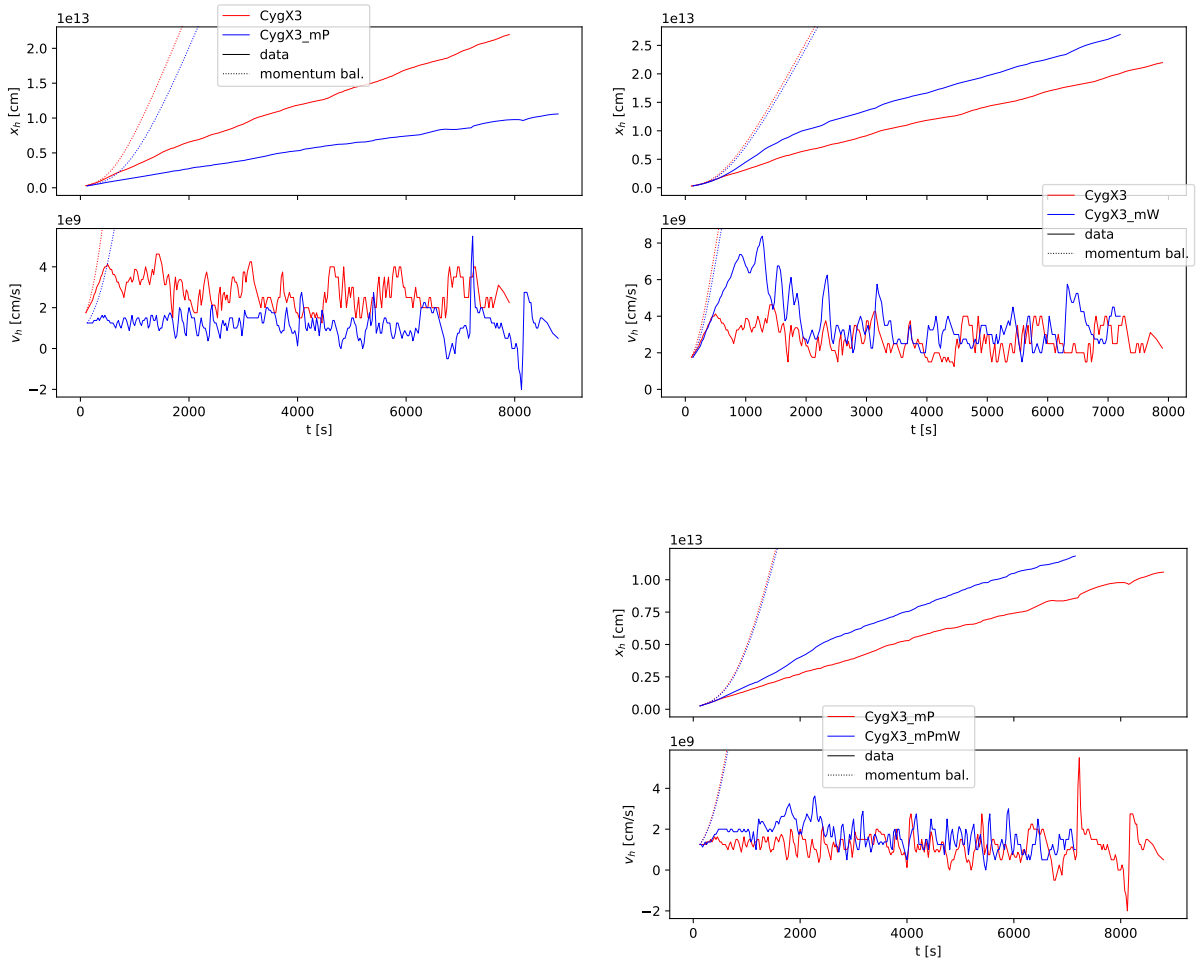

Figure 4.15: Sensitivity of jet head position and speed to kinetic power (left) and wind momentum (right) for Cygnus X-3 runs. Top left: Dividing jet power by 2 lowers all dynamical values, starting from the mean propagation speed. In particular, the acceleration is far less efficient: it shows a gain of $\sim 40\%$ in speed between the starting point and the peak against a gain of $\sim 120\%$ in the CygX3 run. Top right: reducing $\dot{M}_\star$ by 25% and v_w by 33% (keeping η constant) lengthens the smooth phase and strengthens the speed fluctuations in the following phases. Jets settle to the same median speed in the turbulent phase. Bottom right: same reduction as in the former with halved jet power. In CygX3_mPmW case (right, blue), the initial acceleration phase is followed by a speed plateau.

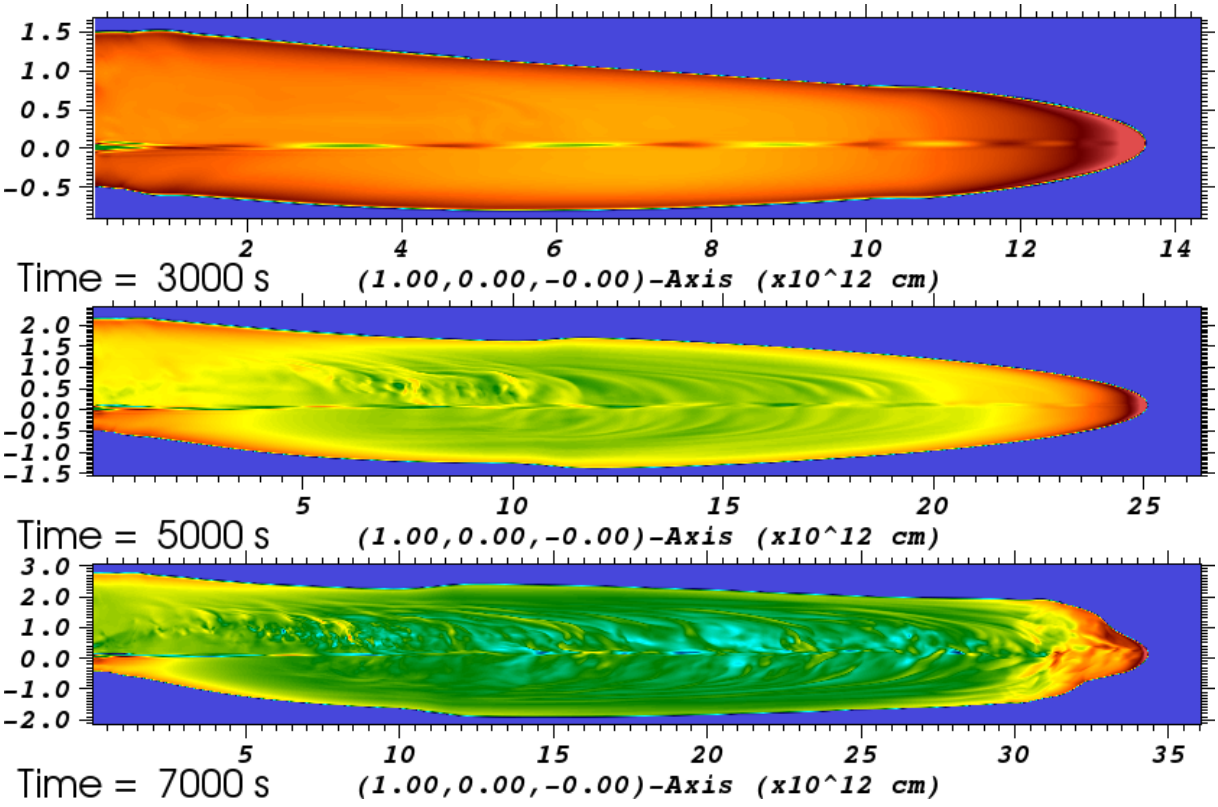

Figure 4.16: Pressure slices during instability growth phase of fiducial Cygnus X-1 run CygX1. Color scale is fixed from 1 (blue) to 1000 Ba (red) to better highlight the beam structure. The beam shows an alternance of over- and underpressured zones whose number has risen at the 5000 s mark. The inner cocoon shows ripple-like structures alternating on both sides of the beam with increasing intensity as the jet evolves.

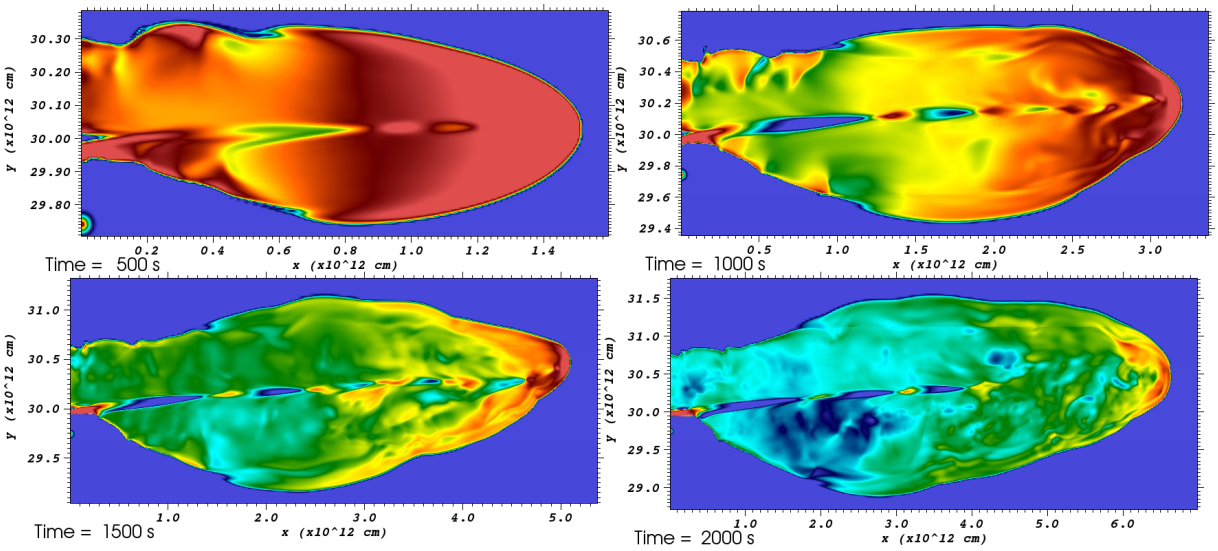

Figure 4.17: Pressure slices during instability growth phase of fiducial Cygnus X-3 run CygX3. Color scale is fixed from 10^3 (blue) to 10^5 Ba (red) to better highlight the beam structure.

Chapter 5

Conclusion

5.1 Summary

In the course of this PhD thesis I developed analytical formulas for the cooling of an astrophysical plasma, as well as numerical tools aiming to precisely analyse and quantify simulated relativistic hydrodynamical jets. These tools were then used to study the impact of including the aforementioned cooling in state-of-the-art numerical simulations of hydrodynamical, relativistic jets over a large spatial and temporal scale. The context of this thesis is presented in the Introduction, introducing microquasars as complex astrophysical objects where various physical phenomenon are at play. More details on the microquasars Cygnus X-1 and Cygnus X-3, which were (tentatively) reproduced for this PhD, are also given. We then focused on the component which was the focus of this PhD: the relativistic jets, from their genesis to the studies of their evolution in interaction with the rest of the system, mainly the stellar winds from companion star.

By the end of this introduction, we saw a lack of numerical simulations that are both relativistic (Perucho & Bosch-Ramon, 2008; Perucho et al., 2010b,a; Perucho & Bosch-Ramon, 2012) and large-scale (Yoon & Heinz, 2015; Yoon et al., 2016), justifying the present work. Such relativistic jets being visible in radio bands (Mirabel & Rodriguez, 1994; Gallo et al., 2005; Martí et al., 2001) from synchrotron and free-free radiation, we also added these radiative processes, as well as inverse Compton scattering and line recombination, as an energy loss term into the equations of special relativistic hydrodynamics to investigate whether these radiative processes have an impact on the jet over such scales.

In chapter 1, I presented our current knowledge on the physics of hydrodynamical relativistic jets, beginning with the studies of AGN jets on which microquasar jet studies are based on. From the equations of special relativistic hydrodynamics (Mihalas & Mihalas, 2013), we delved into the development of hydrodynamical instabilities in relativistic jets. This section focused on the onset of the Kelvin-Helmholtz instability, as this instability was identified as the driving mechanism behind the internal structure of the jet (Bodo et al., 1994; Perucho et al., 2004a,b), its growth determining the evolutionary stages that a relativistic jet will go through in its propagation. This picture is then completed by a few words on the observed MHD effects on relativistic jets as well as the previous studies that focused on the evolution of relativistic jets in the context of a microquasar (see the

works from Perucho et al. and Yoon et al. cited in previous paragraph).

The derivation of the volumic losses which were added in the A-MaZe toolkit (free-free, synchrotron and inverse Compton emission) are then presented in the first part of chapter 2, as well as line cooling when electrons recombinate with ions at low temperatures. To obtain the energy radiated by a thermal plasma, we integrated the energy lost per electron for each process with the relativistic Maxwell-Jüttner distribution for electrons, as the temperatures reached in our model jets are high enough for the electrons to adopt a (mildly) relativistic behaviour. The emission coefficients corresponding to the same processes are presented in a second part of the chapter.

The numerical methods used to perform this work are presented chapter 3. The A-MaZe toolkit (Walder & Folini, 2000) used to perform the numerical study of relativistic jets is described, with an emphasis on the relativistic solver implemented for this work and the related numerical benchmarks. Given the sheer size of such simulations (a simulation snapshot represents $\sim$ 15 GB of data, a run with a given set of parameters is several TB), an efficient data processing method is necessary. The code behind those methods is presented in the second part of the chapter 3. Lastly, we present a numerical method to obtain a spectral signature of our simulated jets using the emission coefficients derived in the second part of chapter 2.

The impact of the loss term on the structure and dynamics of the jets is thus investigated in chapter 4. In particular, adding radiative losses induced a differential cooling between the jet beam and the surrounding cocoon. This differential cooling strengthens the overpressure of the latter over the former, which in turn accelerates the growth of the Kelvin-Helmholtz instability and destabilises the jet (Martí et al., 2016), impacting its structure and dynamics.

A parametric study around the parameters chosen to reproduce Cygnus X-1 (Orosz et al., 2011) and Cygnus X-3 (Zdziarski et al., 2013) makes the last part of chapter 4. Results from previous studies such as jet bending and jet disruption by the stellar wind are confirmed, and the impact of the jet temperature on its stability and dynamics was investigated. A threshold effect is found: when the injected temperature is greater than the temperature to which the first recollimation shock would heat injected material of this density and velocity, the instability growth results in sensibly different dynamical properties of the jet.

5.2 Perspectives

While we successfully investigated the impact of thermal, optically thin radiative losses on the evolution of microquasar jets, there is several ways to push this study further. We discuss here the limitations of this study and present the corresponding ideas that may be developed in future works to push past those limits.

5.2.1 Jet zones diagnostics and equation of state

Firstly, the post-processing methods present room for improvement. The core of the actual method resides in discriminating simulation cells between the three jet zones and the ambient medium, but this zone identification could be made more precise. The importance of the hotspot between the reverse shock and the contact discontinuity at jet head has

been emphasised in various works such as Scheck et al. (2002) as they are a source of non-thermal emission and particle acceleration. Including the detection of this zone in the algorithm would allow us to access more precise data to compare with existing works.

Other diagnostics may also be added to paint a better picture of our simulated jets. Capturing the geometry of each zone would allow for a more quantitative study of the wind effects on the jet structure: measuring the jet thickness would give more ways to compare our simulations to those of Yoon & Heinz (2015) and a measure of the jet-cocoon mixing would allow automatic estimates to discriminate between the instability growth and turbulent phases identified in this work, comparable to the criterion used in Perucho et al. (2004b). The oscillations in the propagation speed could be further analysed to find relevant frequencies, which may be linked to the dominant modes of KHI. Finally, a characterisation of the turbulent flow in the cocoon has never been done to my knowledge and may be of interest to develop emission models.

We discussed in section 1.3 the importance of the adiabatic index in the jet structure. While we used an adiabatic EoS with constant index $\Gamma = 5/3$, this can be refined. Some studies keep the adiabatic EoS and inversion method and update from a constant to a variable index as suggested by Mignone & McKinney (2007). Another way would be to directly use the theory of relativistic gases (Synge, 1957), which shows the specific enthalpy to be a function of the temperature Θ alone:

$$h = \frac{K_3(1/\Theta)}{K_2(1/\Theta)}, \tag{5.1}$$

term which is already computed in A-MaZe to derive the radiative losses due to synchrotron emission and inverse Compton scattering. A realistic EoS can therefore be included in A-MaZe without adding much to the calculation time. It would nonetheless require an updated method to recover primitive variables such as described in Appendix A in Mignone & McKinney (2007).

5.2.2 Instabilities, shocks, and mesh resolution

The dynamics of the second (instability growth) phase are not well understood yet, as well as the physical phenomenon setting fluctuation in propagation speed. The physics of instability growth is deep and rich, and we may have overlooked some effects concerning the non-linear phase especially. The study of instability growth is also linked to the grid resolution: as discussed in section 1.2, some instability modes cannot grow in our simulations due to resolution limitations. The shocks and interfaces whose impact has been highlighted during this work also require a fine mesh to be correctly resolved (see the discussion section 3.2). Simulations using the full capacity of the AMR methods implemented in A-MaZe would allow to solve this issue at least partly, but at the cost of more computational resources.

Accompanying this increase in resolution, an implementation of shock detection methods (e.g. Dubois et al., 2019) in the post-processing code would serve as basis for various diagnostics, especially towards improving the spectral signature of jets as shocks are a potential source for high-energy emission. This implementation was attempted but was deemed too computationally-heavy for a single-processor Python code. Upgrading the post-processing methods with parallel computing, and even rewriting the code in a more

performance-oriented language such as C/C++ would significantly improve the analysis of such heavy simulation snapshots, deemed to become even heavier in the case of runs using AMR.

5.2.3 Jet bending and wind structure

The bending of the jet away from the mass-shedding donor star due to the combined effects of the wind and orbital motion, investigated in e.g. Perucho & Bosch-Ramon (2008) and subsequent papers, Yoon & Heinz (2015), Bosch-Ramon & Barkov (2016), and again confirmed in this paper, will lead to helical jet trajectories. In the most extreme cases, an observer will see the jet under different angles during an orbit of the system (see e.g. Horton et al., 2020). Future works will lead to a more quantitative statement of this prediction. Moreover, the jets are injected with no inclination relative to the orbital plane, contrary to works such as Dubus et al. (2010) suggesting the inclination angle for Cygnus X-3 to be between 20 and 80°. Other physical effects not taken into accounts in our jet injection include the intrinsic rotation of the beam and its variability with time. Simulations including these parameters could easily be launched with A-MaZe.

Moreover, the structure of the environment in which the jet propagates has been heavily simplified. In high-mass microquasars, jets are launched into winds originating from orbiting and rotating stars. This causes a circumbinary environment structured in Archimedean spirals, in both colliding wind binaries (Walder, 1995) and in accreting binaries (Walder et al., 2008, 2014b). These spirals, also called corotating interaction region (CIR), are bound by shocks which confine high-density, high-temperature regions. Such structures will likely have an impact on the jet propagation and its stability, but will also likely lead to flashing outbursts in emission. The interactions between the jet and this accretion wake could be studied by combining the numerical setup of this study with the simulations of accretion in microquasars from Walder et al. (2014a), letting us investigate the interactions of the jet with the accretion wake. The gravitational focusing of the wind by the BH may also play a role in modifying the environment into which the jet will be launched. The difference in the density profile encountered by the jet during its propagation may have a strong impact in the dynamics and structure of the jets and therefore their observational signatures. This setup would also add the orbital effects to the jet evolution, allowing to compare results with studies such as Bosch-Ramon & Barkov (2016).

Another unknown is wind clumping. We know that winds from hot massive stars are clumped (e.g. Oskinova et al., 2012) with density contrasts $\langle\rho^2\rangle/\langle\rho\rangle^2 \approx 2$, Poutanen et al. (2008) suggested it is likely the case for Cygnus X-1 based on dips in the X-ray light curve (Bałucińska-Church et al., 2000; Miskovicová, Ivica et al., 2016; Hirsch et al., 2019). It is however unknown where these clumps are formed: in the stellar atmosphere or further away from the star, e.g. by supersonic turbulence in the wind. Whether these clumps are small and dense, an intermittent density fluctuation of compressible turbulence or a mix of both is also unknown, see discussion in Walder & Folini (2003). Perucho & Bosch-Ramon (2012) suggests that even moderate wind clumping has strong effects on jet disruption, mass loading, bending and likely energy dissipation. In addition, de la Cita et al. (2017) suggested that the standing shocks introduced in the jet flow by its interaction with a clumpy wind would generate a higher apparent gamma-ray luminosity

through inverse Compton scattering of the stellar photons, as well as efficient synchrotron cooling. One may expect in light of these results that introducing clumpiness in the wind could significantly enhance the radiative cooling of the jet and bring even stronger modifications to its dynamics.

5.2.4 SED

The amelioration of the post-processing performance would also allow my code to perform more precise calculations of the radiations emitted by our relativistic jets, following De Colle et al. (2012). At this point, the work towards drawing a physically-relevant SED from our hydrodynamical simulations is still incomplete even in the framework of thermal, optically-thin processes, and needs to be pushed further to be scientifically relevant. Already existing frameworks to compute spectral energy densities of astrophysical plasmas given a certain set of physical parameters, such as CLOUDY (Ferland et al., 2017), agnpy (Nigro et al., 2020), or other works towards modelling the spectra of microquasars (see e.g. Dubus et al., 2010; Zdziarski et al., 2012; Malzac, 2014; Kantzas et al., 2021, among many) could be combined to this study to present a more complete picture of our simulated jets without investing fully into the implementation of non-thermal processes.

5.2.5 Electron temperature and cooling

In single fluid simulations the dynamics is dominated by the ions, while the electrons are responsible for most of the radiative losses. Studies such as Vink et al. (2015); Zhdankin et al. (2021) have shown processes such as shocks and radiative relativistic turbulences may create and/or maintain a difference between ion and electron temperature. Such temperature difference has been observed in supernova remnants (Vink et al., 2003). In particular, Vink et al. (2015) suggest from thermodynamical consideration at shocks that the sonic Mach number of the upstream flow is the main parameter governing this temperature difference: at low Mach number ($M \leq 2$) the shock will not induce a temperature difference, while at high Mach number above $M \sim 60$ the ratio between electron and ion temperature will be equal to the mass ratio $T_e/T_i = m_e/\langle m_i \rangle$. Between those extremal values, this ratio will roughly vary with M^{-2}.

In relativistic jets, at least two strong shocks present an upstream Mach number strong enough to induce a difference between ion and electron temperature downstream of it: the recollimation shock after injection and the reverse shock at beam end. To ensure the calculated energy losses are valid, we need to check the time taken by the electrons to thermalise to the flow temperature. We use formulas from Trubnikov (1965) found in Huba (2016), to get an estimation for the thermalisation timescale considering the extremal case for high Mach number. The equilibration rate between a population of ions and a population of electrons is given, in the case where the populations have no relative drift, by equation:

$$\nu_\epsilon^{e|i} = 1.8 \cdot 10^{-19} \frac{(m_e m_i)^{1/2} Z_i^2 n_i \lambda_{ei}}{(m_e T_i + m_i T_e)^{3/2}} \ \mathrm{s}^{-1}, \tag{5.2}$$

where λ_{ei} is the Coulomb logarithm of electron-ion collisions, given in Huba (2016) as:

$$\lambda_{ei} = \lambda_{ie} = \begin{cases} 16 - \ln(n_i^{1/2} T_i^{-3/2} Z_i^2 \mu) & \text{if } r > 1 \\ 23 - \ln(n_e^{1/2} Z_i T_e^{-3/2}) & \text{if } r < 1 \text{ and } 10\, Z_i^2/T_e > 1 \\ 24 - \ln(n_e^{1/2} T_e^{-1}) & \text{if } r < 1 \text{ and } 10\, Z_i^2/T_e < 1 \end{cases} \tag{5.3}$$

where $r = T_i m_e / T_e m_i$, $\mu = m_i/m_p$, and temperatures are in eV. The thermalisation timescale is then obtained with $t_{therm} = \nu_\epsilon^{e|i\,-1}$. This Coulomb logarithm is defined as the integral of $1/b$, with b the impact parameter of the collision, and is thus the factor by which small-angle collisions are more effective than large-angle collisions.

Table 5.1 presents the rest mass density and temperature values after the recollimation shock and reverse shock in CygX1 at t = 5000 s and CygX3 at t = 1000 s, the derived thermalisation timescale as well as the associated characteristic length using local flow speed value. In all cases except downstream of CygX3 reverse shock, the associated lengthscale is smaller than the grid resolution, meaning the electrons would have thermalised to the flow temperature after a single simulation grid downstream of the shock. In the last case, we can estimate the volume where an error is made using the flow temperature to derive losses as $V_{therm} = v_h c_s^2 t_{therm}^3$, where c_s is the local sound speed. With $v_h = 3 \cdot 10^9$ cm s^{-1} at t = 1000 s we get $V_{therm} = 3.3 \cdot 10^{33}$ cm^3, which accounts for 0.37% of the inner cocoon volume at that time. We then consider our $T_e = T_i = T$ approximation to be valid in our hydrodynamical framework. In a more realistic framework where the plasma is collisionless (see discussion section 5.2.6), Coulomb interactions cannot equilibrate the electron and ion temperatures, but other processes such as plasma instabilities may fill in that role.

This phenomenon could be overlooked in our simulations, but may be non negligible when performing simulations of jets with other parameters value. Performing 2-fluids simulations evolving protons and electrons separately could allow for more precise results, but the added precision would likely not be worth the added computational costs.

shock	ρ (g cm)$^{-3}$	T (K)	t_{therm} (s)	l_{therm} (cm)
X1 recoll.	$5 \cdot 10^{-15}$	$5 \cdot 10^8$	$4.2 \cdot 10^{-4}$	$4 \cdot 10^6$
X1 reverse	10^{-15}	$3 \cdot 10^{10}$	0.6	$2 \cdot 10^9$
X3 recoll.	10^{-14}	$4 \cdot 10^{10}$	0.1	$2.25 \cdot 10^9$
X3 reverse	$5 \cdot 10^{-15}$	10^{12}	19	$2 \cdot 10^{11}$

Table 5.1: thermalisation of electrons downstream of a shock. Values were taken at t = 5000 s for CygX1 and t = 1000 s for CygX3. l_{therm} is estimated using the local flow speed.

Moreover, our losses are modelised as optically thin at every frequencies, which may not be the case, especially in UV, optical and radio ranges at which our thermal electrons radiates. Reheating due to photon absorption (Belmont et al., 2008) or synchrotron self-absorption as well as effects such as synchrotron self-Compton have not been investigated and may have a strong impact on the jet temperature and therefore structure and dynamics. This may not hold true for Cygnus X-1 where cooling and its effects are moderate but could possibly play a strong role in Cygnus X-3 case, especially since winds from Wolf-Rayet stars are optically thick over larger frequency bands than winds from O-type stars. Also, the temperatures attained in our simulations go higher than the electron pair

production threshold and reach a regime where proton distribution becomes relativistic, which will impact the radiative losses.

Another point not considered in this work is the particle acceleration and the non-thermal processes: particles can be accelerated at magnetic reconnections (Giannios, 2010; Giannios et al., 2009; McKinney & Uzdensky, 2012; Melzani et al., 2014) and shocks (Araudo et al., 2009; Bordas et al., 2009; de la Cita et al., 2017) or by stochastic interaction with magnetised turbulence. Shearing flow acceleration as also been invoked as potential injection process of relativistic particles (Rieger & Duffy, 2019). An extensive review of such processes is given in Marcowith et al. (2020). As all processes will significantly contribute to the non-thermal emission, they can inject a substantial fraction of the kinetic jet energy into non-thermal components and probably change the dynamics as part of the gas energy will be dissipated by the accelerated particles. Alternatively the pressure imparted into these particles can directly modify the flow dynamics.

Non-thermal losses could be included through several means such as parametrized cooling downstream of shocks to model the transfer of kinetic energy to the non-thermal population of electrons, or by adding a population of non-thermal electrons to be passively advected by the fluid and computing the energy spectra of the resulting distribution (see Micono et al. 1999 for a description of the method, which has been used in various works since then). The first suggestion would then need for A-MaZe to detect these shocks to be taken into account. This would also permit to parametrize the T_e/T_i ratio to derive more accurate losses during the jet evolution.

Another important process not included in our numerical model is thermal diffusion by relativistic thermal and non-thermal electrons or X-ray photons. This process is likely important as it creates hot shock-precursors, lowers peak temperatures, smooths out contact interfaces, and enhances cooling. These features are suggested when looking at work which include the process in the context of supernova remnants (Chevalier, 1975; Tilley et al., 2006) and colliding winds in binary systems (Myasnikov & Zhekov, 1998; Motamen et al., 1999). Including heat transfer in a simulation is numerically demanding as it demands (semi-)implicite solvers due to the very stiffness of the process. Nevertheless, a few attempts have been made to develop performent solvers (Balsara et al., 2008; Viallet et al., 2011; Commerçon et al., 2014; Dubois & Commerçon, 2016; Viallet et al., 2016). Future work may expand such attempts to jet simulations.

5.2.6 The hydrodynamical framework assumption

High energy, non-thermal photons are a prominent feature of microquasars observations, present in both the low and high state – though in different form. They are thought to be produced by non-thermal processes happening in the jet (Molina & Bosch-Ramon, 2018; Poutanen & Veledina, 2014; Malzac et al., 2018) where high-energy particles are accelerated to relativistic speeds and adopt a power-law spectrum. The mechanisms invoked to accelerate particles are stochastic acceleration (Fermi mechanism) at shocks, magnetic reconnection, or wave turbulence, see the recent reviews by Marcowith et al. (2020); Matthews et al. (2020). All these acceleration mechanisms imperatively demand the plasma to be collisionless to a high degree. The Coulomb-logarithm (see section 5.2.5 for a definition) of a typical jet beam in microquasars is of order 15 and even higher in large regions of the cocoon. Consequently, kinetic time-scales and kinetic inertial length

scales are more than 10 orders of magnitudes smaller than hydrodynamical ones. In short, the mean free path of thermal particles of a jet may easily be as large as the dynamical length scale of the jet and its cocoon. This opens the question to what degree jets can be understood on the basis of a hydrodynamical model.

Attempts to develop kinetical models of jets have been pursued, see Nishikawa et al. (2021) for a recent review. Such models provide a good insight into the various microphysical processes, and show how instabilities like Kelvin-Helmholtz, Rayleigh-Taylor, kink, etc. translate into the collisionless regime. They also show that jet-like structures can develop on kinetic scales. However, it remains an open question whether the results found on kinetic scales can be scaled up to hydrodynamical scales and thus to scales on which the objects are seen in the skies. Some first steps towards the connection between kinetic and macroscopic scales have recently been made: Dieckmann et al. (2019) show that, under even small magnetic guide fields, kinetic jets can develop a structure resembling the hydrodynamical structure of a jet over scales much larger than the kinetic scales. An electromagnetic piston-like structure is coherently formed, acting like the contact discontinuity between jet and ambient material in a hydrodynamical jet (see also Dieckmann et al., 2017). We note that, in the same context, Dieckmann et al. (2019) also show that a leptonic jet propagating into an ambient ion-electron plasma can accelerate positrons to speeds of several hundred of MeV. This makes microquasars candidate sources to explain the positron population in the cosmic ray spectrum.

Lastly, our study is purely hydrodynamical and is missing on the potential stabilising effects of the magnetic field as well as the development of MHD instabilities. The study of MHD jets is recent (e.g. Mizuno et al., 2015; Martí et al., 2016; Mukherjee et al., 2020) and the field will continue to grow as time passes. The influence of the stellar magnetic field may also lead to further modifications on the structure and dynamics of the jet. A better capture of the magnetic field would lead to more precise calculations of the synchrotron losses, whose relative importance in the dynamics could then be modified.

5.2.7 Wind driving and dynamics

We conclude this discussion by evoking a last caveat of this work, which remain an open question: the radiative driving of the companion star wind, as their velocity and density profiles are prone to a large uncertainty. This pushed us to choose a grid of fixed wind parameters for the study realized during this PhD and make no attempts to model the acceleration of the wind. Winds from massive stars are driven by the radiative pressure on free electrons (to about one third of the driving force) as well as the scattering of stellar photons in millions of UV and optical lines. This wind driving is expected to be vastly different between super-giants (as in Cygnus X-1) and WR stars (as in Cygnus X-3), in that the winds from the latter type are optically thick in the subsonic acceleration phase whereas it is relatively optically thin in super-giant winds.

Such winds are well-understood for single stars, with the exception of the sub-sonic phase of WR winds, see the review by Kudritzki & Puls (2000). In binaries, the situation is more complex. Hainich et al. (2020) present an observation based study of winds in high-mass XRBs and basically confirm that the wind-driving can be put on the same general ideas as in single hot massive stars. However, the situation is more complicated due to the presence of a secondary radiation source, either another star or a compact

object and its environment. This second source leads to an ionisation structure within the wind which, in contrast to the single-star situation, does not fit the frequencies of the photons emitted by the star producing the wind.

This affects in particular the region between the wind-shedding star and its companion. There, the driving by photon scattering in spectral lines can be suppressed and the wind acceleration may be weaker or even inhibited compared to the winds of a single star (Stevens & Kallman, 1990; Stevens, 1991; Blondin, 1994). Models taking in account such inhibition can be fit to observations (Gies et al., 2008). The case of Cygnus X-1 have been investigated through complex radiation hydrodynamics simulations by Hadrava & Čechura (2012) and Krtička et al. (2015), which suggested strong inhibition of the wind speed could happen at the location of the black hole. In this region, wind density and velocity profiles in binaries are very difficult observationally access and are largely unknown. For Cygnus X-3, the situation is even more unknown as the wind is still optically thick at the BH location, studies such as Vilhu et al. (2021) find a strong wind suppressing effect in the extreme-UV region especially. However, we can firmly state that a wind is present in both systems, e.g. by the modulation of the X-ray light curve over the binary orbit. This modulation is due the different optical paths X-ray photons have to travel through the wind and thus different attenuation of the X-ray light through absorption in the wind (Bonnet-Bidaud & van der Klis, 1981; Poutanen et al., 2008; Grinberg et al., 2015).

Another important open problem is the influence of magnetic fields on the wind, as strong fields could substantially influence the mass shedding process, e.g. by a large enhancement of the mass-loss in the equatorial plane (ud-Doula et al., 2006, 2008; Bard & Townsend, 2016). A general discussion of magnetic fields of massive stars and how they influence their environment can be found in Walder et al. (2012).

Bibliography

Araudo A. T., Bosch-Ramon V., Romero G. E., 2009, A&A, 503, 673
Balsara D. S., Tilley D. A., Howk J. C., 2008, MNRAS, 386, 627
Bałucińska-Church M., Church M. J., Charles P. A., Nagase F., LaSala J., Barnard R., 2000, MNRAS, 311, 861
Bard C., Townsend R. H. D., 2016, MNRAS, 462, 3672
Belmont R., Malzac J., Marcowith A., 2008, A&A, 491, 617
Blondin J. M., 1994, ApJ, 435, 756
Bodo G., Massaglia S., Ferrari A., Trussoni E., 1994, Astronomy and Astrophysics, 283, 655
Bonnet-Bidaud J. M., van der Klis M., 1981, A&A, 101, 299
Bordas P., Bosch-Ramon V., Paredes J. M., Perucho M., 2009, A&A, 497, 325
Bosch-Ramon V., Barkov M., 2016, Astronomy & Astrophysics, 590, A119
Chevalier R. A., 1975, ApJ, 198, 355
Commerçon B., Debout V., Teyssier R., 2014, A&A, 563, A11
De Colle F., Granot J., López-Cámara D., Ramirez-Ruiz E., 2012, The Astrophysical Journal, 746, 122

Dieckmann M. E., Folini D., Walder R., Romagnani L., d'Humieres E., Bret A., Karlsson T., Ynnerman A., 2017, Physics of Plasmas, 24, 094502
Dieckmann M. E., Folini D., Hotz I., Nordman A., Dell'Acqua P., Ynnerman A., Walder R., 2019, A&A, 621, A142
Dubois Y., Commerçon B., 2016, A&A, 585, A138
Dubois Y., Commerçon B., Marcowith A., Brahimi L., 2019, Astronomy & Astrophysics, 631, A121
Dubus G., Cerutti B., Henri G., 2010, MNRAS: Letters, 404, L55
Ferland G., et al., 2017, Revista Mexicana de Astronomia y Astrofisica, 53
Gallo E., Fender R., Kaiser C., Russell D., Morganti R., Oosterloo T., Heinz S., 2005, Nature, 436, 819
Giannios D., 2010, MNRAS, 408, L46
Giannios D., Uzdensky D. A., Begelman M. C., 2009, MNRAS, 395, L29
Gies D. R., et al., 2008, ApJ, 678, 1237
Grinberg V., et al., 2015, A&A, 576, A117
Hadrava P., Čechura J., 2012, A&A, 542, A42
Hainich R., et al., 2020, A&A, 634, A49
Hirsch M., et al., 2019, A&A, 626, A64
Horton M. A., Krause M. G. H., Hardcastle M. J., 2020, MNRAS, 499, 5765
Huba J. D., 2016, NRL plasma formulary. Naval Research Laboratory
Kantzas D., et al., 2021, Monthly Notices of the Royal Astronomical Society, 500, 2112
Krtička J., Kubát J., Krtičková I., 2015, A&A, 579, A111
Kudritzki R.-P., Puls J., 2000, ARA&A, 38, 613
Malzac J., 2014, Monthly Notices of the Royal Astronomical Society, 443, 299
Malzac J., et al., 2018, MNRAS, 480, 2054
Marcowith A., Ferrand G., Grech M., Meliani Z., Plotnikov I., Walder R., 2020, Living Reviews in Computational Astrophysics, 6, 1
Martí J., Paredes J., Peracaula M., 2001, Astronomy & Astrophysics, 375, 476
Martí J. M., Perucho M., Gómez J. L., 2016, APJ, 831, 163
Matthews J. H., Bell A. R., Blundell K. M., 2020, New A Rev., 89, 101543
McKinney J. C., Uzdensky D. A., 2012, MNRAS, 419, 573
Melzani M., Walder R., Folini D., Winisdoerffer C., Favre J. M., 2014, A&A, 570, A112
Micono M., Zurlo N., Massaglia S., Ferrari A., Melrose D., 1999, arXiv preprint astro-ph/9906440
Mignone A., McKinney J. C., 2007, Monthly Notices of the Royal Astronomical Society, 378, 1118
Mihalas D., Mihalas B. W., 2013, Foundations of radiation hydrodynamics. Courier Corporation
Mirabel I., Rodriguez L., 1994, Nature, 371, 46
Miskovicová, Ivica et al., 2016, A&A, 590, A114
Mizuno Y., Gomez J. L., Nishikawa K.-I., Meli A., Hardee P. E., Rezzolla L., 2015, APJ, 809, 38
Molina E., Bosch-Ramon V., 2018, A&A, 618, A146
Motamen S. M., Walder R., Folini D., 1999, in van der Hucht K. A., Koenigsberger G., Eenens P. R. J., eds, Vol. 193, Wolf-Rayet Phenomena in Massive Stars and Starburst

Galaxies. p. 378
Mukherjee D., Bodo G., Mignone A., Rossi P., Vaidya B., 2020, MNRAS, 499, 681
Myasnikov A. V., Zhekov S. A., 1998, MNRAS, 300, 686
Nigro C., Sitarek J., Craig M., Gliwny P., 2020, agnpy: modelling Active Galactic Nuclei radiative processes with python. Zenodo
Nishikawa K., DuÅ£an I., Köhn C., Mizuno Y., 2021, Living Reviews in Computational Astrophysics, 7, 1
Orosz J. A., McClintock J. E., Aufdenberg J. P., Remillard R. A., Reid M. J., Narayan R., Gou L., 2011, APJ, 742, 84
Oskinova L. M., Feldmeier A., Kretschmar P., 2012, MNRAS, 421, 2820
Perucho M., Bosch-Ramon V., 2008, Astronomy & Astrophysics, 482, 917
Perucho M., Bosch-Ramon V., 2012, Astronomy & Astrophysics, 539, A57
Perucho M., Hanasz M., Marti J.-M., Sol H., 2004a, Astronomy & Astrophysics, 427, 415
Perucho M., Marti J.-M., Hanasz M., 2004b, Astronomy & Astrophysics, 427, 431
Perucho M., Bosch-Ramon V., Khangulyan D., 2010a, International Journal of Modern Physics D, 19, 791
Perucho M., Bosch-Ramon V., Khangulyan D., 2010b, Astronomy & Astrophysics, 512, L4
Poutanen J., Veledina A., 2014, Space Sci. Rev., 183, 61
Poutanen J., Zdziarski A. A., Ibragimov A., 2008, MNRAS, 389, 1427
Rieger F. M., Duffy P., 2019, ApJ, 886, L26
Scheck L., Aloy M., Martí J., Gómez J., Müller E., 2002, Monthly Notices of the Royal Astronomical Society, 331, 615
Stevens I. R., 1991, ApJ, 379, 310
Stevens I. R., Kallman T. R., 1990, ApJ, 365, 321
Synge J., 1957, The Relativistic Gas
Tilley D. A., Balsara D. S., Howk J. C., 2006, MNRAS, 371, 1106
Trubnikov B. A., 1965, Reviews of Plasma Physics, 1, 105
Viallet M., Baraffe I., Walder R., 2011, A&A, 531, A86
Viallet M., Goffrey T., Baraffe I., Folini D., Geroux C., Popov M. V., Pratt J., Walder R., 2016, A&A, 586, A153
Vilhu O., Kallman T. R., Koljonen K., Hannikainen D. C., 2021, A&A, 649, A176
Vink J., Laming J. M., Gu M. F., Rasmussen A., Kaastra J. S., 2003, APJL, 587, L31
Vink J., Broersen S., Bykov A., Gabici S., 2015, A&A, 579, A13
Walder R., 1995, in van der Hucht K. A., Williams P. M., eds, Vol. 163, Wolf-Rayet Stars: Binaries; Colliding Winds; Evolution. p. 420
Walder R., Folini D., 2000, in Thermal and Ionization Aspects of Flows from Hot Stars. p. 281
Walder R., Folini D., 2003, in van der Hucht K., Herrero A., Esteban C., eds, Vol. 212, A Massive Star Odyssey: From Main Sequence to Supernova. p. 139
Walder R., Folini D., Shore S. N., 2008, A&A, 484, L9
Walder R., Folini D., Meynet G., 2012, Space Sci. Rev., 166, 145
Walder R., Melzani M., Folini D., Winisdoerffer C., Favre J. M., 2014a, arXiv preprint arXiv:1405.0600
Walder R., Melzani M., Folini D., Winisdoerffer C., Favre J. M., 2014b, in Pogorelov

N. V., Audit E., Zank G. P., eds, Astronomical Society of the Pacific Conference Series Vol. 488, 8th International Conference of Numerical Modeling of Space Plasma Flows (ASTRONUM 2013). p. 141 (arXiv:1405.0600)

Yoon D., Heinz S., 2015, The Astrophysical Journal, 801, 55

Yoon D., Zdziarski A. A., Heinz S., 2016, Monthly Notices of the Royal Astronomical Society, 456, 3638

Zdziarski A. A., Lubiński P., Sikora M., 2012, Monthly Notices of the Royal Astronomical Society, 423, 663

Zdziarski A. A., Mikołajewska J., Belczyński K., 2013, MNRAS: Letters, 429, L104

Zhdankin V., Uzdensky D. A., Kunz M. W., 2021, APJ, 908, 71

de la Cita V. M., del Palacio S., Bosch-Ramon V., Paredes-Fortuny X., Romero G. E., Khangulyan D., 2017, A&A, 604, A39

ud-Doula A., Townsend R. H. D., Owocki S. P., 2006, ApJ, 640, L191

ud-Doula A., Owocki S. P., Townsend R. H. D., 2008, MNRAS, 385, 97